# Durham E-Theses

## *Three-dimensional and Two-dimensional Modelling of Springback in the Single-pass Conventional Metal Spinning of Cones*

ASHWORTH, RACHEL,HELEN,SUSAN

**How to cite:**

**Use policy**

# Three-dimensional and Two-dimensional Modelling of Springback in the Single-pass Conventional Metal Spinning of Cones

Thesis by

## Rachel Ashworth

Submitted as partial consideration towards
the degree of Master of Philosophy

Mechanics Research Group
School of Engineering and Computing Sciences
Durham University
United Kingdom
August 2013

# **Abstract**

Parts for industrial and domestic use have been formed by means of the metal spinning process as far back as the ancient Egyptians. Research into the field was initially concentrated on experimental and theoretical studies. The development of numerical methods alongside the increasing capabilities of modern computing brought about numerical investigations into the process. This thesis presents a three-dimensional numerical model developed using the finite element method. In addition, a formability parameter is proposed and a formability surface linking the round off radius, rotational speed and half cone angle of the mandrel is presented. This thesis also presents the first numerical parametric study into springback using a three-dimensional finite element model.

## Declaration

The work in this thesis is based on research carried out at the School of Engineering and Computing Sciences, University of Durham, England, United Kingdom. No part of this thesis has been submitted elsewhere for any other degree or qualification and it is all my own work unless referenced to the contrary in the text.

## Acknowledgements

*For my beloved Grandad*

**"All models are wrong, but some are useful",** George Box

# Contents

# List of Figures

# List of Tables

# §1    Introduction

There are many different processes which can be used to form metal parts for use in industry; some commonly used processes include stamping, bending and extrusion. In extrusion processes, a billet of metal which is positioned in a container is forced through an opening in one end of the container. The material is forced from the container by either applying a ram to the opposite side of the billet, known as forward extrusion. Alternatively, the orifice may be moved towards the opposite side of the container which is known as backward extrusion as illustrated in Figure 1.1. Backward extrusion has been found to give better results than forward extrusion (Valberg, 2010) because the action of moving the orifice in forward extrusion generates deformation of the orifice geometry. This in turn creates variations in the cross section of the extruded part.
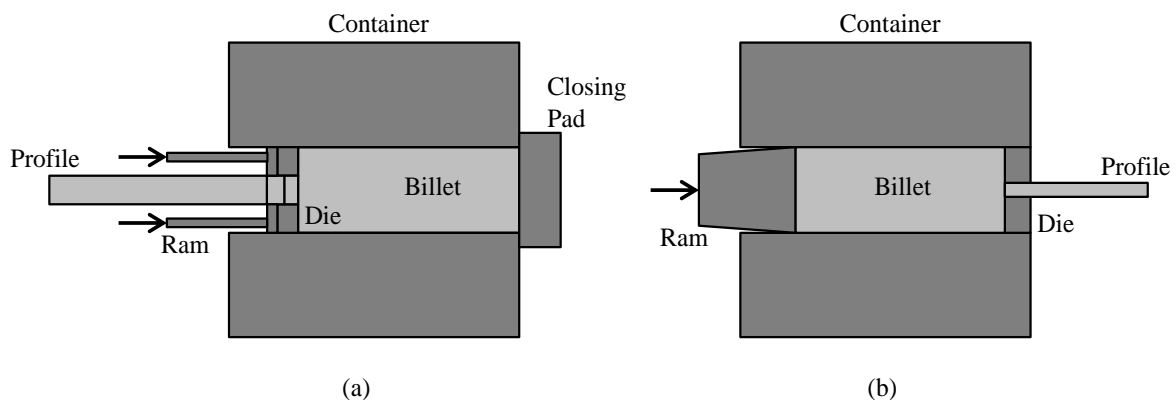


Figure 1.1: (a) Backward extrusion, (b) Forward extrusion

(adapted from Valberg (2010))

The stamping process is often used to manufacture parts for the automobile industry. The process involves a sheet metal blank being rested on a die which bears the geometry of the final part. A punch, whose geometry is the same as the void in the die, is then applied vertically to the workpiece as illustrated in Figure 1.2.
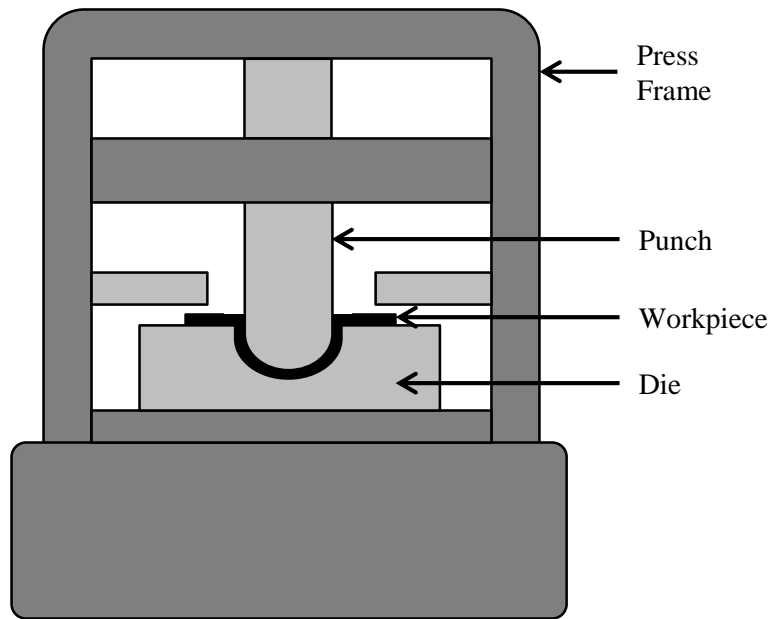
Figure 1.2: Stamping process (adapted from Wick *et al.* (1984))

The bending process is used to create parts with straight sides as opposed to the stamping operation which can be used to form parts with multiple bends or curved sides. Similarly to the stamping process, the blank rests over a die which bears the intended geometry as illustrated in Figure 1.3.
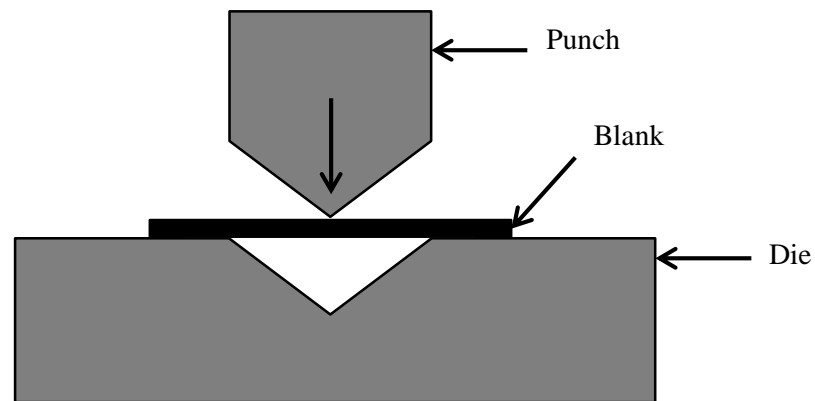
Figure 1.3: Bending process (adapted from Wick *et al.* (1984))

Both the bending and stamping processes have the advantage that they are quick processes; however, the expense of altering the design of the intended geometry is a key disadvantage to both processes as it requires re-tooling.

## 1.1    Metal Spinning

A further, lesser known metal forming process is metal spinning (Packham, 1976). In metal spinning a blank, usually a circular but occasionally square piece of metal is clamped between a mandrel, which bears the form of the intended part, and a tailstock as illustrated in Figure 1.4. The blank is then gradually deformed by means of a roller passing over the surface of the blank in either a single or multiple series of passes. This may or may not occur at a constant feed (mm/rev) which is evaluated from the ratio of roller velocity to mandrel rotational velocity.
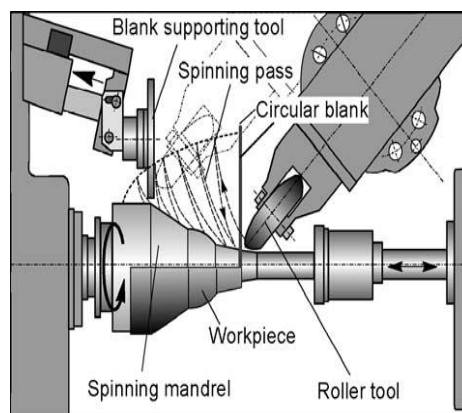
Figure 1.4: Configuration of the metal spinning process (Kleiner *et al*. (2002))

The modern day metal spinning process is very versatile, and can be used to produce parts ranging in diameter from 3 mm to 10 m and thicknesses ranging from 0.4 mm to 25 mm (Music *et al*. (2010)). Modern day metal spinning is used to produce parts such as nose cones for aeroplanes, components for MRI scanners and components of a military nature in addition to decorative items such as sculptures. Indeed, the feet of the Angel of the North were manufactured using the metal spinning process. Figures 1.5 and 1.6 show a range of components manufactured by means of the metal spinning process.

In industry, stainless steel, copper and aluminium are commonly spun metals. Metal spinning has many advantages over other forming processes as there is no need for individual moulds to be cast for parts which differ minutely in dimensions. Furthermore, there is very little material wastage and high

dimensional accuracy can be achieved. An additional advantage of the metal spinning process is that it is a relatively quick manufacturing process requiring a lesser forming force which in turn reduces operating costs. The fact that tensile and yield strength are also improved also enables the possibility for substitution of cheaper materials (Wick *et al*. (1984)). All these factors render the metal spinning process industrially competitive.



Figure 1.5: Smaller parts formed using the metal spinning process (Kleiner *et al*. (2005))



Figure 1.6: 2m diameter parts from Leifield USA (Bewlay, online)

## 1.2    Springback

There are a number of ways in which a part may be rendered unsuitable for its intended purpose; one of these ways is springback. Springback manifests itself as a geometrical change as a result of the release of residual elastic effects; this may result in a part having a geometry outside a specified dimensional tolerance, therefore resulting in industrial wastage. Whilst springback cannot be eliminated, the ability to anticipate the amount of springback for a given set of parameters would help to reduce wastage in industry resulting in lower costs in terms of time and materials and consequently improving productivity. In some metal forming processes, for example three point v-bending, much research as to the influence of blank thickness, punch geometry and die geometry on the level of springback has been investigated. The metric used to quantify the amount of springback in three point v-bending is defined as the ratio of the angle made between a straight edge and the horizontal before and after springback and is referred to as the springback ratio (denoted as K in Figure 1.7).

$\alpha_1$ = Angle before springback
$\alpha_2$ = Angle after springback

$$K = \frac{\alpha_2}{\alpha_1}$$

Bend Angle
$\alpha$
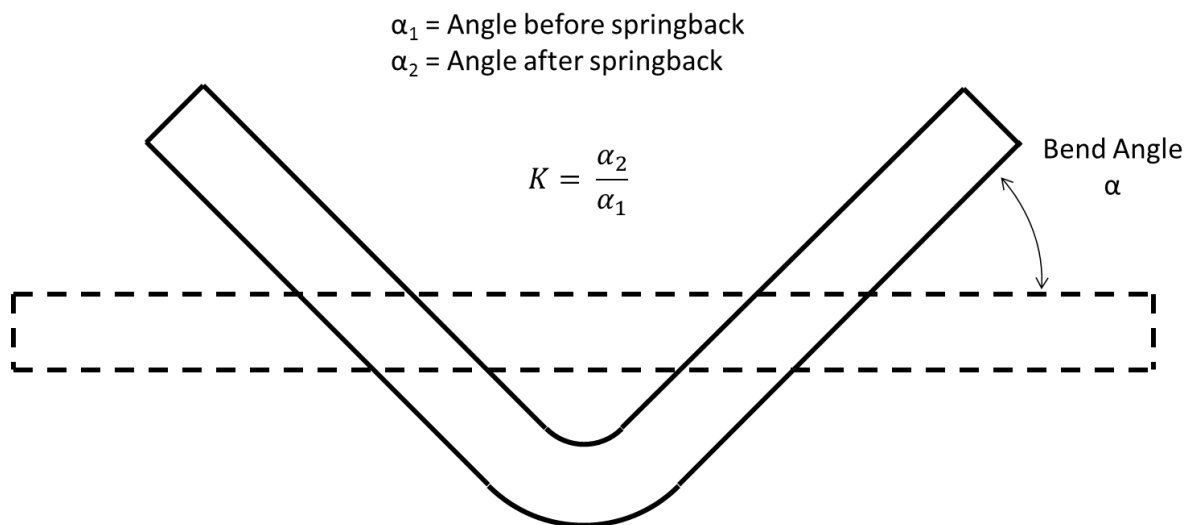
Figure 1.7: Springback ratio definition

Figure 1.8 illustrates the relationship between the springback ratio and the ratio of the bend radius, $R_1$, and the blank thickness, t, for a range of metals.
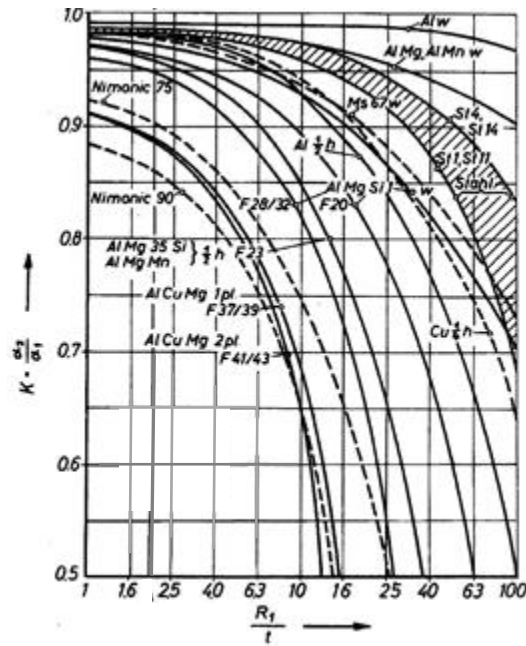
Figure 1.8: Springback ratio in v-bending (adapted from Oehler (1963) cited in Valberg (2010)).

Figure 1.8 illustrates that for a given bend radius, increasing the blank thickness reduces the amount of springback observed for the three point v-bending process. Conversely, for a given blank thickness, springback may be reduced by decreasing the bend radius.

In terms of three-dimensional processes, Yang (1986) investigated springback in the extrusion process for three cross-sectional profiles as illustrated in Figure 1.9. The metal (aluminium) used is extruded through an angle $\theta_L$ as it is formed.
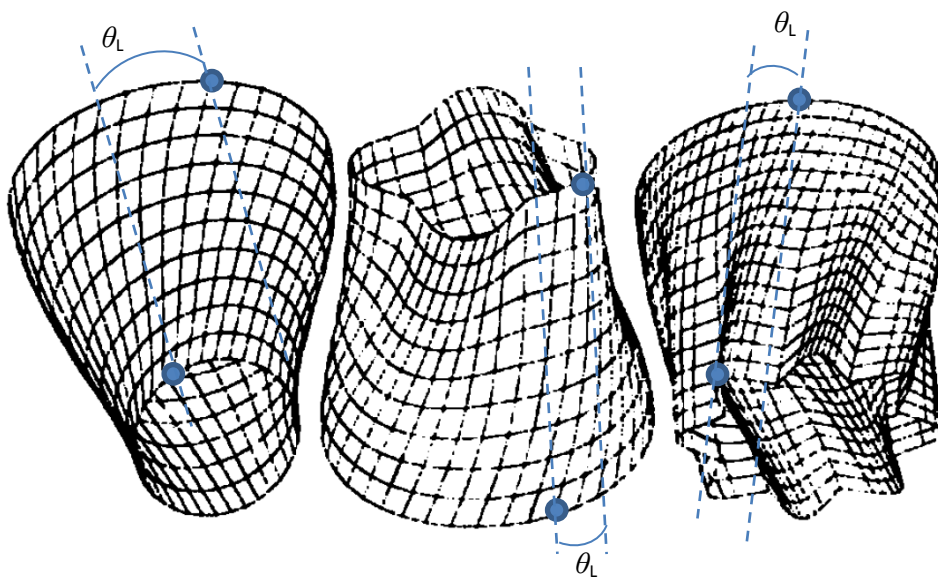


Figure 1.9: Oval, clover and troicoidal Cross sectional profiles from Yang (1986)

Their investigation found that springback was most pronounced for the clover shaped die, and that both dimensions A and B as marked in Table 1.1 were larger than the intended value. Furthermore, the angle of rotation, $\theta_L$, differed from that which was intended. This would indicate that springback occurs in multiple directions simultaneously although Yang (1986) does not elaborate on this point.
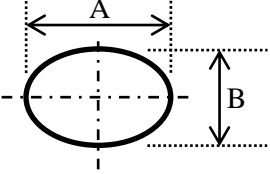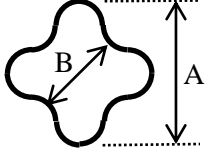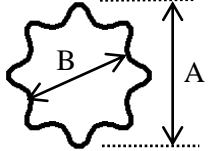
| | | | |
|---|---|---|---|
| DESIGNED DIMENSION OF DIE | A = 23.24mm<br>B = 15.49mm<br>$\Theta_L = 45°$ | A = 22.54mm<br>B = 15.02mm<br>$\Theta_L = 45°$ | A = 25.4mm<br>B = 17.8mm<br>$\Theta_L = 45°$ |
| MANUFACTURED DIMENSION OF DIE | A = 22.91mm<br>B = 15.36mm | A = 22.24mm<br>B = 15.12mm | A = 26.36mm<br>B = 17.97mm |
| DIMENSION OF PRODUCT | A = 23.04mm<br>B = 15.60mm<br>$\Theta_L = 25°$ | A = 22.43mm<br>B = 15.38mm<br>$\Theta_L = 39°$ | A = 28.51mm<br>B = 18.22mm<br>$\Theta_L = 42°$ |

Table 1.1: Dimensional results for extrusion profiles examined by Yang (1986)

For three dimensional axisymmetric problems such as stamping, springback has been investigated and been shown to be asymmetric. Figure 1.10 shows the experimental configuration used by Yu *et al.* (1984) to investigate a hemispherical stamping process.
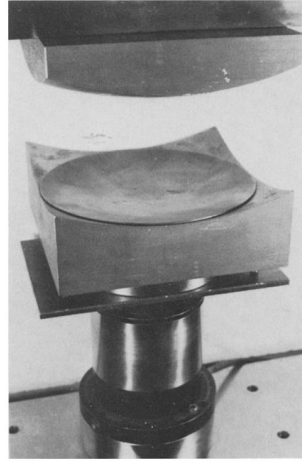
Figure 1.10: Experimental set up used by Yu *et al.* (1984)

Yu *et al.* (1984) found that the parts did not form uniformly as illustrated in Figure 1.11. In terms of springback, the metric used by Yu *et al.* (1984) is to define springback in terms of the radii of the part before and after springback. The authors do not state how this is measured; there is one plot presented which relates the average springback ratio to punch force (expressed as a multiple of the yield stress multiplied by the surface area of the plate). The plot shows that the springback ratio increases as the punch force increases up to a maximum at around three times the yield stress of the aluminium multiplied by the surface area of the plate, beyond which there is little difference.
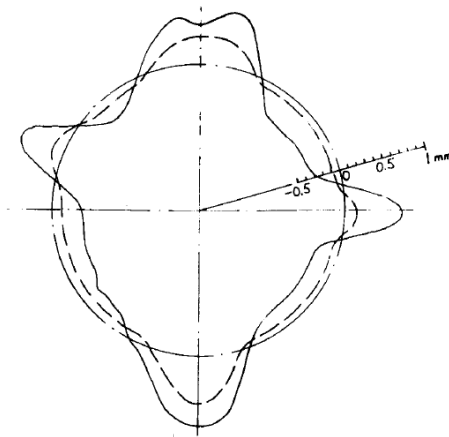


Figure 1.11: Part geometry after forming for a blank of radius 100mm (from Yu *et al.* (1984))

Further metrics for measuring springback are discussed in the literature review. At the present time, there is no standard metric for measuring springback in the metal spinning process.

## 1.3    Experimental Measurement Techniques within Metal Spinning

The metal spinning process does not easily lend itself to the experimental measurement of strains. Experimental techniques in the literature include etching circles on the surface of the blank (Quigley and Monaghan (2000), Beni *et al.* (2010), Razavi *et al.* (2005), Shimizu (2010)), drilling and subsequently plugging holes in the blank (Avitzur and Yang (1960)). A technique of splitting a blank in half, etching a grid through the thickness and then soldering the blank back together before forming and then subsequently splitting the blank and examining the deformation to the grid was described by Kalpakcioglu (1961). Whilst these techniques may provide an insight as to the deformation a part may undergo during a spinning process, the extent to which the measurement technique has influenced the results has not been examined in detail.

## 1.4    Structure of the thesis

This thesis delivers a formability parameter for the conventional metal spinning process in addition to a metric for measuring springback. Furthermore, a three-dimensional parametric study into springback is conducted and examines the influence of the half cone angle of the mandrel, the rotational speed and the mandrel round-off radius on the springback generated. In addition, a two-dimensional finite element springback tool is developed in order to model the average springback obtained in the three-dimensional case. All these are original contributions to the body of knowledge on metal spinning.

This thesis has five further chapters consisting of a literature survey in Chapter Two reviewing the literature appropriate to this thesis. Following on from this, Chapter Three provides background details of the finite element method which is the primary research tool used in this project as it was not possible for experiments to be conducted. Chapter Four details the development of the three-dimensional finite element model used to investigate a single pass conventional metal spinning

process. In addition, a formability parameter, formability surface linking the mandrel round-off radius, half cone angle and rotational speed are presented. Chapter Five consists of a parametric study into springback using the three-dimensional finite element model developed in Chapter Four. The thesis closes with conclusions and suggestions for future work.

# §2    Literature Review

## 2.0    Introduction

The lower tooling and running costs associated with the metal spinning process, alongside the diverse range of geometries possible; make it a particularly attractive option for manufacturers of metal components. Research into the field has mostly taken the form of experimental and numerical investigations as the dynamic nature of the process does not lend itself easily to analytical modelling. Nevertheless, analytical models have been used to model the tool forces experienced throughout the forming process although the body of literature available in this field is relatively small in comparison with other metal forming processes.

## 2.1    Geometry

There are generally three types of geometry considered in the metal spinning literature as shown in Figures 2.1, 2.2 and 2.3 and they can be classified as cylindrical, conical and hemispherical geometries.
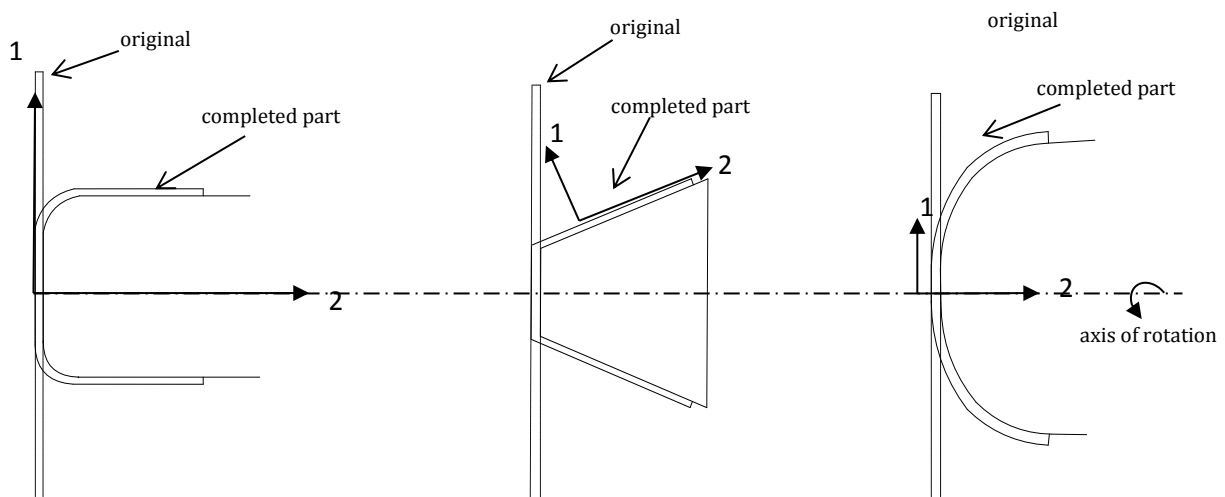
Figure 2.1: Cylindrical geometry

Figure 2.2: Conical geometry

Figure 2.3: Hemispherical geometry

Throughout this thesis, the coordinate system illustrated in Figure 2.1 is adopted where the direction shown as 1 is referred to as the radial direction and direction 2 is the axial direction and the out of the page direction is referred to as the hoop or circumferential direction.

## 2.2    Shear and Conventional Metal Spinning

There are two types of metal spinning, namely shear and conventional metal spinning, which are used to form the parts shown in Figures 2.1 and 2.2. In conventional spinning, the aim of the process is that the finished part has the same thickness as the original blank. Therefore, in the conventional spinning process, the radial and hoop strains should be equal. Conversely, in shear spinning, the blank thickness is intentionally reduced. In ideal shear spinning, the diameter of the final part is the same as the diameter of the blank, resulting in an ideal thickness given by the 'sine law' equation (2.1). The 'sine law' relates the blank thickness and half cone angle of the mandrel to the final thickness of the part as

$$t_f = t_0 \sin \alpha \tag{2.1}$$

where $t_0$ and $t_f$ are the initial and final thicknesses, respectively and $\alpha$ is the half cone angle of the geometry as illustrated in Figure 2.4. In ideal shear spinning, the thickness strain should be equal to the axial strains.
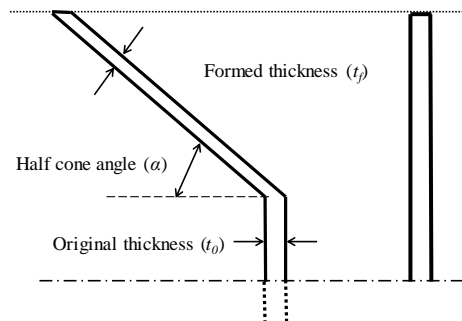


Figure 2.4: Schematic of ideal shear spinning

## 2.3    Forces

The forces studied in metal spinning originate from the reaction force between the roller and the workpiece, which is then resolved into three mutually perpendicular directions resulting in the radial force, axial force and hoop force consistent with the definitions of the radial, axial and hoop directions in Figures 2.1-2.3. Referring to the geometry of Figure 2.3, Wang *et al.* (1989) found that for a three pass conventional spinning process on a hemispherical mandrel using a 2mm thick aluminium blank of diameter 120mm and mandrel rotational speeds varying from 200rpm – 1120rpm; the relative ratios of the axial, radial and hoop forces (resolved to cylindrical notation) to be as

$$F_{axial} : F_{radial} : F_{hoop} = 20 : 10 : 1 \ . \tag{2.2}$$

which would appear to be similar to the findings of Essa and Hartley (2009) who found that the axial force was around double the radial force for a single pass process forming aluminium on the cylindrical geometry. However, Wang and Long (2011b) found the ratio of the forces to be of the order 35:17:1 for a three pass process forming mild steel on a cylindrical geometry. Xia *et al.* (2005) used aluminium to form cups on a cylindrical geometry and found that the axial force was greater than the radial force only for the early stages of the forming process, illustrated in Figure 2.5, after which, the reverse was true.

For the conical geometry, Chen *et al.* (2005) who conducted an analytical and experimental study using a shear spinning process to form a $50^{o}$ aluminium cone found the force ratio (2.2) to be of the order of 4:3:1. This would appear to contradict the findings of Colding (1959) who conducted experiments on aluminium blanks of thicknesses between 6.45mm and 19.4mm and stated that the radial force was both larger than the axial force and between ten and thirty times larger than the hoop force. Combining the results of all these researchers, it can be seen that there is a consensus of opinion that the hoop force is the smallest of the force components. However, since El-Khabeery *et al.* (1991) suggest that the relationship between the axial and radial forces is dependent upon the angle the roller makes with the workpiece which makes the results of the aforementioned research difficult to compare since Chen *et al.* (2005) state that the angle of inclination of the roller they use is $60^{o}$

whereas Avitzur and Yang (1960) use an inclination angle of 90$^{\circ}$, other authors do not provide details. Therefore, whilst it is possible to say that the relationship between the axial and radial forces would therefore appear to be dependent upon the material type, blank geometry, roller contact angle and mandrel rotational speed; however, without a parametric study it is difficult to make any further comparisons.
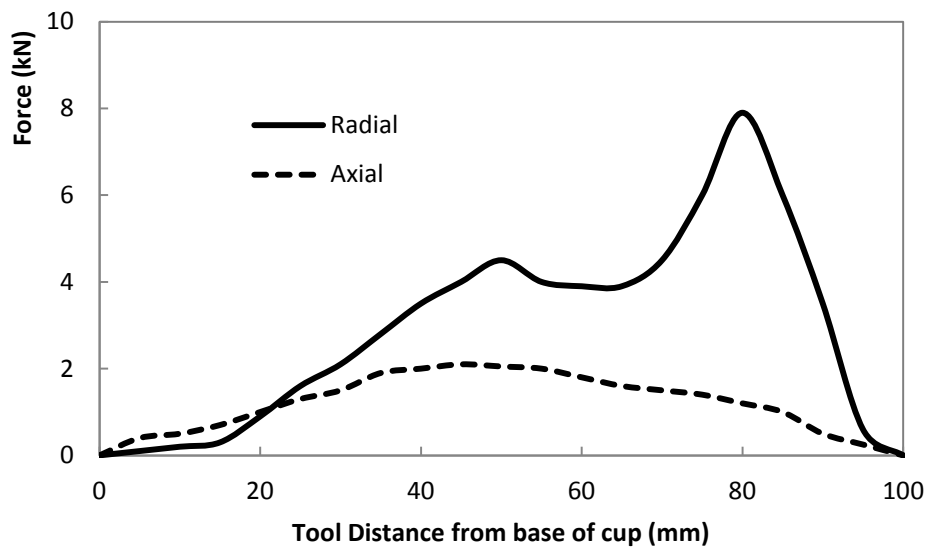


Figure 2.5: Radial and Axial force components (adapted from Xia *et al.* (2005)).

The power needed to form a part is related to the hoop force, since the hoop force does most of the work in forming a part (Sortais *et al.* (1963), Kalpakcioglu (1961), Colding (1959)). Therefore early work concentrated on predicting the hoop force in order to estimate the power required to drive the mandrel. Consequently, researchers such as Avitzur and Yang (1960), Kalpakcioglu (1961), Zhan *et al.* (2007) and Sortais *et al.* (1963) (who all used conical geometries) and Hayama and Murota (1963) (who used the cylindrical geometry), conducted theoretical and experimental investigations focussed on trying to develop an understanding of the forces in metal spinning in order to predict the power required to manufacture a part. All these studies agree that the hoop force is the smallest of the force components.

There have been attempts to provide theoretical expressions for the hoop force in metal spinning. Many of these papers include the assumption that it is the hoop force which does most of the work in deforming the metal (Colding (1959), Kobayashi *et al.* (1961), Chen *et al.* (2005)). This is justified by considering that the energy required to deform the part is evaluated by multiplying each respective force component by the distance over which it acts. The distance over which the hoop force acts is far greater than the distance for either the radial or axial force components. When deriving experimental expressions for the hoop force, quantifying the exact contact area between the roller and the workpiece has proved a fundamental issue in finding representative expressions (Hayama and Murota (1963), Hayama (1974), Kobayashi *et al.* (1961), Sortais *et al.* (1963)). Hayama and Murota (1963) attribute the peaks observed in the radial force (for example as illustrated in Figure 2.5) to the respective (drawing and ironing) deformation modes they assume present in the spinning process. Essa and Hartley (2009) attribute the first peak to the maximum plastic deformation and the second peak to the material thickening towards the open end of the cup.

## 2.4    Relationship between the force components and process parameters

### 2.4.1   Clearance

Sortais *et al.* (1963) defined the term under-spinning to mean that the clearance between the roller and the mandrel surface is greater than the thickness given by the 'sine law' (Equation 2.1). Conversely, they define over-spinning to mean a roller clearance less than the thickness predicted by the sine law. Hayama *et al.* (1965) found that under-spinning resulted in minimal changes in the three force components. However, Hayama *et al.* (1965) found that for over-spinning the radial and hoop force components decreased whilst the axial force component increased. Furthermore, they note that the clearance appears to influence the behaviour of the flange; where the part is under-spun, the authors report that the flange has a tendency to bend backwards towards the roller. When the part undergoes over-spinning, the authors report that the flange tends to lean forward and can lead to wrinkling. Similarly, Slater and Joorabchian (1976) found that all three force components increased as an under-

spinning regime was entered. This was attributed to the fact that the flange was bent to such an extent that it made contact with the roller (Slater (1979)). Similarly, Xia *et al*. (2005) considered the effect of using different clearances on the forming of aluminium cylindrical parts and found that the axial and radial forces decreased as the clearance increased; this was also observed for the shear spinning process by Chen *et al*. (2005). The thickness distribution of a formed part was reported as being more uniform for a smaller clearance by Essa and Hartley (2010). When modelling the metal spinning process via finite element simulations, Razavi *et al*. (2005) suggested that the value of clearance should be adjusted to account for any elastic behaviour of the roller.

### 2.4.2   Roller Geometry and Angle

There has been much discussion, although little consensus as to the significance of the roller nose radius or the nature of the interaction between the roller and the workpiece. Indeed, there exists an example in the published literature whereby the authors ignore the friction between the blank and the workpiece and only model part of the roller (thereby neglecting any rotational effects of the roller), (Sebastiani *et al*. (2006)). Furthermore, recent research (Music and Allwood (2011)) has suggested that the mandrel may be replaced by three rollers (in addition to the forming roller). In their review paper, Wong *et al*. (2003) state that the roller diameter has little effect on the product although they acknowledge that too small a roller nose radius will result in poor thickness uniformity. For the shear spinning process; Kim *et al*. (2003), Hayama *et al*. (1965) report an increase in axial and radial forces as the roller nose radius is increased. However, Avitzur and Yang (1960), Kim *et al*. (2003), Hayama *et al*. (1965) and Dröge (1954) [cited in Music *et al*. (2010)] report an inverse relationship between the roller nose radius and the hoop force. This is consistent with El-Khabeery *et al*. (1991) who found that increasing the roller nose radius resulted in an increase in thickness towards the base of the part in addition to closer conformity to the mandrel geometry. Wang *et al*. (1989) report that increasing the roller nose radius increases all components of the working force; this was also observed by El-Khabeery *et al*. (1991). Both El-Khabeery *et al*. (1991), Kleiner *et al*. (2005) and Chen *et al*. (2001)

find that using a larger roller nose radius results in a smoother finish on the final part which is attributed to the increase in contact area between the roller and the blank. Hayama *et al*. (1966) report that using a larger roller nose radius reduces the likelihood of the part to wrinkle whilst Kleiner *et al*. (2005) state that for a larger roller nose radius (20mm), the clearance did not influence the surface quality. However, for a smaller roller nose radius (10mm), Kleiner *et al*. (2005) state that the surface quality is improved by using a larger clearance. Similarly, Wells (1968) states that a smaller nose radius results in poorer surface finish; furthermore, Wells (1968) also investigated the phenomenon of material build up around the roller for the cylindrical geometry. He found that build up could be controlled by altering the roller tilt angle in addition to decreasing the feed rate. Additionally, Wells (1968) found experimentally (for a shear metal spinning process) that some material also flows underneath the roller (referred to as backflow) which increases as the roller tilt angle is increased. The roller geometry was found to directly influence the nature of material build up in front of the roller to the extent that there was a critical value of build-up, beyond which material flaked off the part as illustrated in Figure 2.6 (Nagarajan *et al.* (1981)).



Figure 2.6: Material flaking off a formed part from Nagarajan *et al*. (1981)

Essa and Hartley (2009) conducted simulations using an ABAQUS/Explicit model containing 6000 elements of a two-pass process using two rollers off different diameters. Their results showed that using the roller with the smaller nose radius for the conventional spinning process required a greater axial force. In addition, their simulation for the radial force in the single pass process produced a

relationship which demonstrated a general increase in radial force with roller displacement. These simulation results were in agreement with the experimental results of Xia *et al*. (2005).

Hayama *et al*. (1970) found that the roller geometry was also influential in determining whether a part could be formed without wrinkling. They conducted experiments using two rollers, one of nose radius 4mm and one of radius 15mm and report that wrinkle free forming can be achieved with higher feed rates for the smaller roller nose radius. Kobayashi *et al*. (1961) found that the hoop force component decreased as the roller diameter increased whilst Avitzur and Yang (1960) found the hoop force decreased as the roller radius decreased.

### 2.4.3    Blank Thickness and Diameter

Hayama (1974) and Kim *et al.* (2006) found that a positive linear relationship exists between all three force components and the blank thickness. However, both these studies were conducted at low feed rates and for a single half cone angle of $22.5^0$. Hayama *et al*. (1965) also found that increasing the blank diameter also resulted in an increase in the three force components, although this reached a terminal value for blanks of diameter 100mm for the hoop force. Dierig (1992) reports that an increase in blank diameter or sheet thickness resulted in an increase in the axial force.

### 2.4.4    Half Cone angle

Kim *et al*. (2006) conducted an extensive study into shear spinning and found that all three of the force components decreased as the half cone angle increased in what appeared to be a linear fashion, although there are only three data points plotted in each case which renders the nature of the relationship difficult to establish. This relationship was also observed by Kalpakcioglu (1961) and Avitzur and Yang (1960). Kobayashi (1963) proposed a wrinkling limit in terms of the ratio of blank to mandrel diameters and a function, δ, involving the half cone angle of the part and the ratio of the final part thickness to the blank thickness. The theory upon which Kobayashi (1963) proposes this

limit originates from work done by Senior (1956) regarding wrinkling in a different metal forming process.

### 2.4.5   Feed rate

Hayama and Murota (1963), Hayama (1974), Zhan *et al.* (2007), Essa and Hartley (2009) and Xia *et al.* (2005) found the radial and axial forces to increase with increasing feed rate; Avitzur and Yang (1960) and El-Khabeery *et al.* (1991) also found the hoop force to be linearly increasing in nature with feed rate which was attributed to a larger contact area between the roller and the workpiece. For a die-less spinning process, Liu (2007) found that the axial force increased as the feed rate increased. Kim *et al.* (2003) found that the hoop force increased quasi-linearly as the feed rate increased.

### 2.4.6   Mandrel Speed

Wang *et al.* (1989) found that the influence of the speed of rotation of the mandrel had little effect on the forces required to deform the blank. However, there was a general trend for the axial and radial forces to decrease as the mandrel speed increased. However, it should be noted that the geometry used in their investigation was the hemispherical mandrel. Hayama (1974) write that in general, using a higher mandrel rotational speed will result in a better quality finished part; this may be due to the fact that increasing the mandrel speed in isolation (*i.e.* without changing the roller velocity or other process parameters) results in a reduction in the feed rate which has been found to increase the quality of the spun part (Kleiner *et al.* (2005), Slater (1979), El-Khabeery *et al.* (1991), Chen *et al.* (2001)), possibly because more of the workpiece comes into direct contact with the roller. Hayama *et al.* (1965) report that the mandrel rotational speed has a negligible effect on the axial and radial forces whereas Joorabchian and Slater (1979) report that there exists an optimal mandrel rotational speed for which the hoop force is a minimum. For the conventional metal spinning process, Wang *et al.* (1989) report that the mandrel rotational speed did not have a significant effect on the tool forces.

In summary of the findings on the forces in the metal spinning process, it can be seen that the blank thickness, feed rate, cone angle and roller geometry effect the forces in metal spinning. It is also implied (although not explicitly investigated) that the mandrel geometry also affects the forces in metal spinning as the ratio of the force components have been found to vary with the mandrel geometry. However, in order to make more detailed comparisons, a parametric study needs to be undertaken.

### 2.4.7   Roller Paths

Kang *et al.* (1999), Liu *et al.* (2002) and Hayama *et al.* (1970) investigated the effect of using different types of roller path, namely concave, involute and linear as illustrated in Figure 2.7. Liu *et al.* (2002) studied the first path of a conventional spinning process used to form an aluminium cup using a 1mm thick blank of diameter 180mm. They found that the involute curve had the lowest stress and strain values for all components; whilst Kang *et al.* (1999) state that the first pass of a conventional metal spinning process is essentially a shear spinning process. Wang and Long (2011c) found that the highest tool forces were observed when a concave roller path was used and that the greatest reduction in wall thickness was observed for the concave path. They also found that thinning could be accentuated if the curvature of the concave path was increased. Wang *et al.* (2011b) found that where a part wrinkled, the wrinkling occurred in forward passes and reported that wrinkling rarely occurred in backwards passes. They also found that the axial force was the largest force and that larger forces were required to form the part with each successive pass. This was also seen in Essa and Hartley's (2009) results which showed that the axial force was larger in the second pass than in the first pass, a phenomenon that was also observed by Wang and Long (2011c).
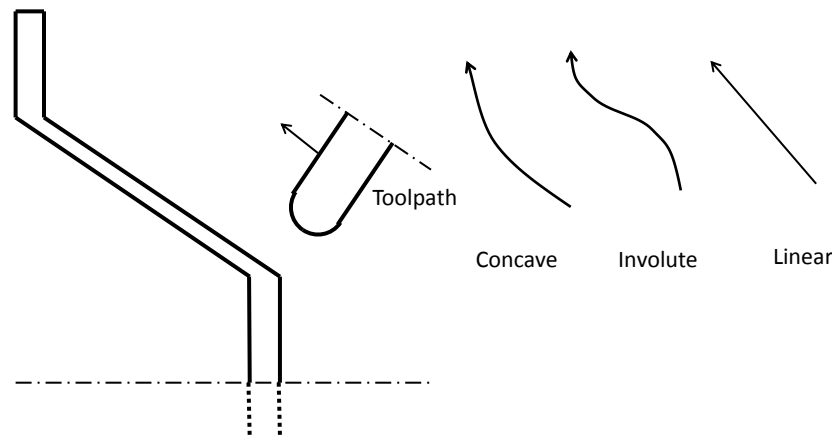
Figure 2.7: Roller path design

## 2.5    Numerical Issues

Modelling the metal spinning process using finite element models can be computationally very expensive. There are essentially two methods which can be employed to reduce the simulation times, namely increasing the processing capability or modelling the process in a way which requires less computational resources. Quigley and Monaghan (2002b) investigated solution times with respect to parallel processing. They found that there was an optimal number of processors (5) to reduce the solution time. For a single processor running on 8400 elements, the solution time per increment was around 900 seconds. Using five processors reduced the time to around 200 seconds but more processors did not improve this much further. The paper suggested that this was due to network issues becoming more significant when more machines were used, since the process was still dependent on a central machine to coordinate the whole process. The fact that the loading mechanism in the spinning process is asymmetric (Razavi *et al.* (2005)) poses a further challenge to building 2d models; however, Mori and Nonanka (2005) and Alberti *et al.* (1989) constructed 2d models in order to reduce simulation times. The model presented by Mori and Nonanka (2005) also assumed an annular forming process and proposed a build-up rate which was compared with experimental data. Alberti *et al.* (1989) assumed an annular forming process, generated by contact between the roller and the workpiece. Whilst a plot of the thickness distribution along the workpiece was presented and

demonstrated thickening towards the open end of the part, there was no comparison with experimental results.

## 2.6    Review of Strain Distribution

For the conventional spinning process, it is assumed that there is no strain in the thickness direction of the part. Therefore, theoretically the hoop strain and the axial strains will be equal to each other from the assumption of constant volume. In the case of shear spinning, the hoop strain is assumed to be zero and consequently, the thickness strain and the axial strains must be equal to each other. Quigley and Monaghan (2000) used this reasoning in order to derive an expression for the strain in the radial direction (although this is the axial direction in Figure 2.2) for a shear spinning process using a conical geometry. Furthermore, they then use a similar rationale to derive an expression for the hoop strain for constant thickness forming using a (theoretically) hemispherical geometry. Their models predicted larger strains for the shear forming process than for the conventional spinning process. They also carried out experiments for single and multiple pass processes. For the single pass process, the measured and predicted radial strains agreed well for approximately one third of the process, despite the fact that the experiments were performed on a hemispherical dome and the shear forming equations had been derived for the conical geometry. However, the hoop strain showed closer agreement with the predicted axial strains for the conventional spinning case. The fact that both the measured radial and hoop strains were tensile over this considered range implies that there is a reduction in thickness, this is also observed experimentally by Beni *et al.* (2010), Quigley and Monaghan (2000), Razavi *et al.* (2005) and in finite element simulations by Wang and Long (2011b). For the multiple pass process, the measured axial strain was largely positive, whilst the measured hoop strain was largely negative, although they did not oppose each other, which would imply that there is some thickness strain present. Furthermore, Quigley and Monaghan (2000) stated that their results showed that the first pass of a conventional spinning process is essentially a shear spinning operation and that multiple passes are required in order to preserve the thickness of the original blank.

This observation was also noted by Köhne (1984) and similarly Kang *et al.*(1999) stated that the first pass of a conventional process determines the final thickness of the part.

For the spinning of cylindrical cups, it is generally found that 'necking' occurs around the corner region of the mandrel and that the formed cup becomes slightly thicker towards the free end of the completed part, Xia *et al.* (2005), Hamilton and Long (2008), Hayama and Murota (1963). Whilst the aforementioned studies only sample one path, Beni *et al.* (2010) considered the average thickness strain across three radial paths and also observed that the (hemispherical) part exhibited thickening towards the circumference of the part. Zhan *et al.* (2007) found that for feed rates greater than 2mm/rev, the minimum wall thickness became greater than that predicted by the sine law. In addition, they found that for feed rates 0.5mm/r to 3mm/r, the maximum wall thickness was approximately the same as the initial blank thickness. These observations are somewhat in agreement with Xia *et al.* (2005) who conducted experiments for feed rates of 0.1, 0.5, 1.0, 1.5, 2.0 and 2.5 mm/rev. and reported that the strain increases with increasing feed rate. Inspection of the presented results shows that for cup depth between 30mm and 50mm, the lowest feed rate resulted in the smallest thickness strain, i.e. smallest deviation from the initial blank thickness. However, for cup depths less than approximately 3mm, Xia *et al.* (2005) found that the highest feed rate resulted in the smallest (absolute value) thickness strain. This would perhaps suggest that in order to produce a part with the same thickness as the initial blank, i.e. to minimise deviation from the original blank thickness, the feed rate should be varied throughout the process, dependent upon the part geometry. Essa and Hartley (2009) also noted that the thinning near the corner of the mandrel was less pronounced in a two pass process than for a single pass process and suggested that a uniform thickness could be achieved through a multi-pass process which is in agreement with the observations made by Quigley and Monaghan (2000).

## 2.7    Review of Stress Distribution

The stress distribution is of particular interest to researchers who are concerned with the phenomena of failure in metal spinning. The widely accepted stress distribution is illustrated in Figure 2.8 where $\sigma_r$ denotes the radial stress (direction 2 in Figure 2.1) and $\sigma_{circ.}$ represents the hoop stress. This distribution predicts tensile radial stresses and compressive hoop stresses as the roller moves away from the tailstock. For roller motion towards the tailstock, both the radial and hoop stresses are predicted as being compressive.
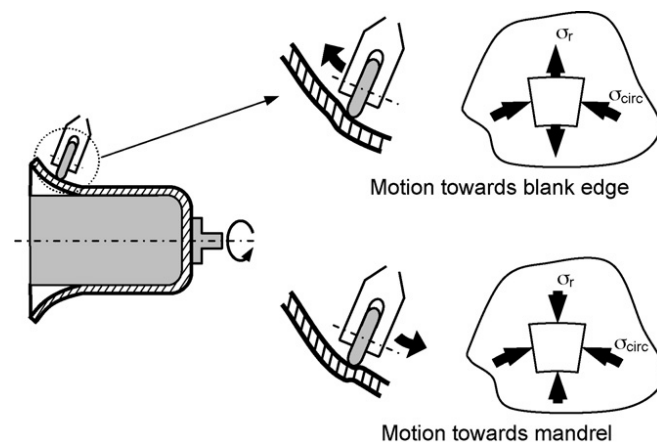
Figure 2.8: Standard stress distribution in conventional spinning (from Music *et al.* 2010).

If compressive hoop stresses generated exceed a critical value, wrinkling occurs in the flange. Xia *et al.* (2005) found that for thinner blanks and larger feed rates, wrinkling occurred whereas (Kobayashi, 1963) found it necessary to increase the mandrel radius as the blank radius increased in order to prevent wrinkling. Zhan *et al.* (2006) found acute thinning to occur at the neck of the mandrel, however, the parts formed in their paper all presented with wrinkles.

However, if tensile hoop stresses are generated and become too large, then radial cracks will emerge. If the radial stress becomes too large, then circumferential cracks may emerge. These failures are shown in Figure 2.9.
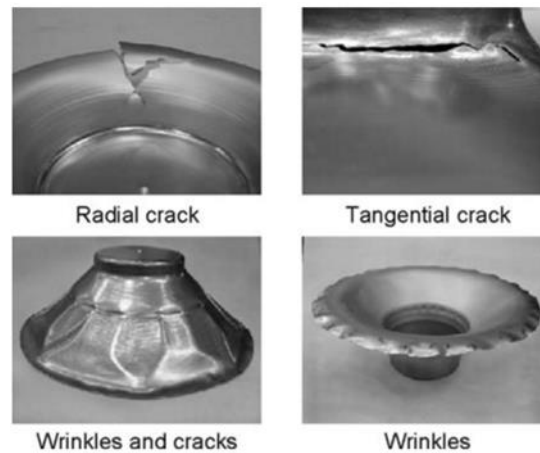
Figure 2.9: Failure modes of circumferential cracking and wrinkling (from Kleiner *et al.* 2002).

In their study of the stress distribution in the spinning of cylindrical cups, Kleiner *et al.* (2002) found that in the early stages of the pass, the hoop stress was close to zero whilst the radial stress increased linearly up until the midpoint between the tailstock and the flange. After this midpoint was reached, compressive hoop stresses began to appear which the authors suggested were responsible for the generation of wrinkles in the flange. In addition, Sebastiani *et al.* (2007) suggest that the onset of wrinkling may even be triggered by the effects of rotating the blank. Whilst there are papers available which study instabilities in rotating discs (Advani 1967, Nowinski (1982)), they are not proposed within the context of the metal spinning process. However, it is interesting to note that Advani (1967) finds that there are two sets of waves which travel in opposite directions around the circumference of a spinning disk. This would appear to relate to the 'toothed' stress pattern observed close to the rim of the workpiece by Sebastiani *et al.* (2006) who suggested that the pattern may be a pre-state to the onset of wrinkling. This stress state was also observed by Wang *et al.* (2011b) in the stress distribution of a backwards pass of a multi-pass process; however, no link was established between the toothed pattern and wrinkling.

It has been found by simulation that the deformation zone is not localised to the immediate vicinity of the roller as stresses have been observed to have been induced in regions which have not been subjected to contact with the roller (Wang *et al.* (2010), Finckenstein (1978), Zhan *et al.* (2006),

Wang and Long (2011b)). Music and Allwood (2011) found that the dominant pressures in forming a part are localised in three distinct regions; they proposed and built a machine to form parts using the spinning process built replacing the mandrel with two rollers. The authors report parts formed with this machine have perfectly flat top and bottom sections.

The effect of the temperatures generated in the spinning process on the stress distribution has not been considered analytically and are not often discussed by researchers, although El-Khabeery *et al.* (1991) suggest that it may be an important factor in the region of contact between the roller and the workpiece. This assertion would appear to agree with Music *et al.* (2010) who report that in practice heat is applied to thick parts and high strength materials in order to reduce the forces required to form the material.

## 2.8    Springback

Springback is the dimensional change which takes place in the part once unloading has taken place. The ability to predict springback is of great industrial importance since springback may render a part unsuitable for its intended purpose. The study of springback within the context of the metal spinning process has been identified by Music *et al.* (2010) as an aspect of the metal spinning process which has not yet been subjected to investigation, hence the key motivation for the author's research project. There is presently no uniformly accepted metric for evaluating springback for the metal spinning process. Within the context of bending, springback can be quantified by measuring the change in bend angle as illustrated in Figure 2.10, this metric has the advantage that it is a non-destructive technique.

Position after springback

θ-δθ

Position before springback

θ
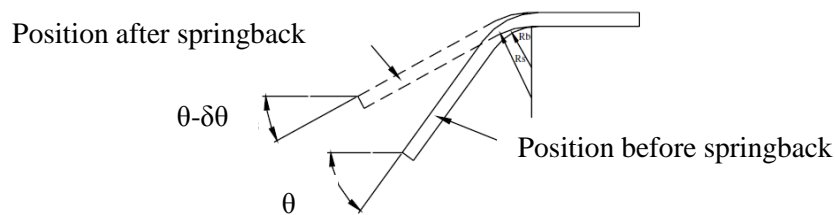
Figure 2.10: Springback measure in bending process (adapted from Ozgur Tekaslan *et al*. (2006)).

Alternatively, Gnaeupol-Herold *et al*. (2005) suggest that the springback in deep drawn cups may be measured by cutting the formed part into a series of rings as illustrated in Figure 2.11. The springback may then be measured by splitting each ring and measuring the angle between the endpoints of each ring.
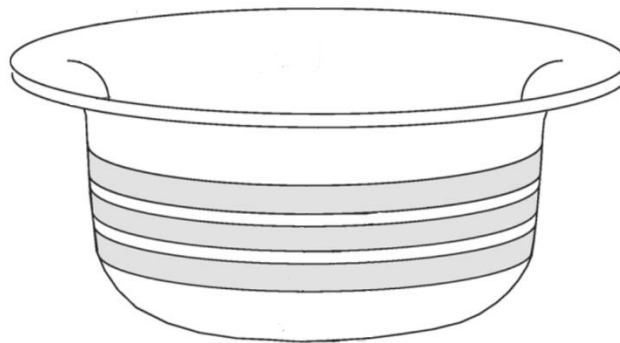


Figure 2.11: Technique for measuring springback in deep-drawn cups (adapted from Gnaeupol-Herold *et al*. (2005)).

Whilst there is no agreed metric for measuring springback in the metal spinning process, Essa and Hartley (2010) defined springback as the maximum deviation from the mandrel diameter. They state that the feed rate affects the springback but that the roller nose radius does not. Bai *et al*. (2008) found that once the process is completed and the release of residual stresses has occurred due to unloading; the stress distribution becomes more homogeneous. Bai *et al*. (2008) consider springback to be a process of self-balance and suggest that springback takes place throughout the forming process as the roller moves over the workpiece. Once the rollers and the mandrel were removed from the workpiece, the authors observed positive springback of $1.8^0$ increase in the half cone angle and a more uniform stress distribution. Zhang *et al*. (2012) acknowledged that springback occurs both during the forming

process and then additionally after unloading. They defined springback in terms of an 'unfitability' (sic) degree which is the distance between the inside of the spun part and the mandrel surface; their results demonstrated that springback did not occur uniformly around the part. Furthermore, Zhang *et al.* (2012) reported a maximum value of unfitability degree in the order of 13mm before unloading and 8mm after unloading. This would indicate that the in-process springback has more of an influence on the final geometry than the springback which can be attributed to unloading the part from the mandrel. In terms of mitigating the amount of springback generated, Kang *et al.* (1999) stated that springback would be greater for a die-less spinning process (possibly due to the absence of a mandrel to restrict the motion of the metal) whilst Ma *et al.* (2010) found that the hardening exponent was the most influential factor on the amount of springback generated.

## 2.9    Conclusions

The reviewed literature has revealed that at the present time, there is agreement amongst researchers that (in isolation) increasing the feed ratio, blank thickness or blank diameter results in an increase in all three force components. Also that increasing the spindle speed has little effect on the axial and radial forces.  The effect of roller design is not yet fully understood, although it is thought that a larger roller diameter or increase in spindle speed (Hayama *et al.* (1965), El-Khabeery *et al.* (1991)) results in a better quality finish on the product. In addition, researchers have concluded that it is not possible to determine the contact area between the roller and the workpiece which has hindered attempts to represent the force components analytically. It is also reported that increasing the feed rate will increase the thickness strain for cylindrical geometries and that using thinner blanks with higher feed rates is more likely to result in the wrinkling of the workpiece. Xia *et al.* (2005) suggest that investigation as to the influence of the mandrel round off radius may be necessary.

## 2.10    Scope of this research

Springback has been identified by Music *et al*. (2010) as one of the areas still in need of investigation by researchers in the field of metal spinning. The effects of process parameters such as feed rate, blank thickness, mandrel rotational speed and half cone angle on the amount of springback observed are also not known. To date, there is no literature which directly compares the shear and conventional metal spinning processes.

The aims of this PhD are to examine the behaviour of springback using a three-dimensional model and then to investigate whether an equivalent two-dimensional modelling tool can be produced to demonstrate representative springback behaviour. Whilst it is anticipated that the two-dimensional model may not accurately reproduce other features of the spinning process, such as a prediction of wrinkling failure, the criterion for success is the investigation of process parameters and their influence on springback using the three-dimensional model and subsequently the development of a two-dimensional model which will accurately reproduce springback results generated in the three-dimensional model.

## §3.    Methodology

### 3.1    Introduction

As was discussed in the literature review, the difficulty in predicting the contact surface area between the blank and the roller precludes directly obtaining an analytical solution to the stress distribution induced by means of the metal spinning process. Therefore, it is necessary to examine alternative computational means of solving the problem.

One method of solving problems which are presented in the form of partial differential equations is the boundary element method. This method requires that (only) the boundary of the solution domain be discretised, this process involves the use of 'boundary functions', the governing equation is then solved on the boundary. Once the boundary solution is known, the solution over the remainder of the solution domain is interpolated via the 'fundamental solutions'. In two dimensional problems, the boundary is represented by straight lines or curves; for three dimensional problems, planar triangles or higher order polygons approximate the boundary and in axisymmetric problems, the boundary is approximated using truncated cones (Kirkup, 2007).

The finite element method is the numerical method of choice for researchers in the field of metal spinning, which was evident in the literature review. The finite element method is a powerful numerical technique employed in situations where the problem to be solved is far too complex to be solved analytically. The finite element method discretises the solution domain into a number of smaller domains called elements, which collectively form a mesh. Throughout each element, individual parameters such as displacement are then interpolated using an isoparametric formulation which is discussed in section 3.7. The local element stiffness matrices are calculated and then assembled into global set of equations which are then solved. The finite element method is used in a wide variety of situations including fluid mechanics, solid mechanics and problems involving heat transfer.

This chapter is split into two sections; the first section contains generic background information, including a derivation of the finite element equations for dynamic analyses, a review of the methods used to solve these equations and a brief review of plasticity and the material model used in this thesis. The second section in this chapter contains information relevant to this thesis problem.

## 3.2      Derivation of the Finite Element Equations

The finite element method procedure consists of solving the governing equations for the displacements then recovering the strains and hence the stresses. Consider the control volume shown in Figure 3.1, making use of Newton's second law and conducting a force balance across the volume (in the x-direction) produces the relation (3.1).
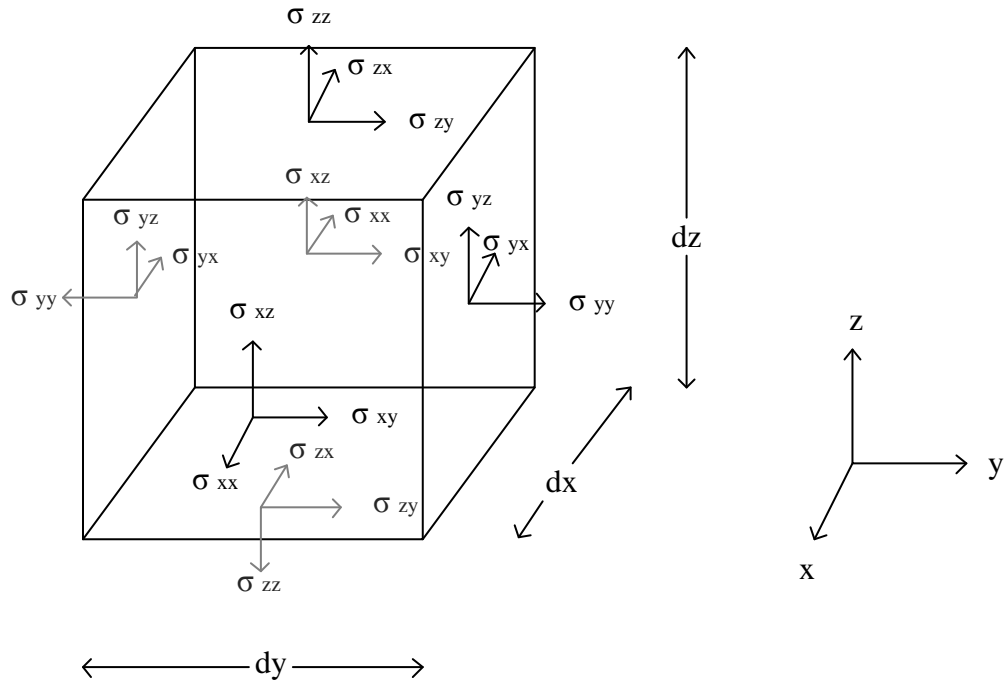


Figure 3.1: Control Volume Showing Internal Stresses

$$\left(\sigma_{xx} + d\sigma_{xx}\right)dydz - \sigma_{xx}dydz + \left(\sigma_{zx} + d\sigma_{zx}\right)dxdy - \sigma_{zx}dxdy + \left(\sigma_{xy} + d\sigma_{xy}\right)dxdz - \sigma_{yx}dxdz = \left(\rho\ddot{u} - f_{x}\right)dxdydz$$

$$(3.1)$$

where $\rho$ is the density of the material under consideration and $\ddot{u}$ represents the acceleration of the body as the second derivative of displacement with respect to time. The term $f_x$ represents the external body forces per unit volume, $f_b$, experienced by the volume in addition to the resistive force per unit volume, $f_d$, experienced by the volume (damping term) and may therefore be written as:

$$f_x = f_b - f_d \tag{3.2}$$

Where viscous damping is implemented, *i.e.*:

$$f_d \propto \dot{u} \tag{3.3}$$

This relationship has been experimentally verified (Pippard, 1978) and is the damping term used by ABAQUS. In this thesis, the constant of proportionality (which is dependent upon the mass of the material) is denoted by the symbol $\kappa$, so that it is possible to write:

$$f_d = \kappa\dot{u} \tag{3.4}$$

Algebraic simplification of expression (3.1), followed by division through the entire expression and then implementing the definition of the partial derivative leads to:

$$\frac{\partial\sigma_{xx}}{\partial x} + \frac{\partial\sigma_{xy}}{\partial x} + \frac{\partial\sigma_{zx}}{\partial x} + f_x = \rho\ddot{u}_x \tag{3.5}$$

Similar equations may be developed for the y and z directions. The principle of virtual work is often used to derive finite element equations and this is the method implemented here. Therefore the next step taken in deriving the finite element equations is to multiply the governing equation (3.5) by an arbitrary virtual displacement and to integrate over the volume of the element to obtain the weak form of the finite element equations. The weak form satisfies the equations in an average sense, hence (3.5) is rewritten as:

$$\int_V \delta_x \frac{\partial\sigma_{xx}}{\partial x} dV + \int_V \delta_x \frac{\partial\sigma_{xy}}{\partial x} dV + \int_V \delta_x \frac{\partial\sigma_{xz}}{\partial x} dV + \int_V \delta_x f_x dV = \int_V \delta_x \rho\ddot{u}_x dV \tag{3.6}$$

The Green-Gauss theorem states that:

$$\iiint_V (\nabla \cdot \underline{\sigma}) dV = \int_S (\underline{\sigma} \cdot \underline{n}) dS \tag{3.7}$$

In order to apply the Green-Gauss theorem, it is useful to introduce the surface boundary condition:

$$t_x = \sigma_{xx} n_x + \sigma_{xy} n_y + \sigma_{xz} n_z \tag{3.8}$$

where $t_x$ may be thought of as the traction (in the $x$-direction) experienced at a point on the surface of the volume; $n_x$, $n_y$ and $n_z$ are components of the normal vector to the surface in the $x$, $y$ and $z$ directions, respectively. Applying the Green-Gauss theorem (3.7) to equation (3.6) and introducing the surface boundary condition (3.8) results in:

$$\int_S \delta_x t_x dS - \int_V \left( \frac{\partial \delta_x}{\partial x} \sigma_{xx} + \frac{\partial \delta_x}{\partial y} \sigma_{xy} + \frac{\partial \delta_x}{\partial z} \sigma_{xz} \right) dV + \int_V \delta_x f_x dV - \int_V \delta_x \rho \ddot{u}_x dV = 0 \tag{3.9}$$

Similar expressions may also be obtained for the y and z directions:

condition (3.8) results in:

$$\int_S \delta_y t_y dS - \int_V \left( \frac{\partial \delta_y}{\partial x} \sigma_{yx} + \frac{\partial \delta_y}{\partial y} \sigma_{yy} + \frac{\partial \delta_y}{\partial z} \sigma_{yz} \right) dV + \int_V \delta_y f_y dV - \int_V \delta_y \rho \ddot{u}_y dV = 0 \tag{3.10}$$

$$\int_S \delta_z t_z dS - \int_V \left( \frac{\partial \delta_z}{\partial x} \sigma_{zx} + \frac{\partial \delta_z}{\partial y} \sigma_{zy} + \frac{\partial \delta_z}{\partial z} \sigma_{zz} \right) dV + \int_V \delta_z f_z dV - \int_V \delta_z \rho \ddot{u}_z dV = 0 \tag{3.11}$$

Summing equations (3.9), (3.10) and (3.11) allows the weak form of the governing equations to be written in matrix form as:

$$\int_S \underline{\delta}^T \underline{t} dS + \int_V \underline{\delta}^T \underline{f} dV - \int_V \rho \underline{\delta}^T \underline{\ddot{u}} dV = \int_V \left( \overline{\nabla} \underline{\delta} \right)^T \underline{\sigma} dV \tag{3.12}$$

where:

$$\overline{\nabla}\underline{\delta} = \begin{pmatrix} \dfrac{\partial \delta_x}{\partial x} \\[2mm] \dfrac{\partial \delta_y}{\partial y} \\[2mm] \dfrac{\partial \delta_z}{\partial z} \\[2mm] \dfrac{\partial \delta_x}{\partial y} + \dfrac{\partial \delta_y}{\partial x} \\[2mm] \dfrac{\partial \delta_x}{\partial z} + \dfrac{\partial \delta_z}{\partial x} \\[2mm] \dfrac{\partial \delta_y}{\partial z} + \dfrac{\partial \delta_z}{\partial y} \end{pmatrix} \tag{3.13}$$

$$\text{and} \qquad \overline{\nabla} = \begin{pmatrix} \dfrac{\partial}{\partial x} & 0 & 0 \\[2mm] 0 & \dfrac{\partial}{\partial y} & 0 \\[2mm] 0 & 0 & \dfrac{\partial}{\partial z} \\[2mm] \dfrac{\partial}{\partial y} & \dfrac{\partial}{\partial x} & 0 \\[2mm] \dfrac{\partial}{\partial z} & 0 & \dfrac{\partial}{\partial x} \\[2mm] 0 & \dfrac{\partial}{\partial z} & \dfrac{\partial}{\partial y} \end{pmatrix} \tag{3.14}$$

Equation (3.12) is to be solved over the whole solution domain in order to recover the displacements, from which the strains, and subsequently the associated stresses may be recovered. The finite element method procedure discretises the solution domain into sub-domains or 'elements' which make use of isoparametric formulation, *i.e.* that displacements across an element are interpolated using the same shape functions which define the geometry of the element. The number of shape functions for an element is equal to the number of nodes, *n*, in that element; each shape function obeys:

$$N_i = \begin{cases} 1 & \text{at node } i \\ 0 & \text{at all other nodes} \end{cases} \qquad i=1,...,n \tag{3.15}$$

The shape functions used vary depending on the number of nodes in an element and the degree of interpolation required. The shape functions used in this thesis and more detail regarding isoparametric formulation will be given in the second part of the chapter. The global displacement vector $\underline{u}$ (which has dimensions 3nx1 in 3D analyses) has the assumed form:

$$\underline{u} = \underline{N}\,\underline{a} \qquad\qquad (3.16)$$

where $\underline{a}$ holds the nodal displacements. It is now possible to use this isoparametric relationship to rewrite the governing equations given in (3.12). Returning to equations (3.12), recall that $\underline{\delta}$ is an arbitrary vector of virtual displacements, it follows from (3.16) that $\underline{\delta}$ may be written as:

$$\underline{\delta} = \underline{N}\,\underline{C} \qquad\qquad (3.17)$$

where $\underline{C}$ is an arbitrary matrix. Using relation (3.17), it is then possible to write

$$\overline{\nabla}\underline{\delta} = \underline{B}\,\underline{C} \qquad\qquad (3.18)$$

where

$$\underline{B} = \overline{\nabla}\underline{N} \qquad\qquad (3.19)$$

Furthermore, the strain relation is introduced as:

$$\underline{\varepsilon} = \overline{\nabla}\underline{u} = \underline{B}\,\underline{a} \qquad\qquad (3.20)$$

and the relationship between stress and strain is determined to be:

$$\underline{\sigma} = \underline{D}\{\underline{\varepsilon} - \underline{\varepsilon}_0\} = \underline{D}\,\underline{B}\,\underline{a} - \underline{D}\,\underline{\varepsilon}_0 \qquad\qquad (3.21)$$

Where $\underline{\varepsilon}$ contains the strains, $\underline{\varepsilon}_0$ contains the (known) initial strains and $\underline{D}$ is the constitutive matrix containing the relationship between the stress and strain vectors.

The precise nature of $\underline{D}$ depends upon the material model used and may vary throughout the analysis in nonlinear elastoplasticity modelling and the construction of appropriate constitutive models to represent experimentally observed behaviour is "extremely complex" as pointed out by Zienkiewicz and Taylor (2005). In nonlinear elastoplasticity modelling, the nature of $\underline{D}$ accounts for the fact that strains can be considered as the sum of elastic strains and plastic strains (equation (3.64), repeated here for convenience).

$$\underline{\varepsilon} = \underline{\varepsilon}^e + \underline{\varepsilon}^p \tag{3.64}$$

where the superscripts $e$ and $p$ respectively denote the elastic and plastic components of the total strain. In nonlinear elastoplasticity modelling, the stresses and strains are assumed to have a rate relationship which may be written as

$$\dot{\underline{\sigma}} = \underline{D}\dot{\underline{\varepsilon}} \tag{3.22}$$

Where the rate form of equation (5.52) is adopted, namely

$$\dot{\underline{\varepsilon}} = \dot{\underline{\varepsilon}}^e + \dot{\underline{\varepsilon}}^p \tag{3.23}$$

In this relationship, the plastic strain is characterised by a flow rule of the form

$$\dot{\underline{\varepsilon}}^p = \dot{\lambda}\underline{h} \tag{3.24}$$

where $\underline{h}$ represents the direction of plastic flow and is given by

$$\underline{h} = \frac{\partial g}{\partial \underline{\sigma}} \tag{3.25}$$

where g is known as the plastic potential (Lubliner, 2008), in associated flow rules, the quantity g is taken to be the same as the yield surface f as the plastic flow is associated with the yield surface; in non-associated flow models, g is not the same as f. The quantity $\dot{\lambda}$ is a plastic consistency parameter which controls the magnitude of the plastic strains (Coombs, 2011). It is readily seen that the Karush-Kuhn-Tucker conditions of optimisation theory are satisfied, since

$$\dot{\lambda}f = 0 \tag{3.26}$$

$$\dot{\lambda} \geq 0 \tag{3.27}$$

$$f \leq 0 \tag{3.28}$$

In nonlinear elastoplasticity, equation (3.23) is substituted into (3.22) to give

$$\underline{\dot{\sigma}} = \underline{D}\left[\underline{\dot{\varepsilon}}^e - \underline{\dot{\varepsilon}}^p\right] \tag{3.29}$$

whereupon the plastic flow rule is then incorporated and hence

$$\underline{\dot{\sigma}} = \underline{D}\left[\underline{\dot{\varepsilon}}^e - \dot{\lambda}\underline{h}\right] \tag{3.30}$$

The precise nature of $\dot{\lambda}$ depends on the inclusion of internal material parameters in the material model, these internal material parameters provide detail of the material deformation history. Where these material parameters – represented by $\underline{\chi}$ have been included, the condition for hardening elastoplasticity is (Coombs (2011))

$$\dot{f} = \left[\frac{\partial f}{\partial \sigma}\right]^T \underline{\dot{\sigma}} + \left[\frac{\partial f}{\partial \chi}\right]^T \underline{\dot{\chi}} \tag{3.31}$$

and the internal variable rate is related to the plastic consistency parameter via the relation

$$\underline{\dot{\chi}} = \dot{\lambda}\underline{H}_\chi \tag{3.32}$$

where $\underline{H}_\chi$ defines the instantaneous evolution of the material parameters (Coombs (2011)). It is then possible to substitute (3.30) and (3.32) into (3.31) in order to obtain a relation for $\dot{\lambda}$ which is then

substituted back into (3.30) to give the instantaneous change in rate of stress with strain relationship as

$$\dot{\underline{\sigma}} = \underline{D}\left[ [I] - \frac{\dfrac{\partial g}{\partial \underline{\sigma}}\left[\dfrac{\partial f}{\partial \underline{\sigma}}\right]^{T}\underline{D}}{\left[\dfrac{\partial f}{\partial \chi}\right]^{T}H_{\chi} + \left[\dfrac{\partial f}{\partial \sigma}\right]^{T}\underline{D}\dfrac{\partial g}{\partial \underline{\sigma}}} \right]\dot{\underline{\varepsilon}} \tag{3.33}$$

For a detailed description of these substitutions, the reader is referred to Coombs (2011).

Returning to the derivation of the finite element equations, substitution of relations (3.17) and (3.21)

$$\int_{S}\underline{N}^{T}\,\underline{C}^{T}\,\underline{t}dS + \int_{V}\underline{N}^{T}\,\underline{C}^{T}\left(\underline{f}_{b} - \kappa\underline{N}\dot{\underline{a}}\right)dV - \int_{V}\rho\underline{N}^{T}\,\underline{C}^{T}\,\underline{N}\ddot{\underline{a}}dV = \int_{V}\underline{B}^{T}\,\underline{C}^{T}\left(\underline{D}\underline{B}\underline{a} - \underline{D}\underline{\varepsilon}_{0}\right)dV \tag{3.34}$$

where the force term has been split into the two components previously mentioned in (3.2). Since the matrix $\underline{C}$ is arbitrary, it may legitimately be chosen to be the identity matrix. This then allows (3.34) to be rewritten in the recognisable form found in many textbooks:

$$\underline{M}\,\ddot{\underline{a}} + \underline{R}\,\dot{\underline{a}} + \underline{K}\,\underline{a} = \underline{H} \tag{3.35}$$

where

$$\underline{M} = \int_{V}\rho\underline{N}^{T}\,\underline{N}dV \tag{3.36}$$

$$\underline{R} = \int_{V}\underline{N}^{T}\kappa\underline{N}dV \tag{3.37}$$

$$\underline{K} = \int_{V}\underline{B}^{T}\,\underline{D}\underline{B}dV \tag{3.38}$$

$$\underline{H} = \int_V \underline{B}^T \underline{D} \underline{\varepsilon}_0 dV + \int_S \underline{N}^T \underline{t} dS + \int_V \underline{N}^T \underline{f}_b dV \tag{3.39}$$

Equation (3.13) represents the equations solved in dynamic analyses, the matrix $\underline{M}$ is referred to as the mass matrix, the matrix $\underline{R}$ as the damping matrix and the matrix $\underline{K}$ is referred to as the stiffness matrix. In static analyses; the first two terms in equation (3.35) are omitted. Having established the governing equations for the analyses, this section of the thesis continues by looking at the solution methods used in solving these equations. ABAQUS uses two methods to solve the finite element equations, the implicit solution method and the explicit solution method.

### 3.3    Explicit Solution Method

The ABAQUS/Explicit package uses the central difference method to approximate differential terms. The central difference operators are (Bathe, 1982):

$$\dot{a}_t = \frac{a_{t+\Delta t} - a_{t-\Delta t}}{2\Delta t} \tag{3.40}$$

Similarly;

$$\ddot{a}_t = \frac{\dot{a}_{t+\Delta t} - \dot{a}_{t-\Delta t}}{2\Delta t} \tag{3.41}$$

$$\ddot{a}_t = \frac{1}{(\Delta t)^2} \left( a_{t+\Delta t} - 2a_t + a_{t-\Delta t} \right) \tag{3.42}$$

By eliminating $a_{t+\Delta t}$ from (3.40) and (3.42), then halving the time step, relation (3.43) is obtained.

$$a_{t-\Delta t} = a_t - (\Delta t)\dot{a}_t + \frac{(\Delta t)^2}{2} \ddot{a}_t \tag{3.43}$$

Relation (3.43) is used in order to initialise the solution procedure.

The governing equation (3.35) is rewritten as:

$$\underline{M}\,\underline{\ddot{a}} = \underline{H} - \left[\underline{R}\,\underline{\dot{a}} + \underline{K}\,\underline{a}\right] = \underline{H} - \underline{F}^{\,\text{int}} = \underline{F}^{\,residual} \tag{3.44}$$

Therefore, the acceleration can be found by solving:

$$\underline{\ddot{a}} = \underline{M}^{\,-1`}\,\underline{F}^{\,residual} \tag{3.45}$$

The solution procedure assumes that the initial displacements and velocities are known at time t=0; therefore the initial acceleration, $\ddot{a}_0$ is calculated from equation (3.45) using equations (3.20) and (3.21):

$$\underline{\ddot{a}}_0 = \underline{M}^{\,-1}\left[\underline{H} - \left[\underline{R}\,\underline{\dot{a}}_0 + \underline{K}\,\underline{a}_0\right]\right] \tag{3.46}$$

Once the initial acceleration has been evaluated, the values of $\underline{a}_0$, $\underline{\dot{a}}_0$ and $\underline{\ddot{a}}_0$ are substituted into (3.43) to find $\underline{a}_{-\Delta t}$. Equation (3.40) is used (replacing $t$ with $-\dfrac{\Delta t}{2}$) to find $\underline{\dot{a}}_{-\frac{\Delta t}{2}}$, following which, $\underline{\dot{a}}_{\frac{\Delta t}{2}}$ is found using equation (3.41) and is then substituted back into equation (3.40) to find $a_{\Delta t}$. Then equation (3.41) with the initial velocity, $\underline{\dot{a}}_0$ is used with a half time step alongside the assumption that the acceleration is constant across the whole time step (*i.e.* that $\underline{\ddot{a}}_{\frac{\Delta t}{2}} = \underline{\ddot{a}}_0$) to calculate $\underline{\dot{a}}_{\Delta t}$. Equation (3.46) is then used to calculate $\underline{\ddot{a}}_{\Delta t}$ and the procedure is repeated until the total simulation time has been reached.

The key advantage of the central difference method is that the solution can essentially be obtained at element level, thereby requiring comparatively little storage; consequently very large systems may be solved effectively (Bathe, 1982).  The solution process implies that another advantage of using the central difference method for explicit integration is that the cost of the analysis increases linearly with problem size (ABAQUS, 2010). However, the disadvantage of this method is that it is only conditionally stable and in order to obtain a valid solution the time step must satisfy:

$$\Delta t \le \Delta t_{cr} = \frac{T_n}{\pi} \tag{3.47}$$

where $T_n$ is the smallest period of the assembly with n degrees of freedom (Bathe, 1982), *i.e.* the largest time taken for a stress wave to propagate across an element (Bathe, online lectures), which is naturally dependent upon the length of the longest element in the mesh and the material properties used in the simulation. This implies that for an optimal time step to be chosen, the mesh should be uniform (Bathe, online lectures), however the disadvantage of this is that the finer the mesh, the greater the number of equations there are to be solved at each time increment. Whilst it is possible to calculate an estimate of the lower bound of $T_n$ (Bathe, 1982), these details are beyond the scope of this thesis since these calculations are performed by the ABAQUS software and the interested reader is referred to (Bathe, 1982) for further details. However, it should be noted that the value of the critical time increment may change throughout the solution.

## 3.4     Implicit Solution Method

ABAQUS/Standard uses the Newmark implicit solution method to solve the finite element equations. The standard Newmark method presented here follows that presented by Bathe (1982). Equation (3.43) is modified as follows:

$$\underline{a}_{t+\Delta t} = \underline{a}_t + (\Delta t)\underline{\dot{a}}_t + (\Delta t)^2 \left[ \left( \frac{1}{2} - \beta \right) \underline{\ddot{a}}_t + \beta \underline{\ddot{a}}_{t+\Delta t} \right] \tag{3.48}$$

where $\beta$ is a constant. Furthermore, introducing another constant, $\gamma$, it is possible to write:

$$\underline{\dot{a}}_{t+\Delta t} = \underline{\dot{a}}_t + (\Delta t)\left[ (1 - \gamma)\underline{\ddot{a}}_t + \gamma \underline{\ddot{a}}_{t+\Delta t} \right] \tag{3.49}$$

The parameters $\beta$ and $\gamma$ are chosen to obtain stability and accuracy of the integration (Bathe, 1982). Equation (3.48) is rearranged in order to obtain $\underline{\ddot{a}}_{t+\Delta t}$ in terms of $\underline{a}_{t+\Delta t}$ :

$$\underline{\ddot{a}}_{t+\Delta t} = \frac{1}{\beta(\Delta t)^2}\left[ \underline{a}_{t+\Delta t} - \underline{a}_t \right] - \frac{\underline{\dot{a}}_t}{\beta \Delta t} - \left( \frac{1}{2\beta} - 1 \right)\underline{\ddot{a}}_t \tag{3.50}$$

Expression (3.50) is then substituted into (3.49) to give:

$$\dot{\underline{a}}_{t+\Delta t} = \left(1 - \frac{1}{\beta}\right)\dot{\underline{a}}_t + \left(2\Delta t - \gamma\Delta t - \frac{\Delta t}{2\beta}\right)\ddot{\underline{a}}_t + \left(\frac{\gamma}{\beta(\Delta t)}\right)\underline{a}_{t+\Delta t} - \frac{\gamma}{\beta(\Delta t)}\underline{a}_t \qquad (3.51)$$

The only unknown terms in relations (3.50) and (3.51) is $\underline{a}_{t+\Delta t}$; relations (3.50) and (3.51) are

substituted into equation (3.35) at time $t + \Delta t$ and then the system is solved for $\underline{a}_{t+\Delta t}$ using an

iterative procedure such as the Newton-Raphson process. Once $\underline{a}_{t+\Delta t}$ has been obtained, relations

(3.48) and (3.49) are used to evaluate $\ddot{\underline{a}}_{t+\Delta t}$ and $\dot{\underline{a}}_{t+\Delta t}$. The key advantage of the implicit solution

method over the explicit solution method is that the implicit solution method is unconditionally stable

for β=0.25 and γ=0.5, therefore there is no restriction on the time step used. However, because the

stiffness matrix $\underline{K}$ needs to be formed at every increment, a large amount of storage capacity is

required.

## 3.5    Mass Scaling

Using the explicit solution method can involve very long simulation times at great cost for the reasons

already stated in section 3.2. ABAQUS offers mass scaling as a method of reducing the time taken to

run a simulation. Since the metal spinning process involves a high degree of nonlinear deformation, a

typical run-time for the forming of a cone using a single pass is over 37 hours, mass scaling has been

employed in this thesis. The critical time step was stated as (3.47), however, in a static analysis, the

critical time step for the central difference method may be determined to be

$$\Delta t_{crit} = L^e \sqrt{\frac{\rho}{E}} \qquad (3.52)$$

Where $L^e$ is the element length, ρ is the material density and E is the Young's modulus. From

equation (3.52), it is seen that artificially increasing the material density, equivalent to 'scaling the

mass' by a factor of $j^2$. This results in an increase in the stable time increment by a factor of j, thereby

reducing the overall solution time by factor j. Whilst mass scaling can be very beneficial in terms of

reducing the computational costs of a simulation, the effects of mass scaling on the inertial effects in the simulation can lead to erroneous results if excessive mass scaling is used (ABAQUS, 2010). In order to control the effects of mass scaling, it is recommended (ABAQUS, 2010) that the ratio of kinetic energy to internal energy does not exceed ten per cent.

## 3.6    Hourglassing and Locking

In the previous section, it was demonstrated that the internal energy output is used to monitor the effects of mass scaling; in addition to this, the internal energy is also used to monitor another potential concern, namely hourglassing. Hourglassing and another phenomenon called locking may cause a simulation to abort or produce erroneous results. There are three types of locking, namely volumetric locking, which occurs in fully integrated elements, where the quadrature is sufficient to provide the exact integrals in the expression for the stiffness matrix terms, if the element is undistorted. Another form of locking is shear locking, which occurs in fully integrated elements subjected to bending; and membrane locking which occurs in shell elements. Locking results in elements becoming overly stiff owing to a densely populated stiffness matrix which is a direct result of fully integrated elements. In order to greatly reduce the risk of locking, it is recommended (Zienkiewicz and Taylor, 1989) to employ elements which make use of reduced integration. The disadvantage of using reduced integration in elements is that such elements are susceptible to 'hourglassing'. Hourglassing is a phenomenon which occurs due to spurious deformation modes as shown in Figure 3.2. The mode of deformation is such that a zero strain energy mode is perceived at an integration point at the centre of the
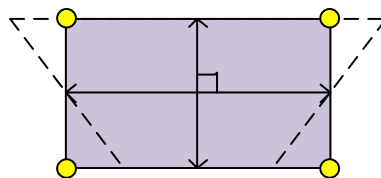


Figure 3.2: Deformation of a single element

element since no change in dimension is detected at right angles to the point as indicated by the arrowed lines in Figure 3.2. Since no strain energy is attributed to the element, the element becomes too 'soft'; in order to correct for this phenomenon, artificial strain energy is added to the system. To ensure that the amount of strain energy added to the system is sufficient to control potential hourglassing whilst not adversely influencing the results of the simulation, Simula (ABAQUS, 2010), the developers of the commercial software ABAQUS, recommend that in order to avoid hourglassing, the ratio of the artificial strain energy to internal energy should not exceed ten per cent.

## 3.7     Material Modelling

It has already been demonstrated in section 3.4 that the material properties influence the calculation of an appropriate time step for use in the explicit dynamic solution. This section includes a brief introduction to plasticity and the material model used in this thesis.

### 3.7.1   Principal Stress Space

The components of the Cauchy stress may be written in matrix form as:

$$[\sigma] = \begin{bmatrix} \sigma_{xx} & \sigma_{xy} & \sigma_{xz} \\ \sigma_{yx} & \sigma_{yy} & \sigma_{yz} \\ \sigma_{zx} & \sigma_{zy} & \sigma_{zz} \end{bmatrix} \tag{3.53}$$

where it may be demonstrated that this stress matrix is symmetric (Lubliner, 2008). For each point in a body, the coordinate axes x, y, z may be oriented such that the shear stresses vanish and only the stresses $\sigma_{xx}$, $\sigma_{yy}$ and $\sigma_{zz}$ remain; these stresses are known as the principal stresses. In terms of the principal stress tensor:

$$[\sigma'] = \begin{bmatrix} \sigma_1' & 0 & 0 \\ 0 & \sigma_2' & 0 \\ 0 & 0 & \sigma_3' \end{bmatrix} \tag{3.54}$$

The relationship between the general stress state (3.54) and the principal stress state may be written as:

$$[\sigma] = [T][\sigma'][T]^T \tag{3.55}$$

where the matrix $[T]$ is a rotational transformation matrix

### 3.7.2   von Mises Yield Criterion

It is possible for a specimen of material to exhibit plastic deformation even though each of the principal stresses is has a value lower than the yield stress. Therefore, it is necessary to postulate a yielding criterion in order to accommodate this phenomenon. Two of the most popular yielding criteria are the von Mises yield criterion and the Tresca yield criterion. In order to discuss the von Mises yield criterion, it is first necessary to consider the deviatoric stress tensor. The Cauchy stress tensor (3.53) may be written in terms of two components known as the volumetric stress tensor (sometimes referred to as the hydrostatic stress tensor or the pressure tensor) which is the stress associated with a change in volume of the domain under consideration; and the deviatoric stress tensor which is associated with shearing deformation.

The deviatoric stress tensor, [s] is:

$$[s] = [\sigma] - \frac{I_1}{3}[I] \tag{3.56}$$

where $I_1 = tr[\sigma]$ and $\frac{I_1}{3}[I]$ is known as the mean stress.

The principal axes of $[s]$ are the same as for $[\sigma]$ and the principal invariants of the deviatoric stress are defined as:

$$J_1 = s_{xx} + s_{yy} + s_{zz} = 0 \tag{3.57}$$

$$J_2 = \frac{1}{2}tr(s)^2 = \frac{1}{2}\left((\sigma_1 - \sigma_2)^2 + (\sigma_2 - \sigma_3)^2 + (\sigma_3 - \sigma_1)^2\right) \tag{3.58}$$

where $\sigma_i \quad i = 1,2,3$ are the principal stresses and to specify a unique orientation:

$$\sigma_1^{'} \geq \sigma_2^{'} \geq \sigma_3^{'} \tag{3.59}$$

The third principal invariant of the hydrostatic stress tensor is:

$$J_3 = \frac{1}{3}tr(s)^3 \tag{3.60}$$

In terms of the principal stresses, the von Mises yield criterion is defined as:

$$\sigma_Y = \sqrt{3J_2} = \sqrt{\frac{1}{2}\left((\sigma_1 - \sigma_2)^2 + (\sigma_2 - \sigma_3)^2 + (\sigma_3 - \sigma_1)^2\right)^{\frac{1}{2}}} \tag{3.61}$$

In terms of the Cauchy stress tensor, the von Mises yield criterion is defined as:

$$\sigma_Y = \sqrt{3J_2} = \sqrt{\frac{1}{2}\left((\sigma_{xx} - \sigma_{yy})^2 + (\sigma_{yy} - \sigma_{zz})^2 + (\sigma_{zz} - \sigma_{xx})^2 + 6(\sigma_{xy}^2 + \sigma_{yz}^2 + \sigma_{zx}^2)\right)^{\frac{1}{2}}} \tag{3.62}$$

where in both cases, $\sigma_Y$ is the yield stress of the material in tensile stress. This yield criterion presents a yield surface consisting of a cylinder of radius $\sigma_Y\sqrt{\frac{2}{3}}$ centred on an axis corresponding to $\sigma_{xx} = \sigma_{yy} = \sigma_{zz}$, which is known as the hydrostatic axis and is shown in Figure 3.3 as the "space diagonal".
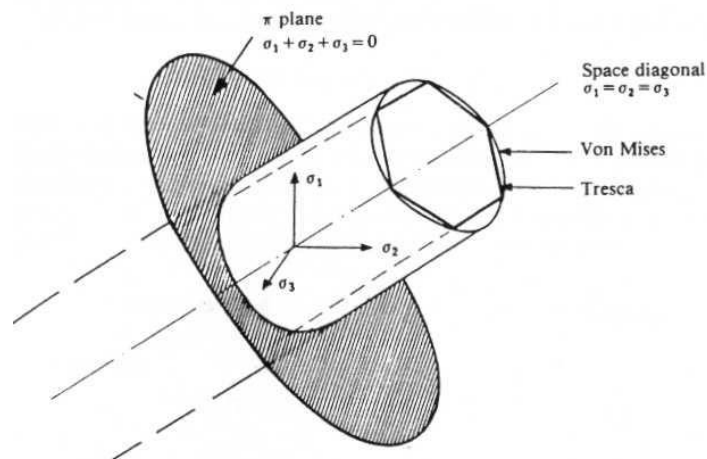
Figure 3.3: von Mises Yield Surface (Owen and Hinton (1980))

Values of Cauchy stress which when substituted into (3.62) yield a value less than the von Mises yield criterion correspond to points inside the yield surface, whereas values of deviatoric stress equal to the von Mises yield criterion (equation 3.62) lie on the yield surface. Also shown in Figure 3.3 is the Tresca yield criterion which states that the material yields when the maximum shear stress on all planes reaches the yield stress in shear of the material (Lubliner 2008) and is written as:

$$\max\left(\left(\sigma_1 - \sigma_2\right),\left(\sigma_2 - \sigma_3\right),\left(\sigma_3 - \sigma_1\right)\right) = \frac{\sigma_Y}{2} \tag{3.63}$$

It is seen in Figure 3.3, that the Tresca yield criterion is a more conservative model for plastic behaviour. The work presented in this thesis uses the von Mises yield criterion throughout.

### 3.7.3    Plastic strains

One of the fundamental concepts of Plasticity theory states that the strain experienced by a material may be decomposed into elastic and plastic strain components, *i.e.* that it is possible to write:

$$\{\varepsilon\} = \{\varepsilon^e\} + \{\varepsilon^p\} \tag{3.64}$$

where the superscripts *e* and *p* respectively denote the elastic and plastic components of the total strain. In the elastic range, the relationship between the stress and strain may be assumed to be linear; and the ratio of stress to strain may be taken to equal to the Young's Modulus of the material. Once the material has yielded, the stress state is on the yield surface and the aforementioned assumptions are no longer valid, and strain hardening (where the material appears stronger as a result of plastic deformation) occurs. In order to explore this notion further, it is necessary to first consider the uniaxial case as illustrated in Figure 3.4.
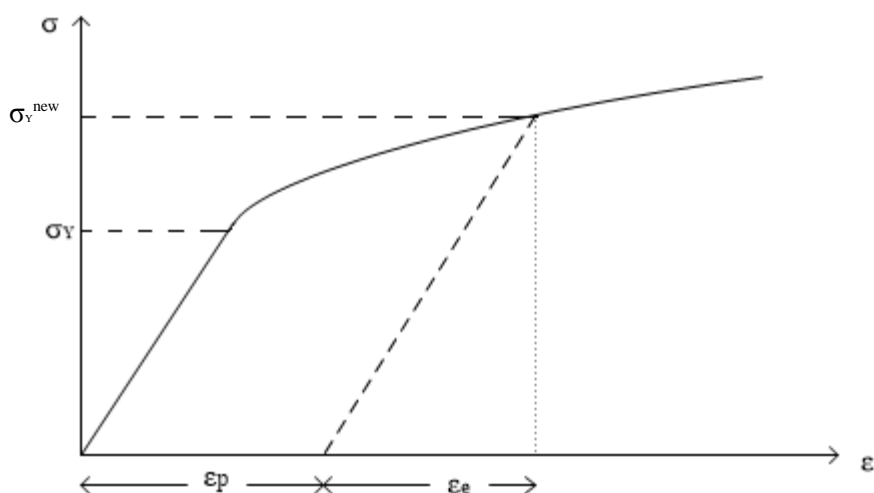


Figure 3.4: Sample 1-D stress-strain graph

Beyond the yield stress, the deformation which occurs is referred to as elasto-plastic (Lubliner, 2008); furthermore, if the material is unloaded beyond the yield stress, the stress-strain relationship follows a path parallel to the initial loading. This is shown by the dashed line in Figure 3.6, the strain which is not recovered is the plastic component of the total strain and the strain which is recovered is referred to as the elastic strain. If the material were to be reloaded, the loading path would follow the dashed line, up to the 'new yield stress', $\sigma_Y^{new}$. In the uniaxial case, the elasto-plastic stress-strain relationship may be modelled using the Ludwick's Law (Dixit and Dixit, 2008):

$$\sigma = \sigma_Y + K\varepsilon_p^{\,h} \tag{3.65}$$

where *h* is known as the strain hardening exponent which can be used to model uniaxial tensile test data, as will be shown in the latter part of this chapter; K is referred to as a strength coefficient. In terms of multiaxial models, there are two ways in which strain hardening is accommodated using the three dimensional yield surface, namely kinematic hardening and isotropic hardening. Isotropic hardening accommodates the increase in yield stress, $\sigma_Y^{'}$ by means of expanding the yield surface (*i.e.* the hydrostatic axis remains in its original position whilst its radius increases). This phenomenon is illustrated in Figure 3.5.
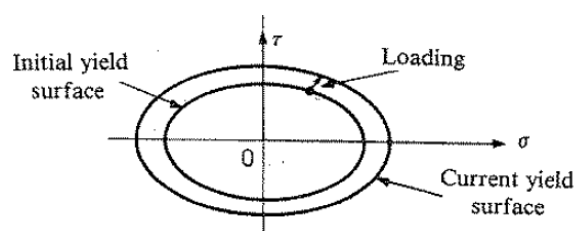


Figure 3.5: Isotropic hardening (Owen and Hinton (1980))

Alternatively, the Kinematic hardening model assumes that the dimensions of the yield surface remain the same and that $\sigma_Y^{'}$ is accommodated by translation of the hydrostatic axis, as shown in Figure 3.6.
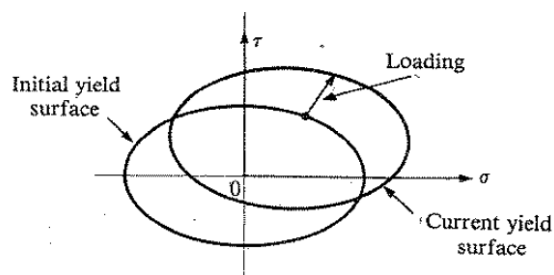


Figure 3.6: Kinematic hardening (Owen and Hinton (1980))

Consideration of the two models yields to the conclusion that during unloading, the elastic range is greater for the isotropic hardening model than for the kinematic hardening model.

### 3.7.4    Material model used in this thesis

The material model for mild steel adopted in this thesis adopts the format of (3.65) and is fitted to experimental tensile-test data obtained byWang (2012), the relationship (in MPa) transpires to be:

$$\sigma = 197 + 434\varepsilon^{0.572} \tag{3.65a}$$

Furthermore, the material is assumed to be isotropic and the von Mises yield criterion is applied. The Young's Modulus of the material (represented by the gradient of the line in Figure 3.4 between the origin and $\sigma_Y$) is taken to be 197 GPa and the density of the material is taken to be 7850 kgm$^{-3}$; the Poisson's ratio is taken to be 0.3. Both the experimental data and the curve fit are shown in Figure 3.7.
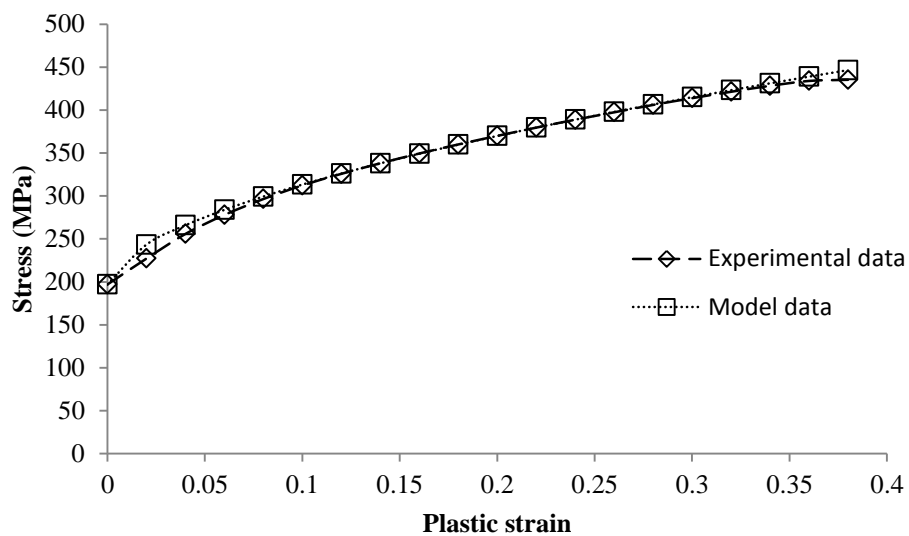
Figure 3.7: Comparison of experimental data and Material Model

# §PART 2: SPECIFICS.

## 3.8      Isoparametric Formulation

As was mentioned in section 3.1, the governing equations are solved over the whole domain using elements which use isoparametric formulation. The elements used employ an isoparametric formulation using shape functions to interpolate the displacements; the same shape functions are used to interpolate any scalar parameter such as temperature. This section establishes the $\underline{B}$ and $\underline{N}$ matrices required for substitution into expressions (3.36)-(3.39) in order to calculate the mass, stiffness and damping matrices for a domain discretised using eight noded hexahedral elements. The concept assumes that each element is mapped to an idealised element as shown in Figure 3.8
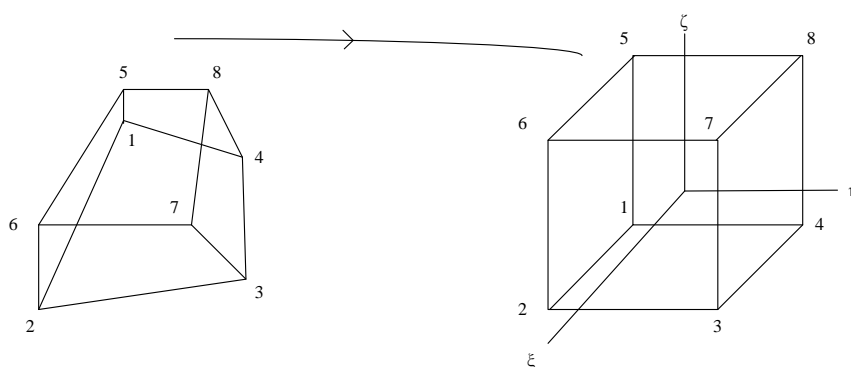


Figure 3.8: Mapping of an 8 noded hexahedral element.

The idealised element operates a coordinate system $(\xi,\eta,\varsigma)$ with its origin at the centre of the element with $\xi,\eta,\varsigma \quad \in [-1,1]$. The element in Figure 3.8 has eight nodes and therefore eight shape (interpolation) functions are required for interpolation in this element. Each shape function is equal to unity at its corresponding node and is zero at all other nodes as stated in (3.15). The shape functions used in the three dimensional analyses in this thesis are:

$$N_1 = \frac{1}{8}(1-\xi)(1-\eta)(1-\varsigma)$$

$$N_2 = \frac{1}{8}(1+\xi)(1-\eta)(1-\varsigma)$$

$$N_3 = \frac{1}{8}(1+\xi)(1+\eta)(1-\varsigma)$$

$$N_4 = \frac{1}{8}(1-\xi)(1+\eta)(1-\varsigma)$$

$$N_5 = \frac{1}{8}(1-\xi)(1-\eta)(1+\varsigma)$$

$$N_6 = \frac{1}{8}(1+\xi)(1-\eta)(1+\varsigma)$$

$$N_7 = \frac{1}{8}(1+\xi)(1+\eta)(1+\varsigma)$$

$$N_8 = \frac{1}{8}(1-\xi)(1+\eta)(1+\varsigma)$$

$$(3.66) - (3.73)$$

The coordinates of any point within an element are given by:

$$x = \sum_{i=1}^{8} N_i x_i$$
$$y = \sum_{i=1}^{8} N_i y_i \qquad (3.74\text{-}3.76)$$
$$z = \sum_{i=1}^{8} N_i z_i$$

Where the $N_i$ are the shape functions for the eight noded hexahedral element given by equations (3.66)-(3.73) and $x_i$, $y_i$ and $z_i$ are the coordinates of each node. Recall, the aim is to evaluate the matrices:

$$\underline{M} = \int_V \rho \underline{N}^T \underline{N} dV \qquad (3.36)$$

$$\underline{R} = \int_V \underline{N}^T \kappa \underline{N} dV \qquad (3.37)$$

$$\underline{K} = \int_V \underline{B}^T \underline{D} \underline{B} dV \qquad (3.38)$$

$$\underline{B} = \overline{\nabla} \underline{N} \qquad (3.19)$$

52

for the idealised element. In order to calculate $\underline{B}$ it is necessary to establish a shape function matrix

of dimension d x dn where d is the number of spatial dimensions and n is the number of nodes in the

element, therefore, in the case of an eight noded hexahedral element, $\underline{N}$ has dimensions 3 x 24 and is

written:

$$\underline{N} = \begin{bmatrix} N_1 & 0 & 0 & N_2 & 0 & 0 & N_3 & 0 & 0 & N_4 & 0 & 0 & N_5 & 0 & 0 & N_6 & 0 & 0 & N_7 & 0 & 0 & N_8 & 0 & 0 \\ 0 & N_1 & 0 & 0 & N_2 & 0 & 0 & N_3 & 0 & 0 & N_4 & 0 & 0 & N_5 & 0 & 0 & N_6 & 0 & 0 & N_7 & 0 & 0 & N_8 & 0 \\ 0 & 0 & N_1 & 0 & 0 & N_2 & 0 & 0 & N_3 & 0 & 0 & N_4 & 0 & 0 & N_5 & 0 & 0 & N_6 & 0 & 0 & N_7 & 0 & 0 & N_8 \end{bmatrix} \tag{3.77}$$

The $\underline{B}$ matrix for an eight noded hexahedral element is obtained by substituting (3.77) into (3.19):

$$\underline{B} = \begin{bmatrix} N_{1,x} & 0 & 0 & N_{2,x} & 0 & 0 & N_{3,x} & 0 & 0 & N_{4,x} & 0 & 0 & N_{5,x} & 0 & 0 & N_{6,x} & 0 & 0 & N_{7,x} & 0 & 0 & N_{8,x} & 0 & 0 \\ 0 & N_{1,y} & 0 & 0 & N_{2,y} & 0 & 0 & N_{3,y} & 0 & 0 & N_{4,y} & 0 & 0 & N_{5,y} & 0 & 0 & N_{6,y} & 0 & 0 & N_{7,y} & 0 & 0 & N_{8,y} & 0 \\ 0 & 0 & N_{1,z} & 0 & 0 & N_{2,z} & 0 & 0 & N_{3,z} & 0 & 0 & N_{4,z} & 0 & 0 & N_{5,z} & 0 & 0 & N_{6,z} & 0 & 0 & N_{7,z} & 0 & 0 & N_{8,z} \\ N_{1,y} & N_{1,x} & 0 & N_{2,y} & N_{2,x} & 0 & N_{3,y} & N_{3,x} & 0 & N_{4,y} & N_{4,x} & 0 & N_{5,y} & N_{5,x} & 0 & N_{6,y} & N_{6,x} & 0 & N_{7,y} & N_{7,x} & 0 & N_{8,y} & N_{8,x} & 0 \\ N_{1,z} & 0 & N_{1,x} & N_{2,z} & 0 & N_{2,x} & N_{3,z} & 0 & N_{3,x} & N_{4,z} & 0 & N_{4,x} & N_{5,z} & 0 & N_{5,x} & N_{6,z} & 0 & N_{6,x} & N_{7,z} & 0 & N_{7,x} & N_{8,z} & 0 & N_{8,x} \\ 0 & N_{1,z} & N_{1,y} & 0 & N_{2,z} & N_{2,y} & 0 & N_{3,z} & N_{3,y} & 0 & N_{4,z} & N_{4,y} & 0 & N_{5,z} & N_{5,y} & 0 & N_{6,z} & N_{6,y} & 0 & N_{7,z} & N_{7,y} & 0 & N_{8,z} & N_{8,y} \end{bmatrix} \tag{3.78}$$

where $,x$ denotes differentiation with respect to $x$. The shape functions are defined in terms of the local

coordinate system, it is necessary to employ the function of a function rule of differentiation to enable

the construction of the Jacobian transformation matrix. Hence

$$\frac{\partial N_i}{\partial \xi} = \frac{\partial N_i}{\partial x} \frac{\partial x}{\partial \xi} + \frac{\partial N_i}{\partial y} \frac{\partial y}{\partial \xi} + \frac{\partial N_i}{\partial z} \frac{\partial z}{\partial \xi} \tag{3.79}$$

$$\frac{\partial N_i}{\partial \eta} = \frac{\partial N_i}{\partial x} \frac{\partial x}{\partial \eta} + \frac{\partial N_i}{\partial y} \frac{\partial y}{\partial \eta} + \frac{\partial N_i}{\partial z} \frac{\partial z}{\partial \eta} \tag{3.80}$$

$$\frac{\partial N_i}{\partial \zeta} = \frac{\partial N_i}{\partial x} \frac{\partial x}{\partial \zeta} + \frac{\partial N_i}{\partial y} \frac{\partial y}{\partial \zeta} + \frac{\partial N_i}{\partial z} \frac{\partial z}{\partial \zeta} \tag{3.81}$$

Expressions (3.79) – (3.81) may be written in matrix form as:

$$
\begin{bmatrix}
\dfrac{\partial N_i}{\partial \xi} \\[2mm]
\dfrac{\partial N_i}{\partial \eta} \\[2mm]
\dfrac{\partial N_i}{\partial \zeta}
\end{bmatrix}
= \underline{J}
\begin{bmatrix}
\dfrac{\partial N_i}{\partial x} \\[2mm]
\dfrac{\partial N_i}{\partial y} \\[2mm]
\dfrac{\partial N_i}{\partial z}
\end{bmatrix}
\tag{3.82}
$$

where the Jacobian matrix is given by:

$$
\underline{J} =
\begin{bmatrix}
\dfrac{\partial x}{\partial \xi} & \dfrac{\partial y}{\partial \xi} & \dfrac{\partial z}{\partial \xi} \\[3mm]
\dfrac{\partial x}{\partial \eta} & \dfrac{\partial y}{\partial \eta} & \dfrac{\partial z}{\partial \eta} \\[3mm]
\dfrac{\partial x}{\partial \zeta} & \dfrac{\partial y}{\partial \zeta} & \dfrac{\partial z}{\partial \varsigma}
\end{bmatrix}
\tag{3.83}
$$

Substitution of the interpolation relations (3.74 – 3.76) into the Jacobian matrix (3.83) leads to (3.84):

$$
\underline{J} =
\begin{bmatrix}
\displaystyle\sum_{i=1}^{8} x_i \dfrac{\partial N_i}{\partial \xi} & \displaystyle\sum_{i=1}^{8} y_i \dfrac{\partial N_i}{\partial \xi} & \displaystyle\sum_{i=1}^{8} z_i \dfrac{\partial N_i}{\partial \xi} \\[4mm]
\displaystyle\sum_{i=1}^{8} x_i \dfrac{\partial N_i}{\partial \eta} & \displaystyle\sum_{i=1}^{8} y_i \dfrac{\partial N_i}{\partial \eta} & \displaystyle\sum_{i=1}^{8} z_i \dfrac{\partial N_i}{\partial \eta} \\[4mm]
\displaystyle\sum_{i=1}^{8} x_i \dfrac{\partial N_i}{\partial \zeta} & \displaystyle\sum_{i=1}^{8} y_i \dfrac{\partial N_i}{\partial \zeta} & \displaystyle\sum_{i=1}^{8} z_i \dfrac{\partial N_{i=1}}{\partial \varsigma}
\end{bmatrix}
\tag{3.84}
$$

By rewriting (3.82) in the form:

$$
\begin{bmatrix}
\dfrac{\partial N_i}{\partial x} \\[2mm]
\dfrac{\partial N_i}{\partial y} \\[2mm]
\dfrac{\partial N_i}{\partial z}
\end{bmatrix}
= \underline{J}^{-1}
\begin{bmatrix}
\dfrac{\partial N_i}{\partial \xi} \\[2mm]
\dfrac{\partial N_i}{\partial \eta} \\[2mm]
\dfrac{\partial N_i}{\partial \zeta}
\end{bmatrix}
\tag{3.85}
$$

the mass, stiffness and damping matrices are written as:

$$\underline{M} = \int_V \rho \underline{N}^T \underline{N} dV = \int_{-1}^{1}\int_{-1}^{1}\int_{-1}^{1} \rho \underline{N}^T \underline{N} \det[\underline{J}] d\xi d\eta d\zeta$$

(3.86)

$$\underline{K} = \int_V \underline{B}^T \underline{D}\underline{B} dV = \int_{-1}^{1}\int_{-1}^{1}\int_{-1}^{1} \underline{B}^T \underline{D}\underline{B} \det[\underline{J}] d\xi d\eta d\zeta$$

(3.87)

$$\underline{R} = \int_V \underline{N}^T \kappa \underline{N} dV = \int_{-1}^{1}\int_{-1}^{1}\int_{-1}^{1} \underline{N}^T \kappa \underline{N} \det[\underline{J}] d\xi d\eta d\zeta$$

(3.88)

The integrals (3.86)-(3.88) are evaluated using Gauss integration which is a method which is applied to an integral over the interval $[-1,1]$. In one dimension, the n-point Gauss integration approximates the integral $I = \int_{-1}^{1} g(x)dx$ as:

$$I = \int_{-1}^{1} g(x)dx = w_1 g(x_1) + w_2 g(x_2) \cdots + w_n g(x_n)$$

(3.89)

where the $w_i$ are referred to as 'weights' and are known for all values from 1 to n, the $x_i$ are referred to as Gauss points. For further details on the derivation of and tabulated values of the Gauss point locations and their corresponding weights, the reader is referred to (Logan 2011). By default, ABAQUS uses five Gauss points when executing numerical integration via Gaussian quadrature.

## 3.9    Continuum Shell Element SC8R

The previous section was concerned with the shape functions of an eight noded element as this is the element type used in the three dimensional simulations in this thesis. This section outlines why the continuum element SC8R which is an eight noded reduced integration (*i.e.* that the order of integration is of one order lower order than the shape functions) element and uses the shape functions described in section was selected for use in this study. Firstly, since the results of the three

dimensional dynamic analysis generated in ABAQUS/Explicit are to be read into ABAQUS/Standard (which uses the implicit solution method) for the springback analysis, it is necessary to select an element which is available in both libraries. Reduced integration elements were chosen for the three dimensional models in as they are less susceptible to exhibiting locking, hence lower order integration is used to calculate the element stiffness matrix, however, the terms in the mass matrix are still calculated by implementing full integration. Shell elements are designed for use in situations where one dimension (e.g. thickness) is significantly smaller than the other dimensions; rather than use a reference surface to discretize a body as is the case with conventional shell elements; continuum shell elements discretize an entire three dimensional body directly. Continuum shell elements are suitable for use in large strain nonlinear analyses since they allow for large rotations and deformation. Furthermore, these elements allow for two sided contact and changes in the thickness, irrespective of how thick the element is in comparison to other element dimensions. Therefore, the three dimensional eight noded hexahedral continuum shell element with reduced integration (SC8R) was selected for use in the three dimensional dynamic and springback analyses. This element was used extensively by Wang (2012) to model wrinkling in the conventional metal spinning of cylindrical parts, its selection was verified by experimentation.

The equivalent two dimensional axisymmetric element is the CAX4D element. For this element, the corresponding shape functions are given by relations (3.90)-(3.93).

$$
\begin{aligned}
N_1 &= (1-\xi)(1-\eta) \\
N_2 &= (1-\xi)\eta \\
N_3 &= \xi\eta \\
N_4 &= \xi(1-\eta)
\end{aligned}
\qquad\qquad (3.90)\text{-}(3.93)
$$

with corresponding $\underline{B}$ matrix given by (3.94).

$$\underline{B} = \begin{bmatrix} \dfrac{\partial N_1}{\partial r} & 0 & \dfrac{\partial N_2}{\partial r} & 0 & \dfrac{\partial N_3}{\partial r} & 0 & \dfrac{\partial N_4}{\partial r} & 0 \\ 0 & \dfrac{\partial N_1}{\partial z} & 0 & \dfrac{\partial N_2}{\partial z} & 0 & \dfrac{\partial N_3}{\partial z} & 0 & \dfrac{\partial N_4}{\partial z} \\ \dfrac{\partial N_1}{\partial z} & \dfrac{\partial N_1}{\partial r} & \dfrac{\partial N_2}{\partial z} & \dfrac{\partial N_2}{\partial r} & \dfrac{\partial N_3}{\partial z} & \dfrac{\partial N_3}{\partial r} & \dfrac{\partial N_4}{\partial z} & \dfrac{\partial N_4}{\partial r} \\ \dfrac{N_1}{r} & 0 & \dfrac{N_2}{r} & 0 & \dfrac{N_3}{r} & 0 & \dfrac{N_4}{r} & 0 \end{bmatrix} \qquad (3.94)$$

Now that the isoparametric details of the elements have been discussed, this chapter continues by discussing the choice of mesh used in this study.

## 3.10    Mesh Selection

An important consideration is the choice of mesh employed can also have an effect on the validity and solution time of a model. Sebastiani *et al.* (2006) investigated the suitability of various meshes for modelling the metal spinning process as shown in Figure 3.9.
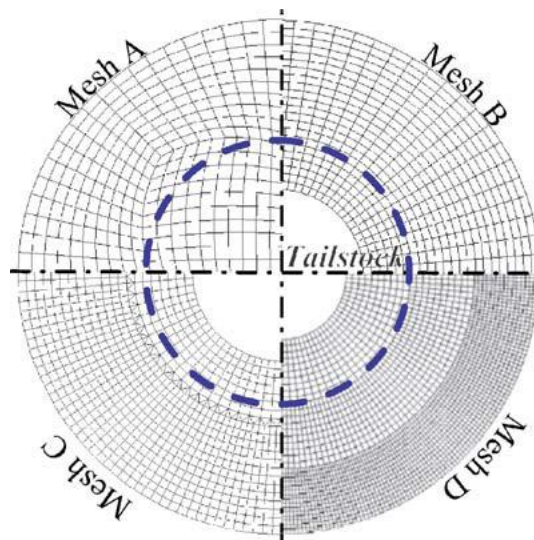


Figure 3.9: Different meshing strategies (Sebastiani *et al.* 2006)

Mesh A uses an irregular element distribution to mesh the entire blank, whereas meshes B, C and D neglect the central section of the blank which is clamped by the tailstock. Mesh B uses a regular

element distribution, Mesh C uses a row of triangular elements around the rim of the tailstock and Mesh D uses a concentric mesh.

The authors report that mesh D was the only employable mesh as mesh A resulted in "local stress peaks due to an inhomogeneous mass distribution in the rotating blank". Whilst the authors do not go into further detail on this point, it is likely that anomalies were observed since from Figure 3.9 it can be seen that the aspect ratio of some individual elements appear to violate the requirement that the aspect ratio of individual elements should not exceed 2 (ABAQUS, 2010). Violation of this condition leads to hourglassing. Mesh B was unusable because the aspect ratio of the outer elements exceeded the 2:1 ratio; this is not acceptable since they state that the aspect ratio should be as close to 1:1 as possible in order to produce more accurate results. Although mesh C gave more desirable results than either meshes A or B, an inhomogeneous mass distribution was still present in the forming zone. Again, Sebastiani *et al.* (2006) does not explore the source of this fault. The notion of optimising mesh design in spinning simulations by creating sub-domains was investigated by Quigley and Monaghan (2002a). They found that the quickest solution times were obtained for meshes which minimised both the boundary length and the number of shared boundaries, mesh C would also be considered less favourable in the light of this finding. Of Mesh D, Sebastiani *et al.* (2006) report that this mesh effectively divides the solution domain into three sub-domains and was found to be free of the aforementioned defects. Consequently, Sebastiani *et al.* (2006) selected this mesh for their study. Since the present study required the entire blank to be meshed (rather than neglecting the area under the tailstock) it was not possible to implement the mesh design of Sebastiani *et al.* (2006). The mesh selection process for the current study is presented here; for each mesh design information has been gathered about the kinetic to internal and strain energy to internal energy ratios in addition to the run time of the job. According to this information, each mesh has been allocated 'points', where 1 is the best mesh and 7 is the worst. The points have been added over the areas of interest and the mesh with the overall lowest number of points, *i.e.* the optimal mesh is selected. The selection procedure is detailed in Tables 3.1 and 3.2 and the graphs of the kinetic energy to internal energy and artificial

strain energy to internal energy are given in Figures 3.10 and 3.11. The results show that mesh 6 is the

optimal mesh.
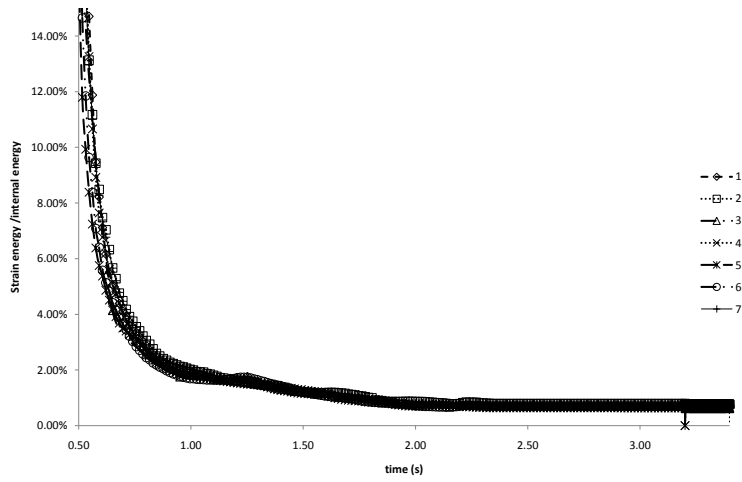


Figure 3.10: Ratio of strain energy to internal energy
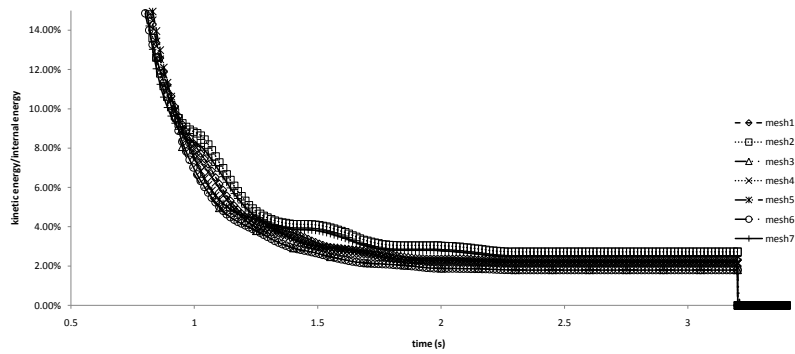


Figure 3.11: Ratio of kinetic energy to Internal energy
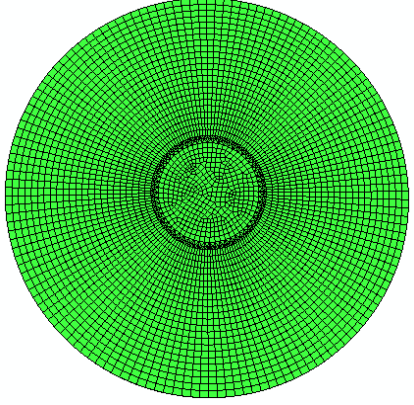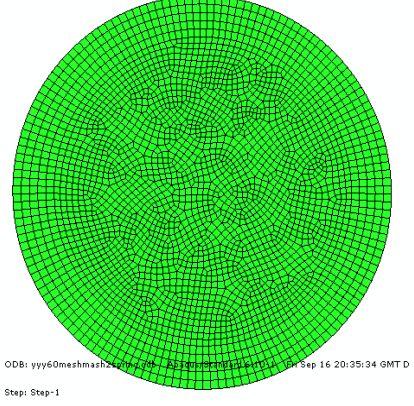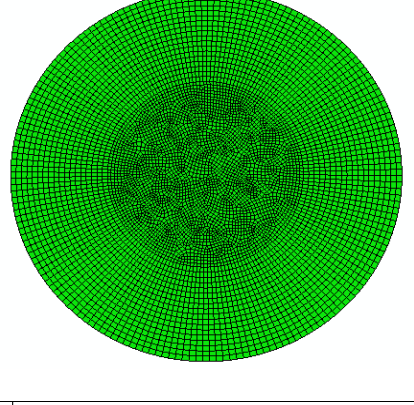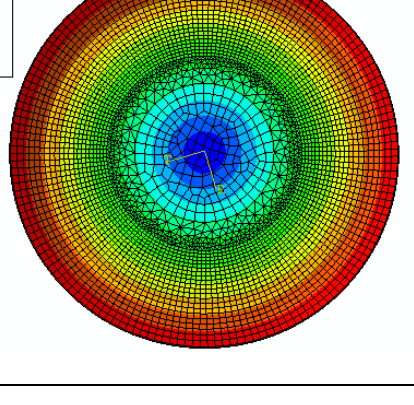
| Name | KE/IE | SE/IE | Run Time | Points | Nodes | D.O.F | Mesh |
|------|-------|-------|----------|--------|-------|-------|------|
| Mesh1 | 5 | 2 | 47 hrs (5) | 12 | 8076 | 24228 |  |
| Mesh2 | 7 | 7 | 23.5 hrs (1) | 15 | 6194 | 18582 |  |
| Mesh3 | 2 | 5 | 68.5 (6) | 13 | 13112 | 39336 |  |
| Mesh4 | 3 | 1 | 44hrs 55 (4) | 8 | 8288 | 24864 |  |

Table 3.1: Mesh selection process
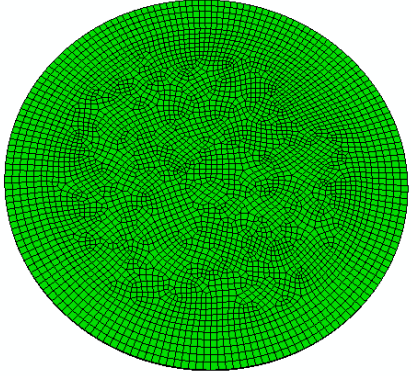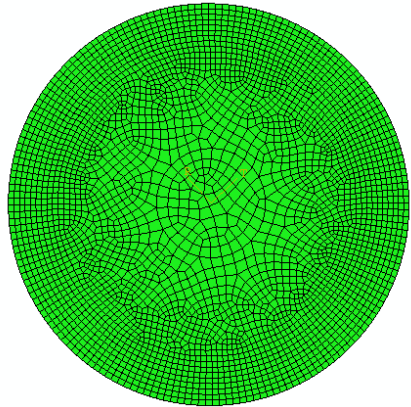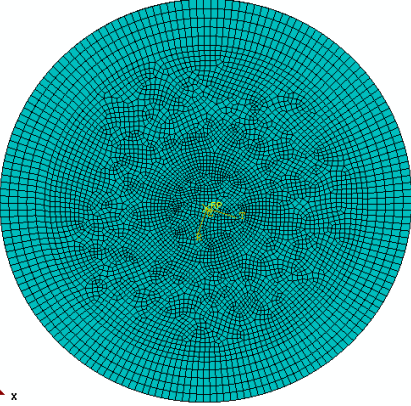
| Name | KE/EI | SE/IE | Run Time | Points | Nodes | D.O.F | Mesh |
|------|-------|-------|----------|--------|-------|-------|------|
| Mesh5 | 4 | 3 | 37hrs 40 (3) | 10 | 8392 | 25176 |  |
| Mesh6 | 1 | 4 | 26hrs 11 (2) | 7 | 6884 | 20652 |  |
| Mesh7 | 6 | 6 | c 93 hrs (7) | 19 | 10842 | 32526 |  |

Table 3.2: Mesh selection process

In this section the governing equations for the finite element method were derived and the isoparametric formulation of the elements used in this thesis was also presented. The solution methods used to solve these equations alongside potential sources of error such as hourglassing and locking were presented. Furthermore; the choice of mesh used in the current study was also justified. The thesis progresses by developing the three-dimensional model.

# §4    Three Dimensional Modelling

This chapter details the development of a single pass, three-dimensional numerical model for the conventional metal spinning of cones using the mild steel material definition using Ludwick's law which was presented in the previous chapter. The Ludwick law was chosen since it includes work hardening, provides an explicit relation for stress as a function of strain and is readily adapted for mild steel or aluminium. The chapter also includes details as to the selection of the roller clearance in the absence of experimental data. Model validation is proposed by comparison with Wang (2012) and by comparison with experimental data published by Kobayashi (1963). Following this, a formability parameter connecting the rotational speed, half cone angle, radius and round off radius of the mandrel with the blank radius is proposed for the single pass conventional metal spinning of conical parts from mild steel. The second half of the chapter presents a theoretical expression for the hoop force in the conventional metal spinning process. The variation of this theoretical hoop force with respect to the formability parameter proposed in the first half of the chapter is investigated. In addition, the variation of process parameters such as the mandrel half cone angle and mandrel rotational speed is investigated.

## 4.1    Development of the Three Dimensional Model

As was mentioned in the methodology, the commercial software package, ABAQUS, was used to simulate this process. It is at this stage that the first of the modelling assumptions is implemented; namely that any elastic behaviour occurring in the roller, mandrel and tailstock is taken to be negligible. Therefore, the aforementioned parts are all modelled as analytical rigid bodies, each with its own reference point which is used to control the part. The blank is modelled as a solid disc which is meshed with SC8R continuum shell elements (discussed in the previous chapter). The model simulates the forming of a frustum of mild steel using a single pass conventional metal spinning process for cone angles of $60^{\circ}$, $50^{\circ}$, $40^{\circ}$ and $30^{\circ}$. The initial configuration of the model is shown in Figure 4.1.
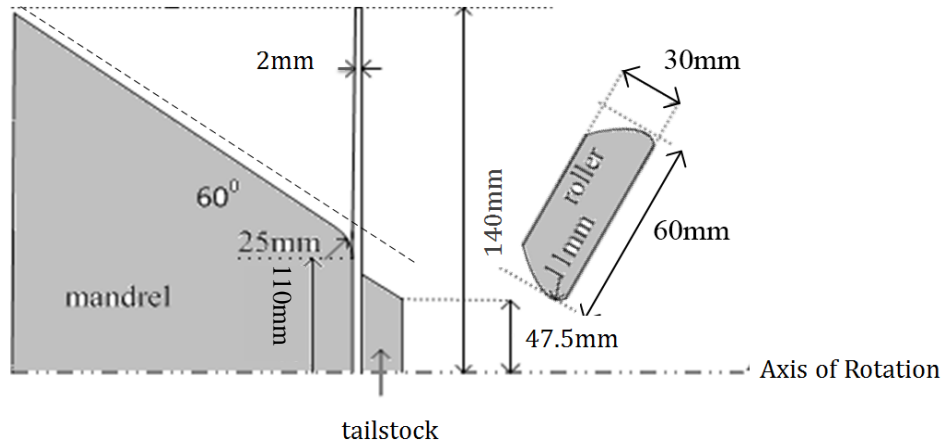
Figure 4.1: Initial setup of the process

The roller forms the part by tracing a single pass parallel to the straight surface of the mandrel. The clearance is defined as the distance between the surface of the mandrel and the dotted line which lies tangential to the roller and parallel to the mandrel surface as illustrated in Figure 4.1. Whilst conventional metal spinning aims to maintain the blank thickness, in practice the clearances used to form parts in this way are less than the blank thickness (Xia *et al*. 2005).  Although, it is accepted that for the geometry shown in Figure 4.1, there are two forms of metal spinning, namely shear and conventional metal spinning, no clear method of partitioning the two forms has been presented (Music *et al* (2010), Wang *et al*. (2010). The only quantitative guideline as to whether a process is categorized as either shear or conventional spinning is given by the 'sine law' (Wong *et al*. (2003)) (as reviewed in Chapter 2). Table 4.1 provides the calculations of the final wall thickness using this rule.

| Cone angle | Ideal thickness (mm) to 3 s.f. |
|:----------:|:------------------------------:|
| 30 | 1.00 |
| 40 | 1.29 |
| 50 | 1.53 |
| 60 | 1.73 |

Table 4.1: Thicknesses calculated using the sine law

The thicknesses in Table 4.1 represent thicknesses predicted by the sine law for the shear spinning process and therefore may be considered as a lower limit on the clearance for the simulations which implies that the range of conventional metal spinning lies in the range 1.73mm< c < 2mm for a cone of half angle $60^0$. In order to establish a limit between the two forms of spinning, the forming process was carried out on a $60^0$ cone using clearances of 1.7mm, 1.8mm, 1.9mm and 2.0mm. This range was chosen in order to capture the transition between shear spinning (as shown in Table 4.1) and conventional spinning for a $60^0$ cone. Figure 4.2 shows the force history obtained from the roller for these clearances; it can be seen that using a clearance of 2mm (equal to the blank thickness) results in troughs in the history output and an overall reduction in the force suggesting that the blank forms in a way which involves a periodic reduction in contact between the roller and the blank. Conversely, in the range of shear metal spinning (clearance 1.7mm), these troughs disappear and the forming force required is much higher. This is consistent with the additional deformation associated with a reduction in thickness. The presence of troughs in the output from the simulation run with a clearance of 1.9mm suggests that 1.9mm is also an inappropriate value for the clearance, whereas the results for a clearance of 1.8mm indicate that this is an appropriate clearance since it is both outside the range of the shear forming limits as predicted by the 'sine law' and has a force history free from the troughs observed in the simulations for 1.9mm and 2.0mm clearances. Consequently, a clearance of 1.8mm was selected for the current study since it lies outside the range of shear spinning for all the cone angles tested in this study.
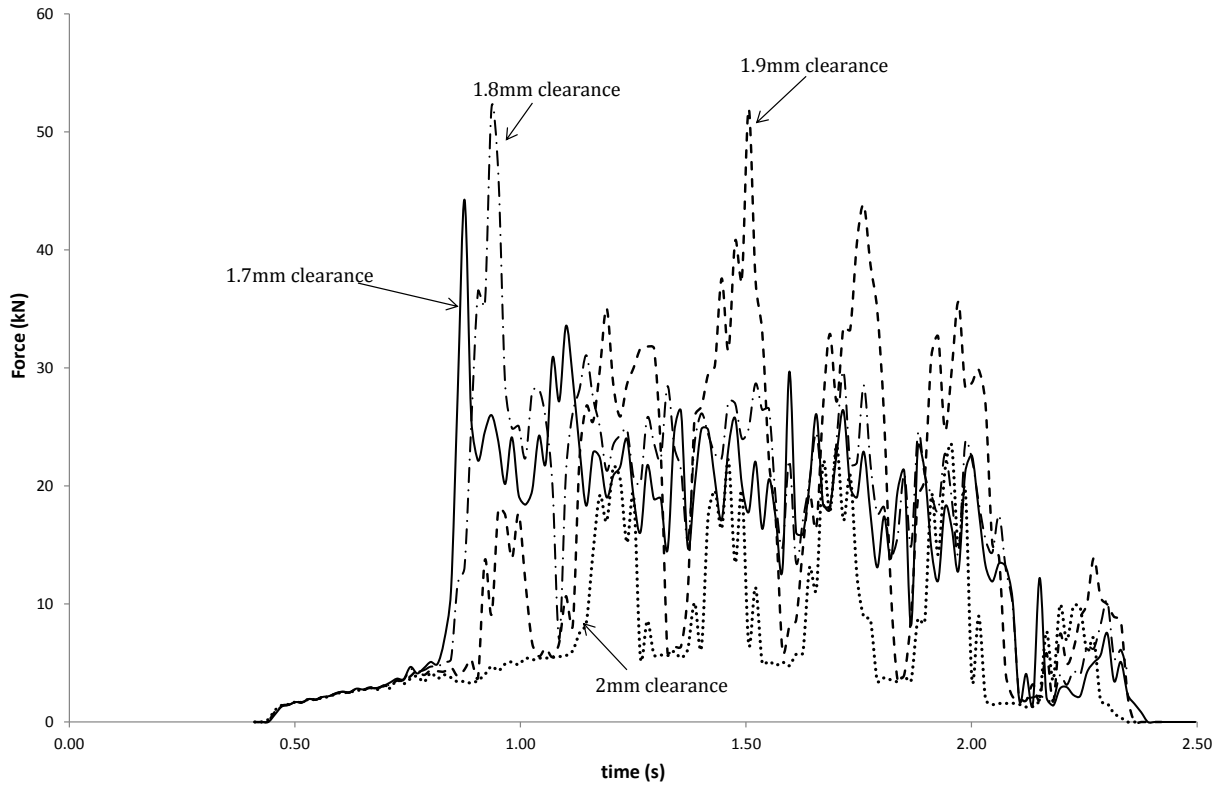
Figure 4.2: Circumferential Force history for different clearances

The model consists of four analysis steps carried out using ABAQUS/Explicit; the details of each step are given below, followed by a table of boundary conditions and a table of interactions.

Initial Step

This step is an inherent part of the software and as such is present in all models, there is no time associated with this step and so only actions to fix locations and interaction properties may be implemented in this step; this step is not classified as an analysis step. In the current model, the initial step is used to constrain all six degrees of freedom of the tailstock and the mandrel. In addition, the frictional conditions between the blank and mandrel, blank and tailstock and blank and roller are applied in this step. The coefficient of friction was set to 0.2 between the blank and the mandrel, to 0.02 between the

blank and the roller and 0.5 between the tailstock and the blank. These values were chosen as they are the values used by Wang *et al*. (2011) in his model of the conventional metal spinning process, his values were successfully verified against experiments (Wang *et al*., 2011).

### Step 1: Apply Tailstock Force, duration 0.001(s)

As the name of this step suggests, this step is used to apply a force at the tailstock reference point towards the mandrel in order to clamp the blank between the mandrel and the tailstock. This force is propagated throughout the whole simulation.

### Step 2: Rotate Parts, duration 0.2(s)

During this step, the boundary conditions applied to the tailstock and mandrel in the initial step are modified so that the two parts rotate with the same angular velocity. The parts are gradually brought from rest to a specified angular velocity. Whilst there is no rotation condition applied directly to the blank, the blank also rotates in this step owing to the frictional conditions applied between it and the mandrel and the tailstock in addition to the 'clamping' force applied to the tailstock.

### Step 3: Form, duration 3(s)

During this step, the blank is forced onto the mandrel by the roller which traces a single linear pass of the mandrel. Whilst in practice the conventional metal spinning process is most often a multi-pass process, it is possible to carry out the conventional metal spinning process using a single pass (Music *et al*., 2010). This study simulates a single pass process using a linear path in order to enable additional verification of the model against experimental data for the forming of cones, published by Kobayashi (1963).

 Step 4: Return, duration 0.2(s)

This is a relatively short step in which the mandrel is brought back to rest in a step which mirrors the step 'rotate parts'. Table 4.2 details the boundary conditions used in the model.

| Boundary Condition | Initial | Apply force | Rotate parts | Form | Return |
|---|---|---|---|---|---|
| Fix mandrel | u1=u2=u3=0 | propagated | inactive | inactive | inactive |
| Fix tailstock | u1=u2=u3=0 | u1=u2=0 | inactive | inactive | inactive |
| Rotate mandrel | | | V1=v2=v3=0 vR1=vR3=0 vR2 =mandrel velocity (rad/s) | propagated | v1=v2=v3=0 vR1=vR2=vR3=0 |
| Rotate tailstock | | | V1=v2=v3=0 vR1=vR3=0 vR2 =mandrel velocity (rad/s) | propagated | v1=v2=v3=0 vR1=vR2=vR3=0 |
| Roll | v1=v2=v3=0 vR1=vR2=vR3=0 | propagated | propagated | v1=v2=0 vR1=vR2=0 v3=0.015ms$^{-1}$ | propagated |

Table 4.2: Boundary conditions used in the model

The boundary conditions on the roller are applied to a local cylindrical coordinate system which is active on the roller. In this system, the local '3' direction lies parallel to the roller path as illustrated in Figure 4.1 , direction '2' is in the circumferential direction and '1' is the radial direction; 'u' represents displacement degrees of freedom whilst 'v' represents velocity degrees of freedom.

**VALIDATION OF THE MODEL**.

Since it was not possible to perform experimental studies throughout this research project, a different approach was needed in order to validate the model. It has already been mentioned that Wang (2012) successfully verified their finite element model against experimental evidence and that this was the reasoning behind the choice of coefficient of friction between the mandrel and the blank, the blank and the tailstock and the roller and the blank. Furthermore, the roller geometry was also chosen to match that of Wang (2012) for the same reason.

The next stage of the verification process was to verify the mesh. In their study, for the area of the mesh that would undergo contact with the roller, Wang (2012) used a (regular) mesh composed of SC8R elements with one element through the thickness of the blank, to simulate the conventional metal spinning process with multiple passes. This mesh neglected the area of the blank under the tailstock; their approach was validated by comparison with experimental results. Since the current study uses the same elements to also model the conventional metal spinning process and uses a mesh of similar aspect ratio to the optimal density discussed by Wang (2012), it is logical to conclude that the mesh in the current study would also be validated. Additionally, the mesh used in this study was directly verified against the analytical solution for the stresses generated in a thin spinning disc. Figures 4.3 and 4.4 show the results for the radial and hoop stresses generated from spinning the blank at 600rpm; comparisons with the theoretical expressions for stresses generated in a spinning disc are shown in Figure 4.5. Since the stresses generated in the model match the theoretical stresses and Table 3.1(b) shows that the ratios of kinetic energy to internal energy and artificial strain energy are well within the recommended limits. Therefore the mesh may be considered to be verified.
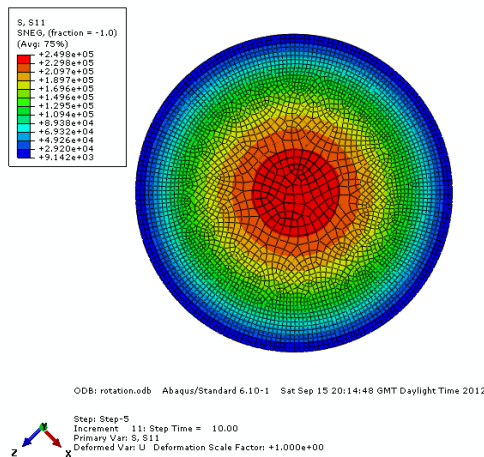


Figure 4.3: Radial stress in a spinning disc
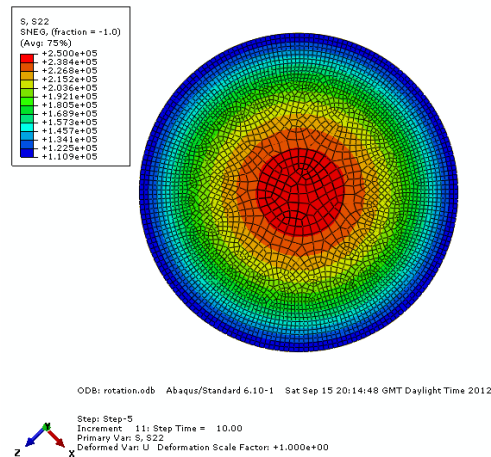
Figure 4.4: Hoop stress in a spinning disc
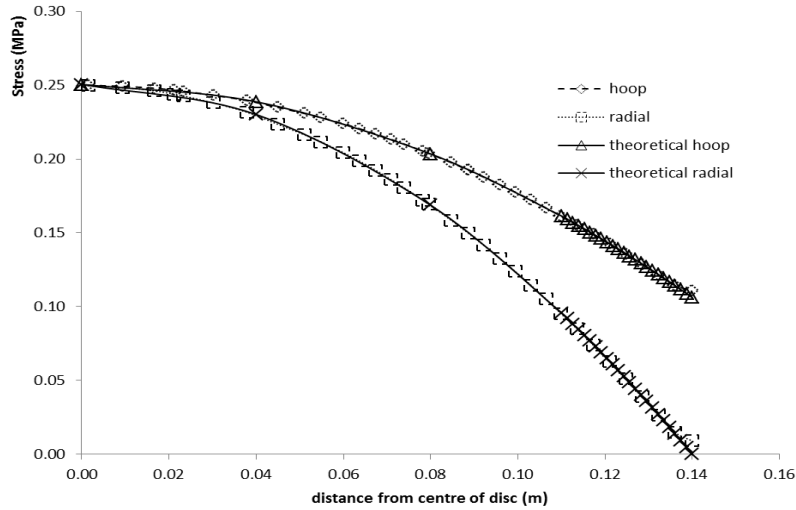
Figure 4.5: Comparison of theoretical and outputted stresses

The final stage of verification is to verify the model as a whole; this is done by comparison with the experimental work carried out by Kobayashi (1963), who proposed a formability limit in terms of the ratio of the blank and mandrel radii and cosec α, where α is the half cone angle of the mandrel as illustrated in Figure 4.1. This limit is reproduced in Figure 4.6. Kobayashi (1963) conducted experiments using 1.25mm thick aluminium, a mandrel of half cone angle $35^0$, rotational speed of 40 rpm and a roller velocity of 0.111ins/rev. The experiments were carried out using blanks of diameter, 2.75 inches, 3 inches, 3.5 inches and 4.5 inches and it was also implied that the parts are formed using a single pass.
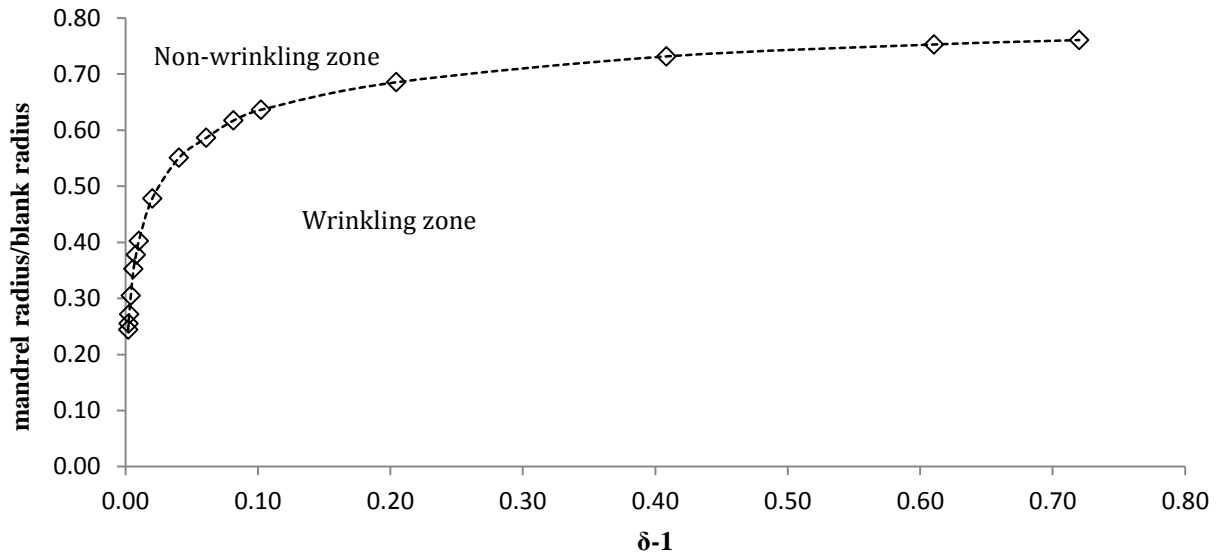
Figure 4.6: Kobayashi's formability limit (1963)

In Figure 4.6, the quantity $\delta$ may be viewed as a ratio of the final part thickness to the thickness predicted by the sine law and is defined in terms of the initial blank thickness, $t_0$; the final part thickness, $t_f$ and the half cone angle of the mandrel, $\alpha$, as:

$$\delta = \frac{t_f}{t_0 \sin \alpha} \tag{4.1}$$

For a blank radius of 140mm and a mandrel radius of 110mm, Kobayashi's (1963) limit predicts that a part could be formed on a mandrel with a half cone angle of $35^0$, although a part formed on a 30 degree cone would wrinkle. In order to verify the current model, two simulations were performed using the three-dimensional model developed for aluminium of thickness 1.25mm. As Kobayashi (1963) conducted his experiments using aluminium; the stated value of Young's modulus was taken to be 70GPa and the Poisson's ratio as 0.35. Furthermore, the Ludwick Law, described in equation (3.65), was used to define the material model for Aluminium, with hardening exponent of 0.17, strength coefficient of 780MPa and a yield stress of 10MPa; the density of the Aluminium was taken to be 2700kgm$^{-3}$ (Gope, 2012).

The 35 degree part formed without wrinkles, whereas the 30 degree part wrinkled early in the process as shown in Figures 4.7 and 4.8. Therefore the three dimensional model has been validated against experimental data presented by Kobayashi (1963).
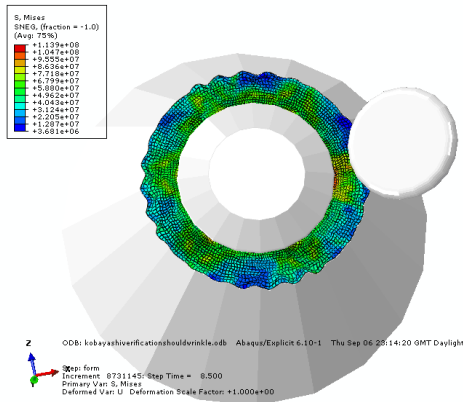


Figure 4.7: 30 degree cone wrinkling
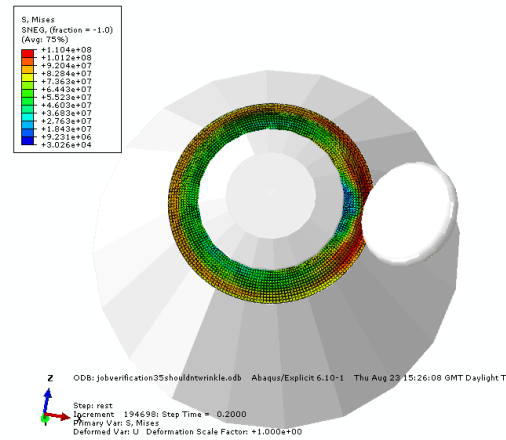
Figure 4.8: 35 degree cone forming without wrinkles

However, Kobayashi's (1963) relation implies that if a blank of radius $r_b$ formed on a mandrel of radius $r_c$ wrinkles, a blank of radius $pr_b$, (where $p$ is any (positive) real number) formed on a mandrel of radius $pr_c$ will also wrinkle. In order to test this, $p$ was selected to be 0.8. Recall that for the configurations shown in Figures 4.7 and 4.8, the blank radius used was 140mm and the mandrel radius used was 110mm. Using a blank radius of 112mm and a mandrel radius of 88mm (the values obtained by choosing $p$=0.8), thereby preserving Kobayashi's (1963) ratio, and re-running the forming process for a 35 degree cone, the part was found to wrinkle, contrary to Kobayashi's (1963) prediction. This suggests that a subtle adjustment to Kobayashi's (1963) ratio is required. The following section proposes the introduction of a formability parameter to account for this discrepancy in Kobayashi's (1963) formability limit.

## 4.2    Proposal of Formability parameter, D.

The previous section demonstrated that preserving Kobayashi's (1963) ratio is not sufficient to guarantee that a part will form without wrinkling, although the ratios of the mandrel and blank radii were preserved the respective volumes are not. Therefore, the deformable volume may be a key parameter in determining a formability limit. Given an initial configuration of blank radius $r_b$ and mandrel radius $r_c$, the initial flange  has a length of $r_b$-$r_c$ (hereafter referred to as the 'deformable radius'). Preserving the ratio of $r_c/_{rb}$ and considering a second configuration using a blank radius of $pr_b$ and a mandrel radius of $pr_c$, it is readily seen that the deformable radius becomes

$$pr_b\text{-}pr_c\text{=}p(r_b\text{-}r_c) \tag{4.2}$$

As the deformable radius, $D$, changes, the volume being deformed during the process also changes, which implies that different stresses would be generated in each part. This highlights the fact that the choice of geometry is non-trivial. Two cases with identical deformable radii are illustrated in Figures 4.9 and 4.10.
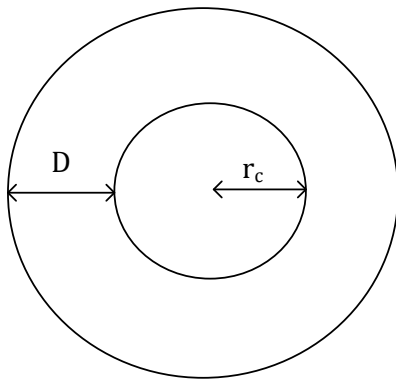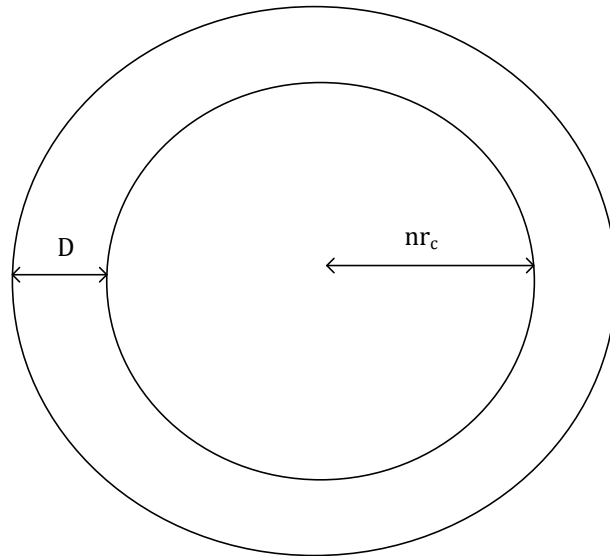


Figure 4.9: Case 1                    Figure 4.10: Case 2

It is instructive to rewrite the blank radius in terms of the deformable radius and the mandrel radius; consequently, for case 1

$$r_b = r_c + D \tag{4.3}$$

Assuming that the blank has initial thickness, $t$, then the volume of material to be deformed is written as

$$V_1 = \pi t \left\{ (r_c + D)^2 - r_c^2 \right\} \tag{4.4}$$

For case 2; let us assume that the mandrel radius is written as $nr_c$, where $n$ is a real number greater than 1, in which case, the volume of material to be deformed may be written as:

$$V_2 = \pi t \left\{ (nr_c + D)^2 - n^2 r_c^2 \right\} \tag{4.5}$$

Calculating the ratio of the volumes involved in case 1 and case 2 yields the following result

$$\frac{V_2}{V_1} = 1 + \frac{2(n-1)r_c}{2r_c + D} \tag{4.6}$$

proving that the deformable volume in case 2 is larger than case 1.

### 4.2.1   Implications for the circumferential stress

This section aims to establish a theoretical reasoning as to why the forming limit determined by Kobayashi (1963) cannot simply be applied in terms of a ratio of the blank radius and the mandrel radius. Since buckling is believed to be initiated by changes in the circumferential stress (Sebastiani *et al*. 2007), this section proceeds by focusing on the circumferential stress in the two cases. It is necessary to calculate the circumferences in the two cases

$$C_1 = 2\pi(r_c + D) \tag{4.7}$$

$$C_2 = 2\pi(nr_c + D) \tag{4.8}$$

Hence, the area of material on the circumference in each case is given by

$$A_1 = 2\pi t(r_c + D) \tag{4.9}$$

$$A_2 = 2\pi t(nr_c + D) \tag{4.10}$$

To date, proposed theoretical expressions for the circumferential force do not take both the mandrel radius and the blank radius into account, however Hayama *et al.* (1965) noted that increasing the blank radius (up to a maximum of 100mm) increases the circumferential force. Combining expressions (4.9) and (4.10) with the observations of Hayama *et al.* (1965), leads to the conclusion that when the deformable radius D is obtained with a larger mandrel radius, the stress at the circumference is lower than when the deformable radius is obtained with a smaller mandrel radius. This would indicate that increasing the mandrel radius decreases the likelihood of a part to wrinkle.

In order to examine this phenomenon in terms of Kobayashi's (1963) forming parameter, δ, it is necessary to write the ratio of mandrel radius to blank radius in terms of the deformable radius and the mandrel radius, thereby establishing for which case δ has the greater value. Defining $a_0$ as the mandrel radius and $b_0$ as the blank radius, for case 1 (Figure 4.9), this ratio may be written as

$$\frac{a_o}{b_o} = \frac{r_{mandrel}}{r_{blank}} = \frac{r_c}{r_c + D} \tag{4.11}$$

and for case 2 (Figure 4.10), the ratio is

$$\frac{a_o}{b_o} = \frac{r_{mandrel}}{r_{blank}} = \frac{nr_c}{nr_c + D} = \frac{r_c}{nr_c + D} + \frac{(n-1)r_c}{nr_c + D} \tag{4.12}$$

In order to place (4.11) and (4.12) into context of Kobayashi's (1963) forming parameter, δ, it is necessary to determine which term (either 4.11 or 4.12) has the greater value.

Comparing the first term on the right hand side of (4.12) with the term on the right hand side of (4.11) it is noted that since n>1,

$$\frac{r_c}{nr_c + D} < \frac{r_c}{r_c + D} \tag{4.13}$$

Attention is now concentrated on the second term on the right hand side of (4.12). In order to make this term easier to interpret, some algebraic manipulation of (4.11) is required. This begins by calculating the difference between the terms in relation (4.13).

$$\begin{aligned}\frac{r_c}{r_c + D} - \frac{r_c}{nr_c + D} &= \frac{r_c(nr_c + D) - r_c(r_c + D)}{(nr_c + D)(r_c + D)}\\ &= \frac{r_c^2(n-1)}{(nr_c + D)(r_c + D)}\end{aligned} \tag{4.14}$$

Therefore, through rearrangement of equation (4.14), it is possible to write:

$$\frac{r_c}{nr_c + D} = \frac{r_c}{r_c + D} - \frac{r_c^2(n-1)}{(nr_c + D)(r_c + D)} \tag{4.15}$$

Hence, it is possible to rewrite (4.11) as

$$\frac{a_o}{b_o} = \frac{r_{mandrel}}{r_{blank}} = \frac{r_c}{r_c + D} = \frac{r_c}{nr_c + D} + \frac{r_c^2(n-1)}{(nr_c + D)(r_c + D)} \tag{4.16}$$

Determining for which case Kobayashi's (1963) parameter has the greater value is reduced to a comparison of the second terms on the right hand side of equations (4.12) and (4.16). Writing

$$\frac{r_c^2(n-1)}{(nr_c+D)(r_c+D)} = \left\{\frac{r_c(n-1)}{(nr_c+D)}\right\} \times \left(\frac{r_c}{r_c+D}\right) \tag{4.17}$$

it is clear that

$$\frac{r_c^2(n-1)}{(nr_c+D)(r_c+D)} < \frac{r_c(n-1)}{(nr_c+D)} \tag{4.18}$$

Therefore, since the ratio of mandrel ratio to blank ratio is larger for case 2 than case 1, it may be seen from inspection of Figure 4.6 that this also implies that Kobayashi's (1963) ratio is larger for case 2 (larger blank radius) than for case1 which may be quantified by stating that for a given deformable radius, $D$, Kobayashi's (1963) ratio increases as the mandrel radius is increased and consequently, the chance of the part wrinkling is reduced. Recently, Zhang *et al*. (2012) presented a paper in which a quarter sized (scaled) model was used to simulate the metal spinning process. They compared the results of this model for 'spinning force' and thickness for the forming process. The results showed discrepancies between the two models with the peak value of the forming force for the 'real' model reported to be around $3.0 \times 10^6$N, twenty times bigger than the similarity model (reporting a peak value of around $1.5 \times 10^5$N), rather than the value anticipated by applying a scaling factor of 4 to the force output (Zhang *et al*. 2012). The results for the thickness distribution were also inconsistent with the assumption that a model can be scaled. This evidence appears to support the notion of $D$ as a formability parameter. It is possible to transform Kobayashi's data into the graph shown in Figure 4.11 by assuming that the blank radius may be written as the sum of the mandrel radius and the deformable radius. As Kobayashi (1963) conducted his experiments using aluminium; the information illustrated in Figure 4.11 can only be used as a guide for the spinning process using aluminium. In the next section, an empirical equation for formability (using aluminium) is proposed.
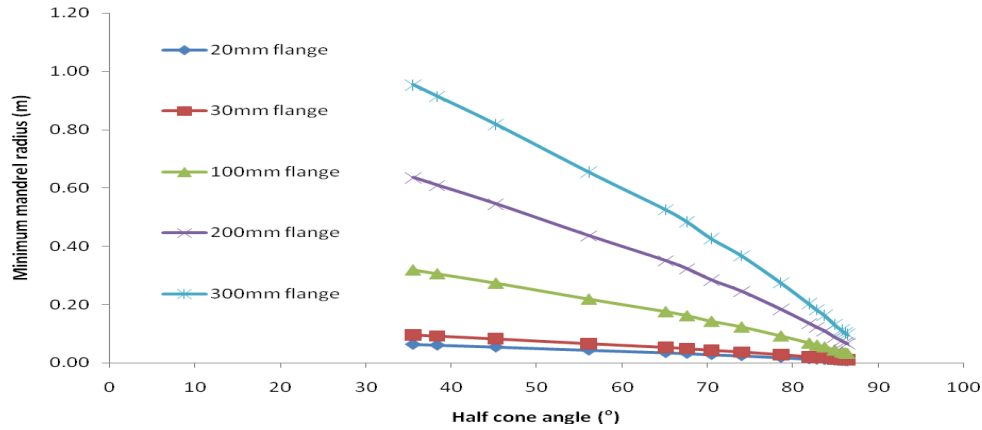
Figure 4.11: Transformation of Kobayashi's data for conventional spinning

### 4.2.2 An Equation for Formability

Using the graph generated by transcribing Kobayashi's original data as described in the previous section, it is possible to postulate an equation of formability by using the Buckingham Pi method (Langhaar (1951)). It was assumed that the formability of a part depends upon material properties such as the yield stress, density, Young's Modulus and Poisson's ratio of the material; size of the flange which is characterised by the deformable radius, the half cone angle and rotational speed of the mandrel. The formability of the part is also known to depend upon the thickness of the blank, (Kleiner (2002)) and this is also taken into account. Hence it is possible to say that an expression to describe the formability limit of a part may be written as

$$r_m = g(E, \nu, D, \alpha, t, \sigma_Y, \rho, \omega) \tag{4.19}$$

where $\omega$ is the rotational velocity of the mandrel (rpm) which needs to be converted to revolutions per second in order to maintain dimensional consistency of the final expression. The Buckingham Pi method states that the number of dimensionless independent parameters (known as Pi groups) which can be formed from the parameters stated in (4.19) is equal to the number of variables minus the number of SI units. In this case, the number of variables is nine and the number of base units is three, consequently, six groups may be formed from these variables. The Buckingham Pi method (Langhaar (1951)) states that if

one of the existing variables is already dimensionless, then it must form one of the Pi groups on its own; furthermore, no one group may be a multiple of another. Consequently, it is possible to define the six Pi groups as

$$\pi_1 = \upsilon \tag{4.20}$$

$$\pi_2 = \alpha \tag{4.21}$$

$$\pi_3 = \frac{\rho \omega^2 t^2}{E} \tag{4.22}$$

$$\pi_4 = \frac{r_m}{D} \tag{4.23}$$

$$\pi_5 = \frac{\sigma_Y}{E} \tag{4.24}$$

$$\pi_6 = \frac{\sigma_Y D^2 \omega^2}{\rho} \tag{4.25}$$

Therefore, (4.19) may be written in terms of the Pi groups as

$$\frac{r_m}{D} = \overline{g}\left( \upsilon, \alpha, \frac{\rho \omega^2 t^2}{E}, \frac{\sigma_Y}{E}, \frac{\sigma_Y D^2 \omega^2}{\rho} \right) \tag{4.26}$$

Since Kobayashi (1963) only performed experiments on aluminium, it is not possible to ascertain the influence of the material parameters on the data presented in Figure 4.11. Therefore, these material parameters are treated as constants in deriving the equation of formability. Consequently the pi groups involving the half cone angle and the deformable radius become the focus for determining the (empirical) equation of formability. Inspection of the transformed data shown in Figure 4.11 implies that as D increases, the minimum mandrel radius needed to form the part also increases, although by how much is

dependent upon the half cone angle of the part being formed. In forming the empirical equation, similarities between the curves shown in Figure 4.11 and the curve defined by

$$\frac{r_m}{D} = \ln\left(|\alpha - 90|\right) \tag{4.27}$$

indicated that (4.27) would form a part of the empirical relation. However, the gradient of (4.27) proved to be too steep when compared with the data extracted from Kobayashi's (1963) data. It was found that dividing function (4.27) by $\left(\dfrac{\alpha}{90}\right)^{1/2}$ provided a better trend when compared to Kobayashi's (1963) data.

Thereafter, a process of trial and error incorporating the remaining pi groups into relation (4.27) established relation (4.28).

$$r_m = D\left(-\ln\left(\frac{1}{|\alpha - 90|}\right)(v - 0.05)^2\frac{E}{\rho\omega^2t^2} - \frac{\sigma_Y}{\rho\omega^2D^2}\right)\left(\frac{90}{\alpha}\right)^{1/2}\left(\frac{\sigma_Y}{E}\right)A - 0.9D \tag{4.28}$$

where $A = 5\times10^{-7}$

Figure 4.12 shows (4.28) plotted for a variety of deformable radii alongside Kobayashi's (1963) transformed data. The close agreement between (4.28) and the transformed data shows that the deformable radius is a key parameter in determining the formability of a blank. In order to ascertain the statistical significance of this expression, a Chi squared test was carried out; the results of which are displayed in Table 4.3.
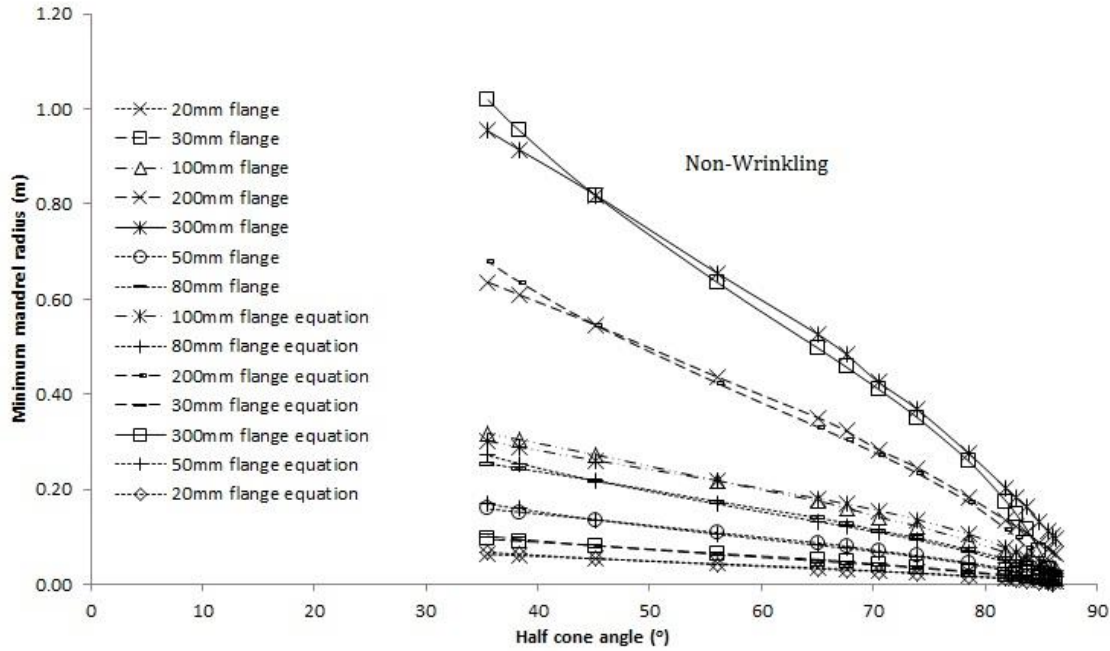
Figure 4.12: Kobayashi's (1963) formability limit transformed

The values shown in Table 4.3, combined with inspection of Figure 4.12 demonstrate a good fit of equation (4.28) to the data extracted from Kobayashi's (1963) relation for the range investigated, with the better fit being obtained for smaller deformable radii.

| Flange length (mm) | Root Mean Square Error |
|---|---|
| 300 | 0.0504 |
| 200 | 0.0336 |
| 100 | 0.0121 |
| 80 | 0.0134 |
| 50 | 0.00841 |
| 30 | 0.00504 |
| 20 | 0.00336 |

Table 4.3: Root Mean Square Error calculations (to 3 s.f.) for the data shown in Figure 4.12

This section has demonstrated that the new forming parameter, $D$, the deformable radius has a significant influence on the formability of a part. It is also apparent from the literature review and the current work that it is an oversimplification to try and determine a formability limit in terms of only two parameters.

Therefore, the next section proposes a formability surface and empirical relation for this formability surface.

## 4.3    A Formability Surface for Conventional Spinning of Cones

In order to establish patterns in relation to the formability of a part, more than 60 simulations were run using the three-dimensional model developed in this chapter. The parameters chosen to establish the formability surface were the round-off radius of the mandrel, the rotational velocity of the mandrel and the half cone angle of the mandrel. These parameters were chosen since they could be tested without altering the solution time of the model. The simulations used blanks made of mild steel with the material description given in the previous chapter. The thickness of each blank was 2mm and the radius of each blank was 140mm. Once the simulations had run and been classified as either wrinkled or not wrinkled, the results were plotted in three dimensional space using gnuplot and an empirical relation linking the test variables was formed. Figures 4.13 and 4.14 show the results of this study and the proposed empirical relation which transpired to be

$$\omega = 65000 \left( \frac{1}{2\rho_M^2} + \frac{15}{2\alpha^2} \right) - 300 \tag{4.29}$$

where $\omega$ is the mandrel rotational speed (rpm), $\rho_M$ is the mandrel round off radius (mm) and $\alpha$ is the half cone angle of the mandrel (degrees).
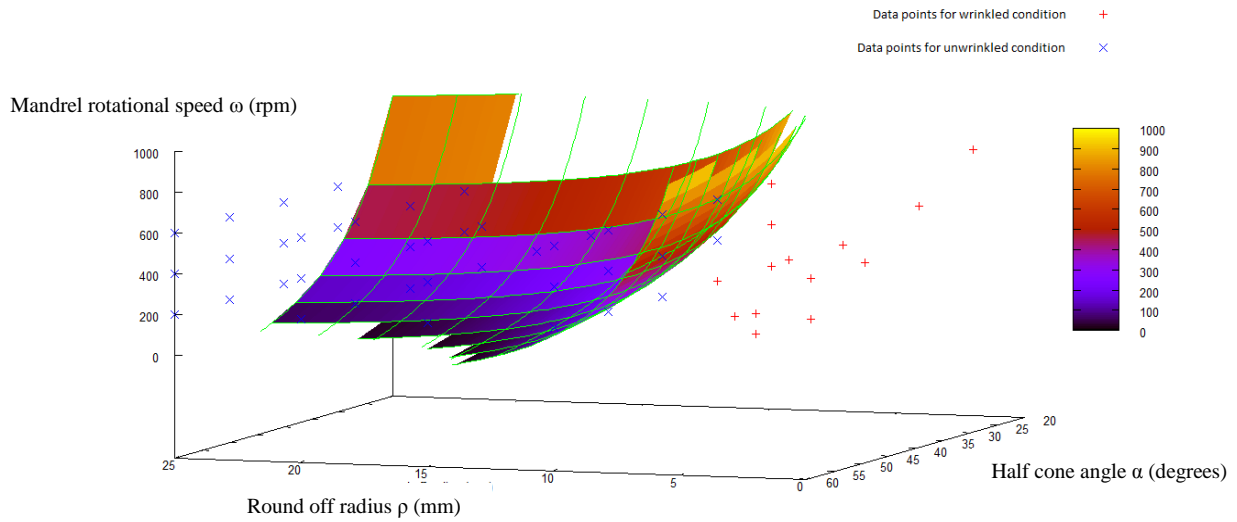
Figure 4.13: Formability surface
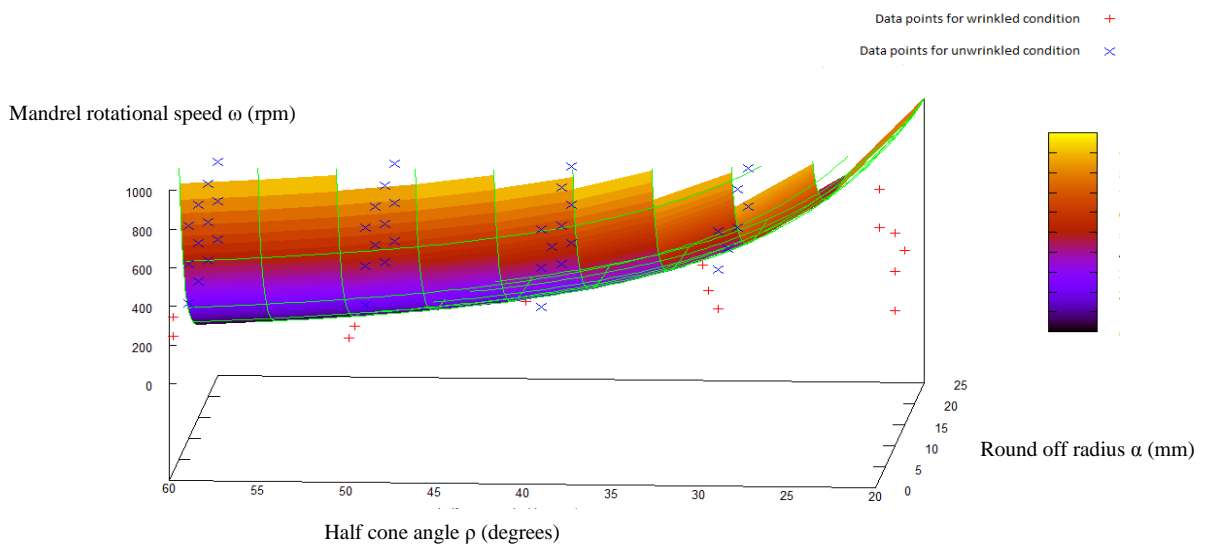


Figure 4.14: Formability surface

The empirical relation (4.29), which is only intended as a guide, was obtained by examining the results

for the formability of the smallest round off radius tested, then similarly, examining the results for the

formability for the smallest half cone angle tested. These examinations demonstrated that in both cases

the trend of an inverse square relationship appeared to be evident. Thereafter, a surface was constructed to

capture this behaviour and was modified to incorporate the data points obtained through the analyses carried out in ABAQUS.

The surface described by (4.29) and plotted in Figures 4.13 and 4.14 demonstrates a non-linear relationship linking the formability of the part and the variables investigated. In agreement with Kobayashi's (1963) experimental work; the surface shows that the likelihood of a part to form without wrinkling decreases with the half cone angle of the part being formed. In addition, the formability of the part with respect to mandrel rotational speed has also been demonstrated (Hayama *et al*. 1966). The surface also shows that the previously un-investigated parameter (round off radius) does influence the formability of the part and that a part formed using a larger round off radius is more likely to form without wrinkling than an equivalent part formed with a smaller round off radius. The effect of altering the round off radius on the deformable radius is illustrated in Figure 4.15. By considering the blank radius as the sum of the mandrel radius, deformable radius and round off radius and noting that the simulations carried out for this chapter were perfomed using a constant value for the mandrel and blank radii; it is seen that the formability of the part is sensitive to the deformable radius. Indeed, decreasing the deformable radius increases the chance that the part will form without wrinkling.
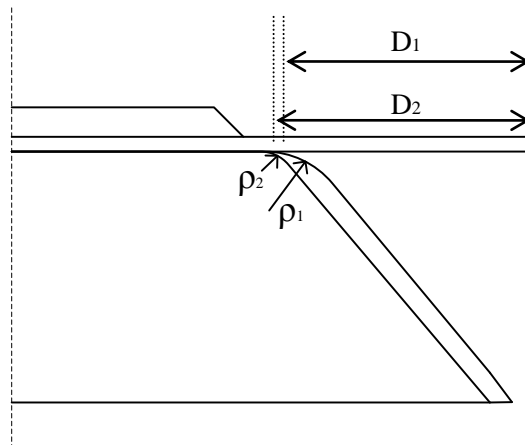


Figure 4.15: Effect of altering mandrel round off radius on deformable radius, *D*

This was tested further by performing four simulations on half cone angles of $40^{\circ}$ using blanks of radius 140mm. Two simulations were performed with mandrel rotational velocities of 600rpm and mandrel

round off radius of 15mm. The deformable radius was altered by performing one of these cases with a mandrel radius of 110mm and the other with a mandrel radius of 115mm. The remaining two simulations were performed with a mandrel rotational velocity of 200rpm and round off radius of 10mm and the deformable radius was altered by performing one simulation with a mandrel radius of 110mm and the other with a mandrel radius of 123mm. In both cases the simulations with the mandrel radius of 110mm exhibited wrinkling whereas the parts formed with a larger mandrel radius (and therefore a smaller value of $D$) formed without wrinkling. This demonstrates that $D$ has been confirmed as a formability parameter.

The transformed data from Kobayashi (1963) illustrated in Figure 4.12 shows that as the deformable radius is increased for a fixed half cone angle; a larger mandrel radius is required in order to prevent the part from wrinkling. Examination of the results shown in Figures 4.13 and 4.14 shows that as the mandrel round off radius is reduced (resulting in an increase in the deformable radius); the part is more likely to wrinkle. This evidence supports the proposition of $D$ as a formability parameter.

This concludes the first part of the chapter; a three-dimensional finite element model has been built to simulate the single pass conventional metal spinning of conical parts. Furthermore, a formability parameter has been proposed and a formability surface has been constructed in terms of the half cone angle, rotational speed and round off radius of the mandrel. The second half of the chapter continues by deriving a theoretical expression for the hoop force whose variation with respect to the formability parameter proposed in the first half of the chapter is investigated. The theoretical expression is derived by consideration of the deformation energy; therefore, it is first necessary to establish an expression for the hoop strain.

| Reference | Max theoretical force (N) to 3 s.f. | Max force simulation | Reference | Max theoretical force (N) to 3 s.f. | Max Simulation force |
|---|---|---|---|---|---|
| A30M25R600 | 44.0 | 931 | A30M15R600 | 44.0 | ------------ |
| A40M25R600 | 19.6 | 496 | A40M15R600 | 19.6 | ------------ |
| A50M25R600 | 7.88 | 1050 | A50M15R600 | 7.88 | 1120 |
| A60M25R600 | 2.65 | 903 | A60M15R600 | 2.65 | 1330 |
| A30M25R400 | 99.1 | 940 | A30M15R400 | 99.1 | 1110 |
| A40M25R400 | 44.1 | 933 | A40M15R400 | 44.1 | 1120 |
| A50M25R400 | 17.7 | 974 | A50M15R400 | 17.7 | 1300 |
| A60M25R400 | 5.97 | 1190 | A60M15R400 | 5.97 | 1390 |
| A30M25R200 | 396. | ———— | A30M15R200 | 396. | ———— |
| A40M25R200 | 176. | 536 | A40M15R200 | 176. | ------------ |
| A50M25R200 | 70.8 | 1300 | A50M15R200 | 70.8 | ------------ |
| A60M25R200 | 23.8 | 960 | A60M15R200 | 23.8 | 1080 |
| A30M20R600 | 44.0 | 1160 | A30M10R600 | 44.0 | 591 |
| A40M20R600 | 19.6 | 501 | A40M10R600 | 19.6 | 1140 |
| A50M20R600 | 7.88 | 743 | A50M10R600 | 7.88 | 587 |
| A60M20R600 | 2.65 | 1040 | A60M10R600 | 2.65 | 1190 |
| A30M20R400 | 99.1 | 450 | A30M10R400 | 99.1 | 760 |
| A40M20R400 | 44.1 | 1180 | A40M10R400 | 44.1 | 1480 |
| A50M20R400 | 17.7 | 1409 | A50M10R400 | 17.7 | 1060 |
| A60M20R400 | 5.97 | 1260 | A60M10R400 | 5.97 | 1200 |
| A30M20R200 | 396. | ------------ | A30M10R200 | 396. | ------------ |
| A40M20R200 | 176. | 1400 | A40M10R200 | 176. | ------------ |
| A50M20R200 | 70.8 | 1090 | A50M10R200 | 70.8 | 1210 |
| A60M20R200 | 23.8 | 943 | A60M10R200 | 23.8 | 1200 |

Table 4.4: Table of peak forces (to 3 s.f.) obtained from theoretical and numerical methods

## 4.4    Conclusions

In this chapter, a three-dimensional finite element model was built to simulate single pass conventional metal spinning of conical parts. A formability parameter, $D$, and an empirical relation for a formability surface (valid for mild steel with a blank radius of 140mm, and a mandrel radius of 110mm) were proposed and investigated. Both the formability parameter and the formability surface are original contributions to the body of knowledge of metal spinning. The empirical surface revealed that a part was found less likely to form without wrinkling taking place as the mandrel speed increased; similarly, decreasing the mandrel round off radius and mandrel half cone angle also reduced the likelihood of the part forming without wrinkling. Furthermore, the issues experienced by Zhang *et al*. (2012) in scaling parameters were explained in the derivation of the formability parameter, $D$.

In addition theoretical expression for the hoop force was derived from geometric considerations and taking into account the strain hardening properties of the material being formed. The trends observed that the hoop force increases as the blank thickness increases and as the half cone angle of the mandrel decreases are consistent with existing research. Furthermore, the theoretical expression was compared to the output from the finite element model developed in this chapter and was found to need scaling by expression (4.72) in order to account for the surface area in contact with the roller as the part is formed. The fact that the trend observed in the theoretical expression are similar to the trends observed in the numerical output indicates that the nature of the hoop force is largely influenced by the geometry of the part.

# §5    3D Springback

The previous chapter involved determining a formability surface in terms of the mandrel half cone angle, rotational speed and mandrel round off radius. Music *et al.* (2010) identified springback as a largely unstudied area within the context of metal spinning; despite the fact that it is an area of importance for industry since the springback experienced by a part may be large enough to render a part unsuitable for its intended purpose. Therefore, the simulations from the previous chapter that produced parts that were wrinkle free were used to study springback. At the present time, there is no agreed metric with which to measure springback within the context of metal spinning. In this chapter, the v-bending problem has been modelled in order to establish the suitability of ABAQUS for investigating springback. Following this, a study of springback in the three-dimensional parts formed using the three-dimensional model developed in the previous chapter is carried out. Of the parts formed in the previous chapter, only those that were wrinkle-free were considered for the springback study (unlike the results of Zhan *et al.* (2008) which were presented for wrinkled parts). The influence of the mandrel rotational speed ($\omega$), the mandrel round off radius ($\rho$) and the half cone angle of the mandrel ($\alpha$) in addition to the contact area between the roller and the workpiece on the observed springback are discussed in Sections 5.3, 5.4 and 5.5.

## 5.1    V-bending problem

 The aim of this test problem is to establish whether or not ABAQUS can be used to calculate springback via consideration of the problem of springback in three point V-bending of sheet metal. This test was chosen as it has been well studied and consequently, there is data available for comparison. The output of the model is verified by comparison with data presented in Lange (1985), which is reproduced here where appropriate via the digitalizing software, 'engauge' (online, 2010). This includes comparisons of results for the monotonic force versus bend angle relationship during the bending process, stress and strain distributions of sheet cross-section, bending curvature variations after bending and springback. The blank is meshed with the CPE4R element, which is a four node

first order reduced integration quadrilateral plane strain element available in both ABAQUS/Standard

and ABAQUS/Explicit student edition.

The modelling assumptions made in this solution were

1.  The material is isotropic;

2.  A line segment originally in the x-y plane remains in the x-y plane;

3.  The sheet has a sufficiently large dimension in the z-direction (illustrated in Figure 5.1) so as
    to justify the assumption of a plane strain problem;

4.  Only half of the problem needs to be modelled due to the symmetry;

5.  There is no friction between the punch and the blank top;

6.  There is kinematic friction between the blank bottom and the die surface;

7.  Apart from gravity and resistance due to friction, the blank can move freely

Figure 5.1 shows a representative geometrical model of the problem for use in the analysis.
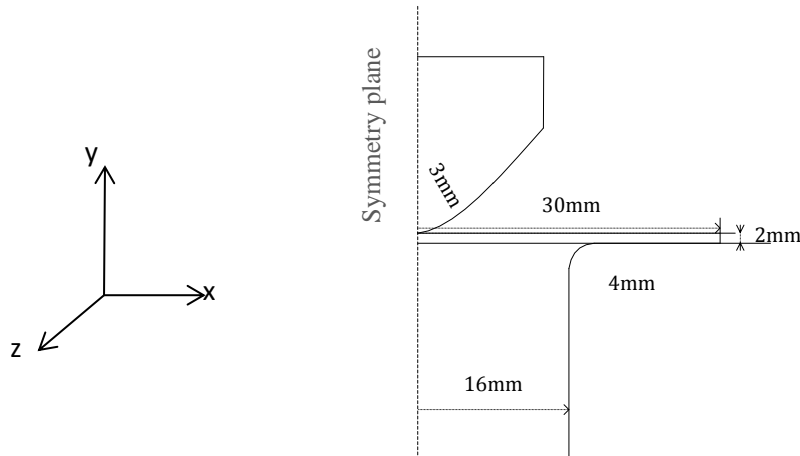


Figure 5.1: Diagram of the initial 2D configuration of the problem

Assumption 1 is easily incorporated into the model with the material definition of the section, where it

is also possible to define elastic and plastic behaviour. The process was modelled using two materials,

the first is 'real data' which is data from actual tensile tests on mild steel conducted by Metal Spinners

Group Ltd. and is the same material definition used for the three-dimensional model. The second

material used was 'aluminium' whose properties were taken from Matweb (online, accessed 2010) and was modelled as elastic-perfectly plastic. The material definition was the same as that which was used to test Kobayashi's (1963) data; the yield stress for aluminium was 10MPa, the Young's modulus was taken to be 70GPa, the Poisson's ratio was taken to be 0.35 and the density was taken to be 2700 kgm$^{-3}$. These two materials were chosen since Lange (1985) presents springback data for mild steel and aluminium which were used for comparison with the output of the numerical model. The punch and die are modelled as 2D analytical rigid objects and the blank is modelled as a deformable 2D part.

After the forming stage is completed in ABAQUS/Explicit (recommended for simulations involving dynamic contact), the resulting stress state of the part is then read into ABAQUS/Standard for the springback simulation.

In the initial step, displacement components are set to be zero at the reference point of the die shoulder (shown in Figure 5.1); this condition is propagated throughout the analysis. At the punch reference point (also shown in Figure 5.1), all degrees of displacement are also set to zero in the initial step, this condition is modified in the forming step to allow the punch to be displaced 14mm vertically downwards. In addition, a set is defined at the left hand edge of the blank. This edge is subjected to an symmetry boundary condition where all degrees of displacement (with the exception of the vertical degree of displacement) are set to zero throughout the analysis. The coefficient of friction was taken to be 0.1 in order to compare with data shown in Lange (1985).

The mesh for the blank was generated using, plane strain element CPE4R, which is the only plane strain element available in the student addition of ABAQUS. This element is a four node, first order plane strain reduced integration element with hourglass control which is recommended for simulations involving large mesh distortions since they eliminate shear locking and hour-glassing can be avoided if multiple elements are used through the thickness (Simula, 2010). A further restriction is that the student edition is restricted to one thousand nodes. Mesh refinement was enabled so that the

mesh was finer nearer the symmetry line of the problem in order to attempt to capture the deformation as accurately as was as reasonably practicable.

The bend angle is defined as the angle of inclination between the blank and the horizontal and was calculated using (5.1).

$$\theta = \left(\frac{180}{\pi}\right) \tan^{-1}\left(\frac{y_2 - y_1}{x_2 - x_1}\right) \tag{5.1}$$

where $\theta$ is the bend angle in degrees and $(x_1, y_1)$, $(x_2, y_2)$ are the coordinates of two points on the top surface of the blank shown in yellow in Figure 5.2. These points were chosen because they remain along a straight line.



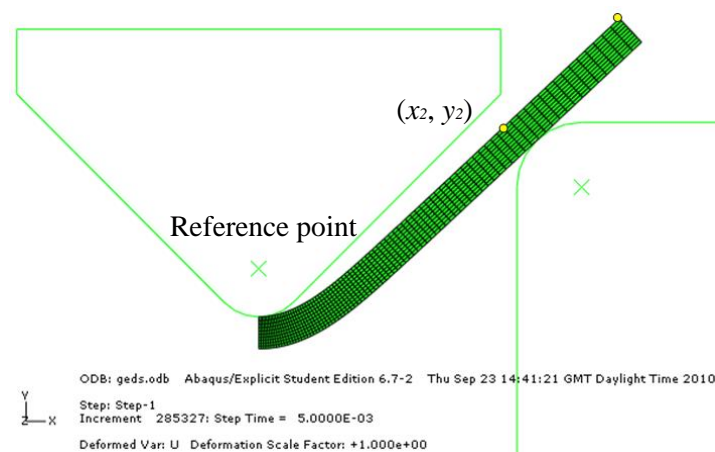Figure 5.2: Coordinates used to calculate the bend angle

The force versus bend angle relationship shown in Figure 5.3 compares well with the trends shown in Lange (1985). Unfortunately, it is not possible to compare completely with the results presented in the text since neither Lange (1985) or the original papers referenced therein (in German) give sufficient material properties for an FEA simulation.
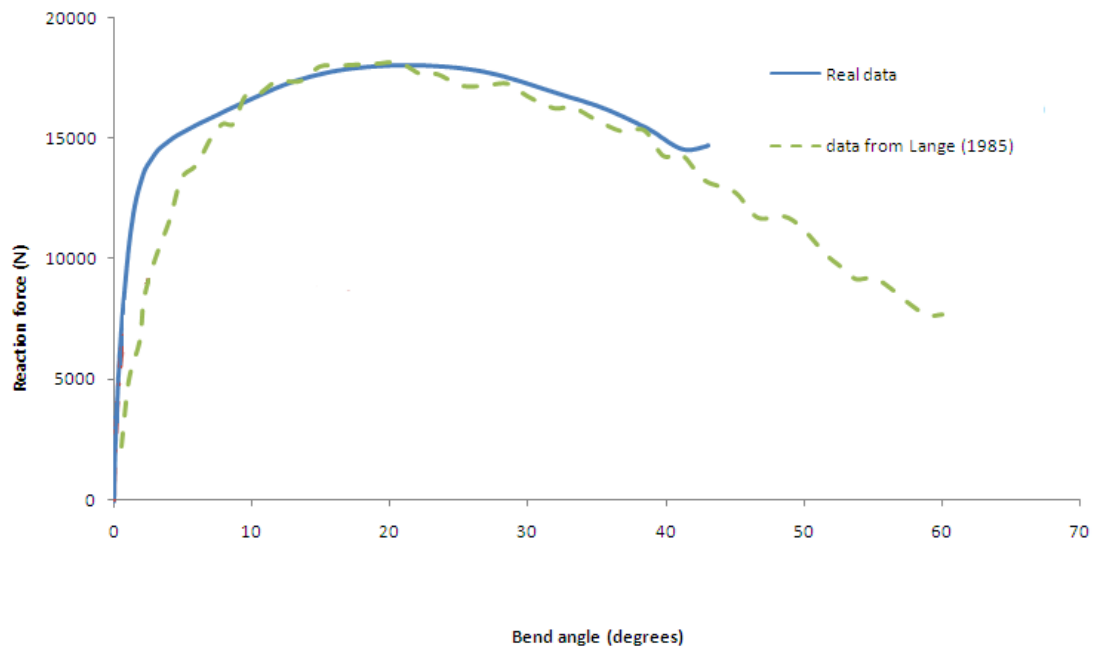
Figure 5.3: Reaction Force versus Bend angle relationship

The data from Lange (1985) is stated as AISI 1050 mild steel although no further details are given. Therefore, for this study, the material properties used to model the mild steel are the same as those used in the previous chapter. For bend angles greater than around $13^{o}$, the data from Lange (1985) gives very similar results to those obtained using the real data in ABAQUS/Explicit. The difference at smaller bend angles is likely to be attributed to any differences in the yield stress between the material used in Lange's (1985) experiments and the property definitions used in the numerical model.

Once the forming stage has been completed in ABAQUS/Explicit, the resulting stress state is then read into ABAQUS/Standard for the springback analysis. Figures 5.4, and 5.5 show the initial and final positions of the formed part for the materials defined as 'real data' and 'aluminium', respectively. In each case, the green plot represents the final position of the blank after springback. Since the observed springback for aluminium was very small, the displacement has been enlarged by a factor of 10.
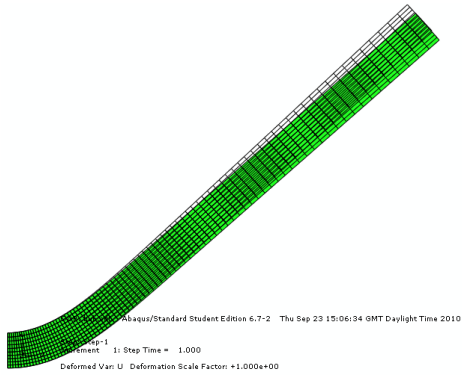
Figure 5.4: Springback – 'real data'
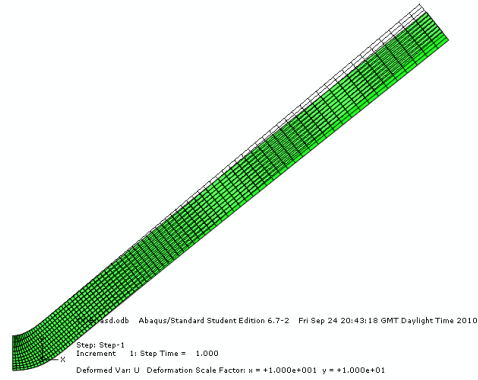
Figure 5.5: Springback, exaggerated for 'aluminium'

Results for springback using different materials are shown in Table 5.1. In this table, frame zero corresponds to the state before springback and frame one corresponds to the position of the part after springback.

The springback ratio, K, is defined in Lange (1985) to be the ratio of the bend angle after springback to the bend angle before springback (i.e. a springback ratio of 1 corresponds to no springback).

| Frame | Material | X1<br><br>(3 s.f.) | Y1<br><br>(3 s.f.) | X2<br><br>(3 s.f.) | Y2<br><br>(3 s.f.) | Angle (degees)<br><br>(3 s.f.) | Difference (degrees)<br><br>(3 s.f.) | K, (Springback ratio) (3s.f.) |
|---|---|---|---|---|---|---|---|---|
| 0 | Real data | 3.30e-3 | 9.69e-3 | 8.36e-3 | 14.4e-3 | 43.1 | | |
| 1 | Real data | 3.63e-3 | 9.35e-3 | 8.83e-3 | 13.9e-3 | 41.4 | 1.68 | 0.961 |
| 0 | Aluminium | 3.42e-3 | 9.66e-3 | 8.72e-3 | 14.1e-3 | 39.97 | | |
| 1 | Aluminium | 3.44e-3 | 9.63e-3 | 8.76e-3 | 14.1e-3 | 39.8 | 0.141 | 0.996 |

Table 5.1: Results for springback using different materials

The springback ratio was calculated to be 0.982 for 'real data' and 0.996 for aluminium, which is in good agreement with Lange (1985) since the data presented in Lange (1985) shows that for "structural steel" the springback ratio was 0.97 and for aluminium, the springback ratio was 0.99.

Lange (1985) presents stress plots through the thickness of the material, which is shown in Figure 5.6. The material properties were not given.
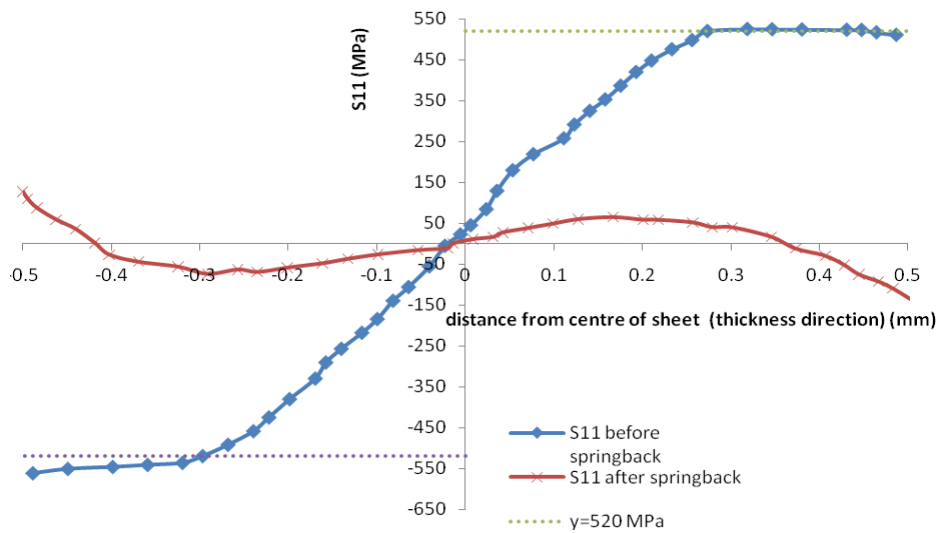


Figure 5.6: Principal stress components presented by Lange (1985).

Lange (1985) stated that theoretically, the stress component should level out at the yield stress of the material. It can be seen that the experimental results correlate well with the theory, although the zero stress state does not correspond exactly to the centre of the sheet, but slightly towards the compressive surface (the surface that would have been in contact with the punch).

The through thickness radial (principal) stress distribution (along the line of symmetry of the sheet) before and after springback are also in good agreement with Lange (1985); these are shown in Figures 5.7, 5.8 and 5.9 using the 'real data' and 'aluminium' material definitions, respectively. In each of the plots, a distance of zero corresponds to the top surface of the blank (the side of the blank which was in contact with the punch).
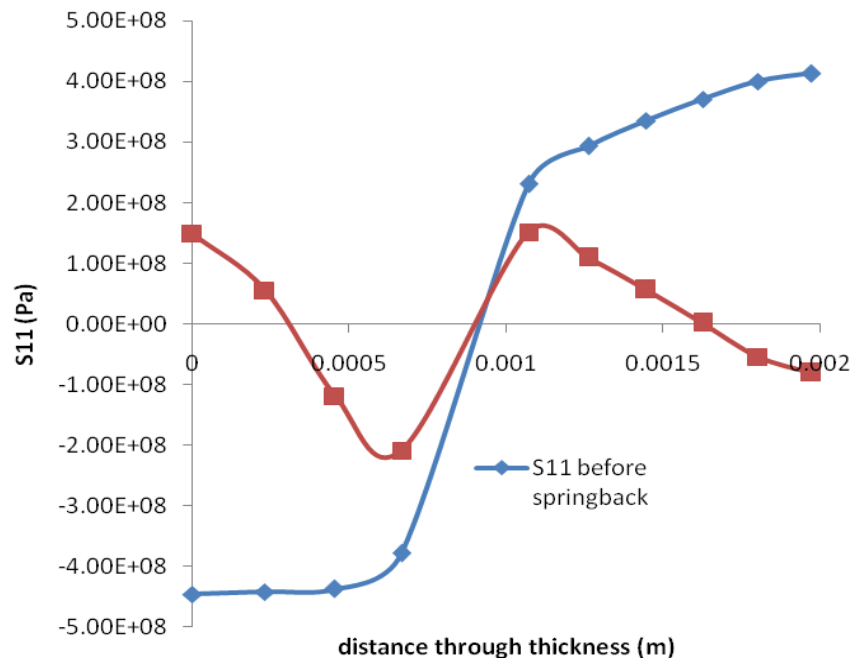
Figure 5.7: Stress plot for 'real data'.
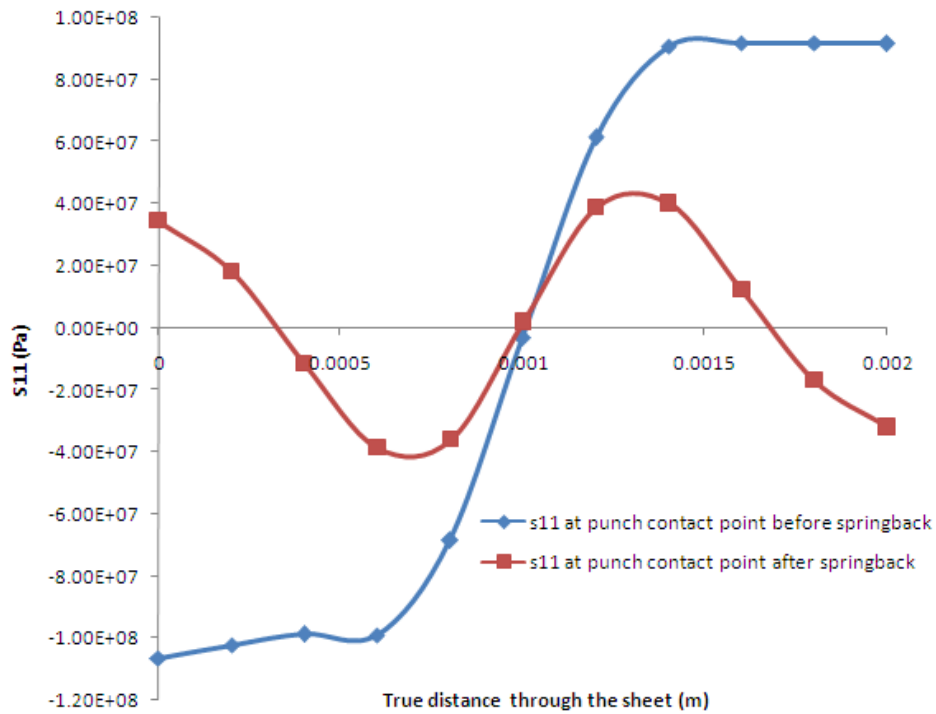


Figure 5.8: Stress distribution for aluminium
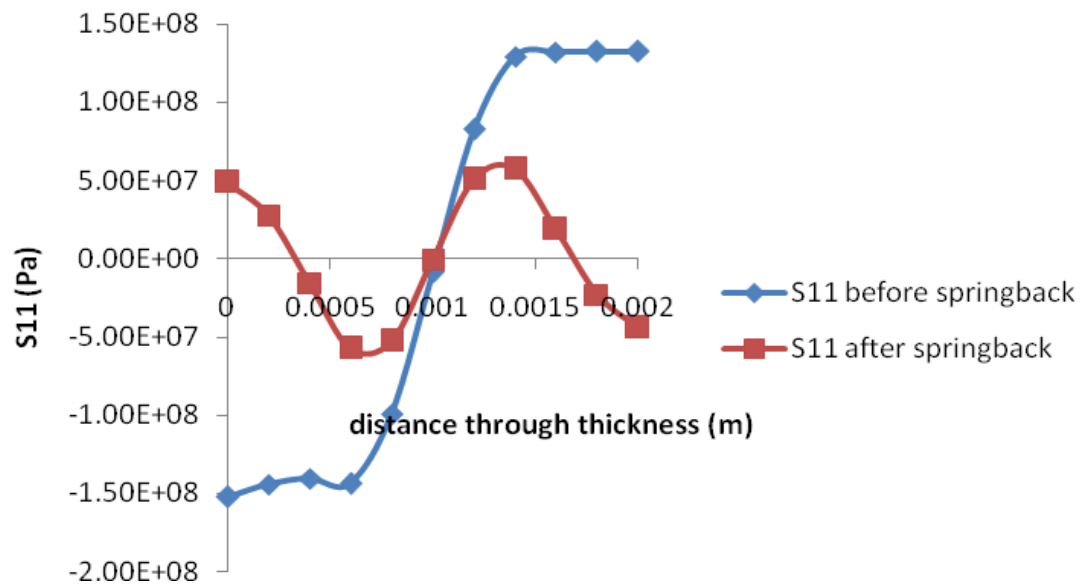
Figure 5.9: Through thickness stress distribution for elastic-perfectly plastic model of mild steel

It can be seen that Figures 5.7, 5.8 and 5.9 also follow the trend of the experimentally measured stresses of Figure 5.6. Both the Figures demonstrate that the stress before springback reaches a maximum at the defined yield stress of the material. For the case of 'real data', the stress peak mid-way through the sheet are greater than illustrated by Lange (1985); this was attributed to the material model used. Therefore, the simulation was repeated using an elastic-perfectly plastic model for the mild steel (preserving the values of the yield stress and Poisson's ratio). The results show a better agreement for the peak occurring part way through the material thickness although the stresses at the outer surfaces were larger than shown for Lange (1985); this is due to the thickness of the sheet used in the numerical model.

The final comparison to be made is for the strain distributions along the line of symmetry of the blank through the sheet thickness. Figure 5.10 shows the radial strain (component 11) and thickness strain (component 22) distributions after springback for the real data.
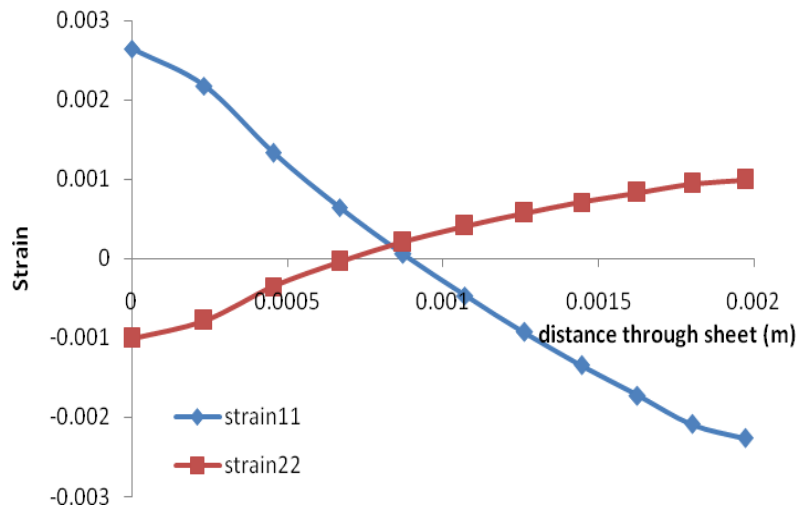
Figure 5.10: Strain distribution 'real data' after springback

The fact that the magnitude of the radial strain distribution is approximately three times the magnitude of the thickness strain distribution is in agreement with the Poisson's ratio (which has a value of 0.3 implying that the ratio of the strain in the radial direction to the strain in the thickness direction should be 0.3).

In conclusion, it is reasonable to state that a successful FEA solution has been found to the problem of springback in 3-point V bending of sheet metal. This statement is based on the agreement of the force-bending angle relationship, the cross-sectional stress distributions before and after springback and comparisons between observed springback and results available in the literature (Lange (1985)). It has also highlighted the importance of defining the correct material properties if direct comparisons are to be made between FEA results and actual experimental data. Therefore, it is appropriate to continue to use ABAQUS/Standard to measure the springback in this study.

## 5.2    Defining Springback

Zhan *et al*. (2008) attempted to quantify the springback in the forming of a $40^0$ cone. The authors stated a single value for the final cone angle of the formed part and did not present any calculations as to how to this value was obtained. Neither do they provide any indication as to whether the springback is uniformly distributed around the part. As described in the previous section, the springback ratio is a measure of springback defined for bending problems where it is not possible to exceed the intended angle, hence the value of the springback ratio is always less than or equal to 1. In the spinning process, deformation occurs around the round off radius of the mandrel, as illustrated in Figure 5.11. Consequently it is possible to get half cone angles which are either greater than or less than the intended half cone angle. The springback ratio is traditionally calculated by considering the angle change during the unloading process. However, for the metal spinning process, it is also important to note that deviation of the cone angle also occurs as a direct result of the forming process itself, this is referred to as 'in-process springback' and in this research is calculated in the same way as the springback due to unloading. In order to calculate the value of the springback, two circumferential paths which pass through the points $(r_{base}, z_{base})$ and $(r_{circ}, z_{circ})$ illustrated in Figure 5.11, were defined. The half cone angle was calculated for each pair of points and hence this provides an average value of the half cone angle of the part. The inner surface of the part was chosen for the springback calculation so as not to allow the thickness strain to influence the calculations.
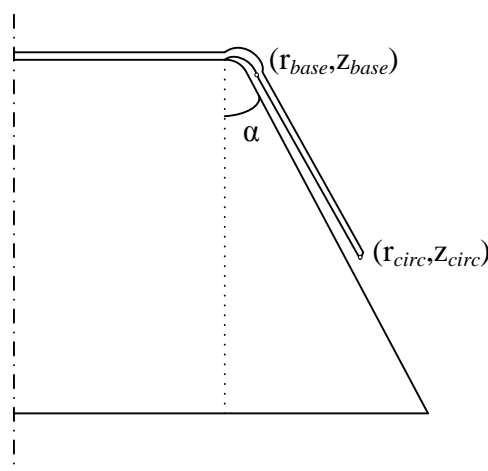


Figure 5.11: Geometry of the part after the forming process

The half cone angle (in degrees) of the part at the end of the forming stage is calculated as:

$$\alpha_f = \left(\frac{180}{\pi}\right)\arctan\left(\frac{z_{circ} - z_{base}}{r_{circ} - r_{base}}\right)$$  (5.2)

where

$\alpha_f$        is cone angle (in degrees) of the part at the end of the forming stage (including the in-process springback)

$z_{circ}$, $z_{base}$ are the z coordinates of the circumferential and base points illustrated in Figure 5.11 at the end of the forming process, respectively

$r_{circ}$, $r_{base}$ are the r coordinates of the circumferential and base points illustrated in Figure 5.11 at the end of the forming process, respectively

In a similar fashion, the cone angle of the part after unloading, $\alpha_{sb}$, is calculated from equation (5.2) where the coordinates $\left(r_{circ}, z_{circ}\right)$ and $\left(r_{base}, z_{base}\right)$ are replaced with $\left(r_{circ\_sb}, z_{circ\_sb}\right)$ and $\left(r_{base\_sb}, z_{base\_sb}\right)$ where:

$z_{circ\_sb}$, $z_{base\_sb}$ are the z coordinates of the circumferential and base points illustrated in Figure 5.11 after springback, respectively

$r_{circ\_sb}$, $r_{base\_sb}$ are the r coordinates of the circumferential and base points illustrated in Figure 5.11 after springback, respectively

The springback angle is defined as the deviation in half cone angle of the part after unloading has taken place, and is calculated as:

$$\psi = \alpha_{sb} - \alpha_f$$  (5.3)

where $\psi$ is the springback angle.

Although it is not explicitly known whether or not springback occurs uniformly around the circumference of the part, it is known that the part does not initially form uniformly around the circumference of the part. Therefore, it is reasonable to assume that springback is likely to be non-uniform in the conventional metal spinning process. The springback angle was calculated for every pair of nodes (with equal circumferential coordinates) as illustrated in Figure 5.11 and plots generated. The final roller contact point is represented by a triangle on each plot. In the following sections, the unloading springback ratio (defined as the ratio of the half cone angle of the part after unloading to the half cone angle of the part after the forming stage which is analogous to the definition of the springback ratio in the v-bending study) will be calculated to quantify the angle change during the unloading process. For the in-process springback; the springback ratio is defined as the ratio of the half cone angle of the part to the intended half cone angle of the part (the half cone angle of the mandrel).

## 5.3    Springback variation with respect to cone angle and round off radius

In bending problems, such as the test problem used at the beginning of this chapter; springback is attributed to the notion that through the thickness of the blank there is a layer which does not undergo plastic deformation therefore remains elastic (Valberg (2010)). This is logical since the material on the outer surface of the bend is under tension, whilst the material on the inner surface of the bend is subjected to compression. This theory is valid for the assumption of plane strain, which is not a valid assumption in metal spinning. In order to see how far this rationale may be extended to the study of springback in metal spinning, plots were generated for in process springback, unloading springback and the total springback for three investigated mandrel speeds. These plots are shown in Figures 5.12-5.17, the value of the springback ratio plotted in each case has been obtained by averaging the springback calculated at every node around the circumference of the part.
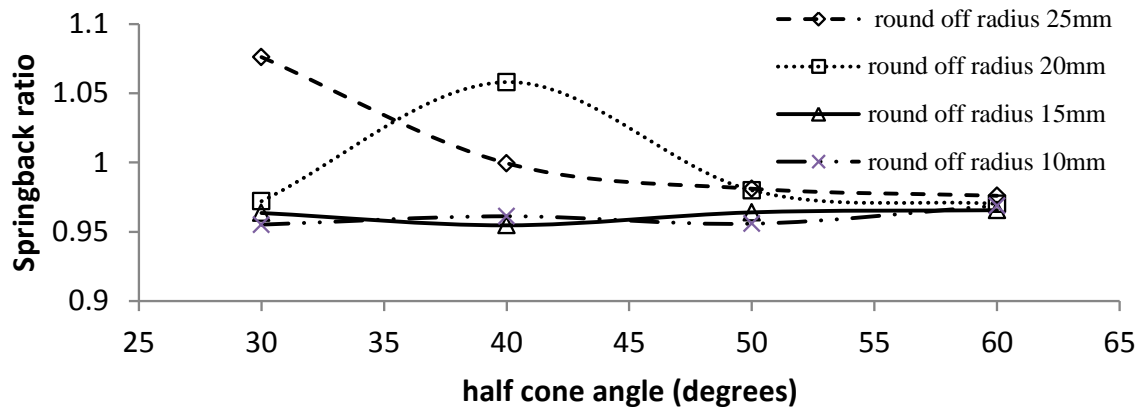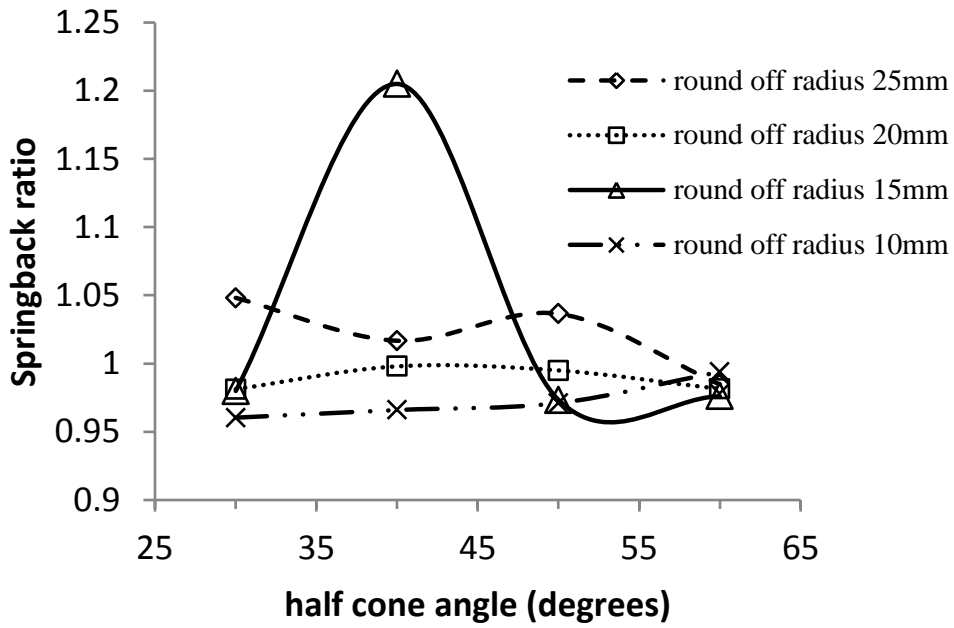
Figure 5.12: In process springback for 600rpm



Figure 5.13: In process springback for 400rpm
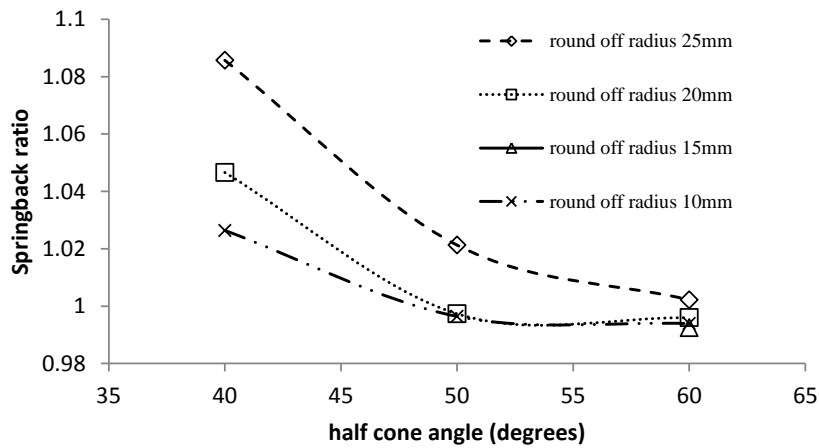
Figure 5.14: In process springback for 200rpm

Figures 5.12-5.14 show that as the half cone angle increases, the mandrel round off radius becomes less influential in the generation of in process springback; that is to say that as the half cone angle increases, less in process springback is observed and the value of the springback ratio converges towards a common value (close to unity). This represents the fact that the part is subjected to less deformation as the half cone angle increases.

The clearest trend for the plots 5.12-5.14 is illustrated in Figure 5.14; which shows the in-process springback for mandrel rotational speed 200rpm. This plot clearly shows that at 200rpm, the in-process springback is greater for a greater round off radius, this can be attributed to the fact that a larger round off radius induces less plastic strain than a smaller round off radius. This observation appears to be somewhat analogous to the experimental springback ratio data available for the v-bending process (Valberg, (2010); Lange (1985)) that shows that the observed springback increases as the ratio of bend radius to thickness increases. In the published literature, there has been a debate as to the mechanics of the metal spinning process and whether it most closely resembles a bending process, deep drawing or a combination of a number of different processes. The plots shown in Figures 5.12-5.14 would imply that if the mechanics of the metal spinning process is a combination of other forming processes, then as the mandrel rotational velocity is decreased, the bending behaviour becomes more evident since the springback plots shown in Figure 5.14 begin to resemble the v-

bending data presented by Lange (1985). Conversely, as the mandrel rotational speed is increased, the springback plots begin to deviate from the pattern shown in Figure 5.14 (analogous to the data presented by Lange (1985)). It is also interesting to note that as the mandrel rotational speed is increased, the springback ratio decreases with the exception of half cone angle $60^{\circ}$. This would indicate that for smaller half cone angles, the springback ratio is sensitive to the mandrel rotational speed.

In order to test the extent to which the unloading springback can be compared to the bending process, similar plots were generated and are shown in Figures 5.15-5.17.  Again, the clearest trend was observed for the simulations carried out at 200rpm. In all the cases listed in Table 5.2, the in process springback caused a greater deviation from the desired cone angle than the springback due to unloading. Furthermore, since Figures 5.15-5.17 show no clear trend with respect to mandrel round off radius, it appears that the mandrel round off radius has much less impact upon the unloading springback than on the in-process springback. Upon inspection of the resulting cone angles after forming and after unloading, it was noted that for a greater mandrel rotational speed, the springback due to unloading actually brought the average cone angle closer to the desired value. Consequently, it can be stated that the majority of the total springback generated may be attributed to in-process springback.  Table 5.2 shows the half cone angles of the parts after forming and unloading and the corresponding springback ratios to 3 significant figures.

| Simulation | Angle after forming | Angle after unloading | unloading springback ratio | In-process springback ratio | Total springback ratio |
|---|---|---|---|---|---|
| A30M25R600 | 32.2 | 32.2 | 0.999 | 1.07 | 1.07 |
| A40M25R600 | 39.9 | 39.9 | 1.00 | 0.999 | 0.999 |
| A50M25R600 | 49.0 | 49.1 | 1.00 | 0.981 | 0.982 |
| A60M25R600 | 58.5 | 58.5 | 0.999 | 0.975 | 0.975 |
| A30M25R400 | 31.4 | 31.4 | 1.00 | 1.04 | 1.04 |
| A40M25R400 | 40.6 | 40.6 | 0.999 | 1.01 | 1.01 |
| A50M25R400 | 51.8 | 51.7 | 0.999 | 1.03 | 1.03 |
| A60M25R400 | 59.0 | 59.0 | 1.00 | 0.984 | 0.984 |
| A40M25R200 | 43.4 | 43.4 | 1.00 | 1.08 | 1.08 |
| A50M25R200 | 51.0 | 51.0 | 0.999 | 1.02 | 1.02 |
| A60M25R200 | 60.1 | 60.1 | 0.999 | 1.00 | 1.00 |
| A30M20R600 | 29.1 | 29.1 | 0.999 | 0.972 | 0.971 |
| A40M20R600 | 39.0 | 39.0 | 1.00 | 0.975 | 0.976 |
| A50M20R600 | 48.9 | 49.0 | 1.00 | 0.979 | 0.980 |
| A60M20R600 | 58.2 | 58.2 | 1.00 | 0.970 | 0.970 |
| A30M20R400 | 29.4 | 29.4 | 0.998 | 0.981 | 0.980 |
| A40M20R400 | 39.9 | 39.9 | 1.00 | 0.997 | 0.998 |
| A50M20R400 | 49.7 | 49.7 | 0.999 | 0.994 | 0.994 |
| A60M20R400 | 58.8 | 58.8 | 0.999 | 0.981 | 0.980 |
| A40M20R200 | 41.8 | 41.8 | 0.999 | 1.04 | 1.04 |
| A50M20R200 | 49.8 | 49.8 | 0.999 | 0.997 | 0.997 |
| A60M20R200 | 59.7 | 59.7 | 0.999 | 0.995 | 0.995 |
| A30M15R600 | 28.9 | 28.9 | 1.00 | 0.963 | 0.964 |
| A40M15R600 | 38.1 | 38.1 | 0.999 | 0.954 | 0.953 |
| A50M15R600 | 48.1 | 48.1 | 0.999 | 0.963 | 0.963 |
| A60M15R600 | 57.9 | 57.9 | 0.999 | 0.965 | 0.965 |
| A30M15R400 | 29.3 | 29.4 | 1.00 | 0.979 | 0.980 |
| A40M15R400 | 39.3 | 39.2 | 0.999 | 0.982 | 0.982 |
| A50M15R400 | 48.6 | 48.6 | 0.998 | 0.973 | 0.972 |
| A60M15R400 | 58.5 | 58.5 | 0.999 | 0.976 | 0.975 |
| A60M15R200 | 59.5 | 59.5 | 0.999 | 0.992 | 0.992 |
| A30M10R600 | 28.6 | 28.6 | 1.00 | 0.955 | 0.955 |
| A40M10R600 | 38.4 | 38.4 | 1.00 | 0.961 | 0.961 |
| A50M10R600 | 47.7 | 47.8 | 1.00 | 0.955 | 0.956 |
| A60M10R600 | 58.1 | 58.1 | 1.00 | 0.968 | 0.969 |
| A30M10R400 | 28.8 | 28.8 | 1.00 | 0.960 | 0.960 |
| A40M10R400 | 38.6 | 38.6 | 0.999 | 0.965 | 0.965 |
| A50M10R400 | 48.5 | 48.5 | 0.999 | 0.971 | 0.970 |
| A60M10R400 | 59.6 | 59.6 | 0.999 | 0.993 | 0.993 |
| A40M10R200 | 41.0 | 41.0 | 1.00 | 1.02 | 1.02 |
| A50M10R200 | 49.8 | 49.8 | 1.00 | 0.996 | 0.996 |
| A60M10R200 | 59.6 | 59.6 | 0.999 | 0.993 | 0.993 |

Table 5.2: Cone angles after forming and unloading and the respective springback ratios to 3 s.f.
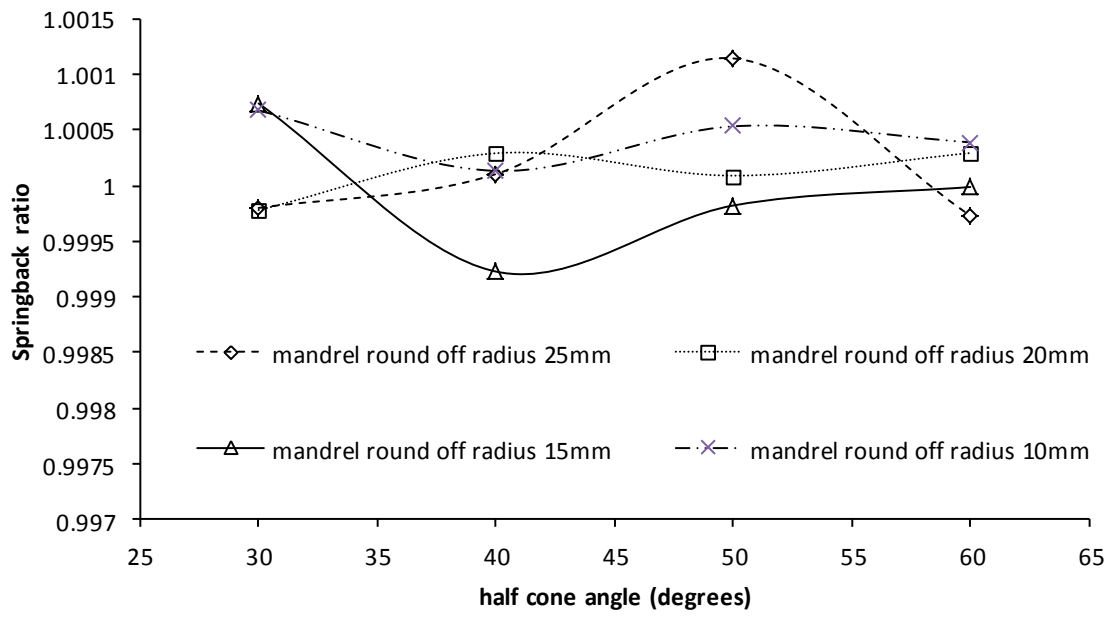
Figure 5.15: Unloading springback for 600rpm
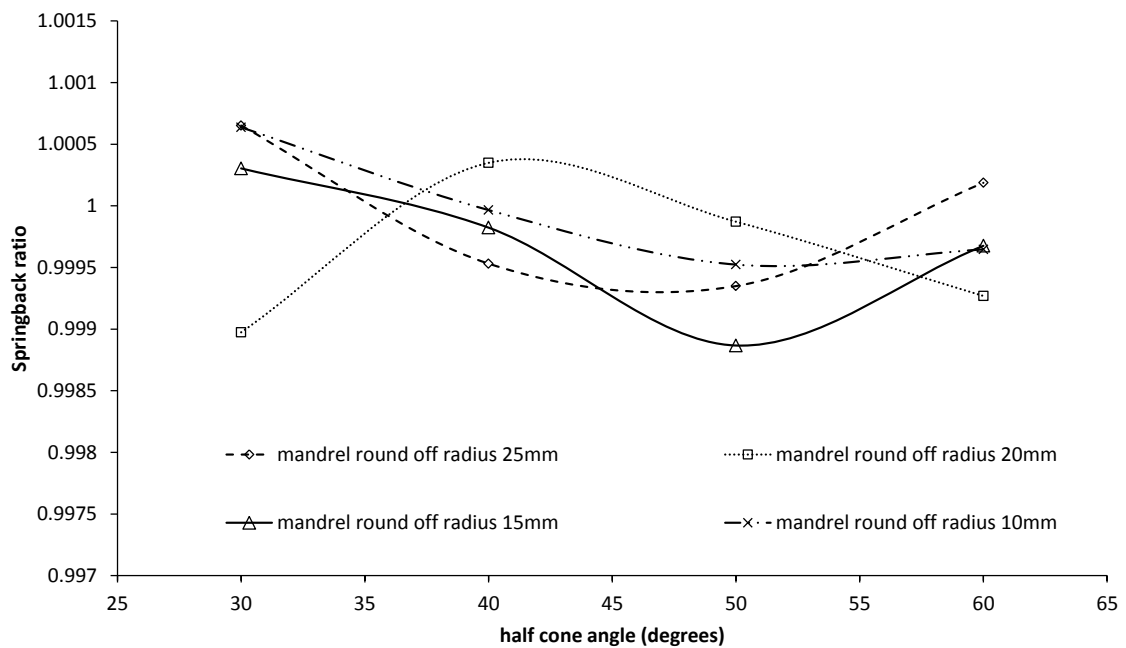


Figure 5.16: Unloading springback for 400rpm

104
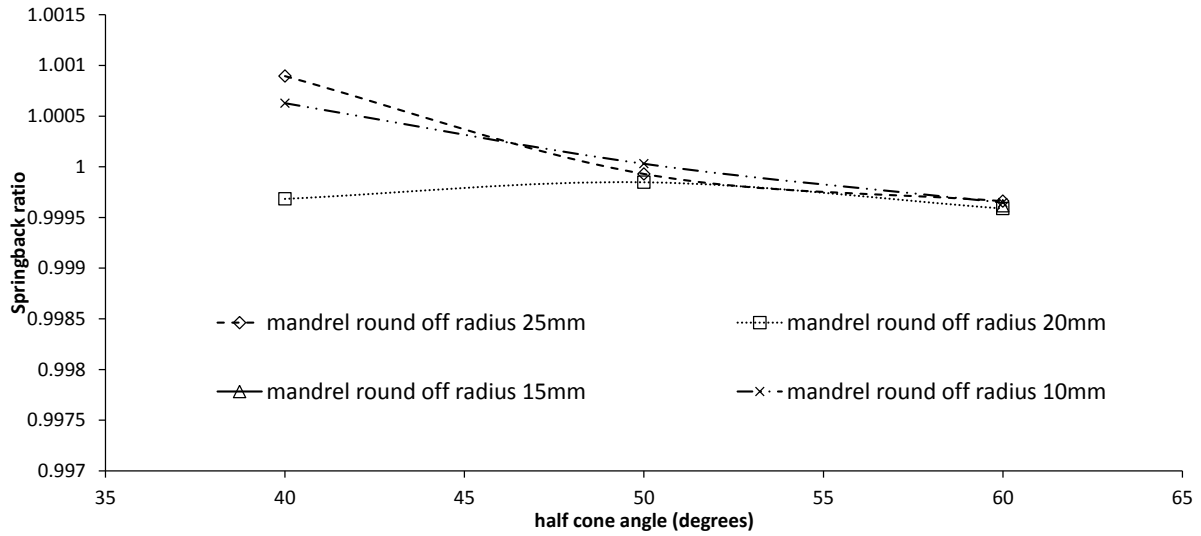
Figure 5.17: Unloading springback for 200rpm

Since springback may be seen as the redistribution and release of residual stresses, plots of the unloading springback were generated to examine the behaviour of unloading springback around the circumference of the part. These plots reveal that as the round off radius is decreased, a clover like pattern can be observed to emerge; this is illustrated in Figures 5.18, 5.19, 5.20, and 5.21. This pattern appears to be dependent primarily upon the mandrel round off radius. In each of the Figures 5.18 – 5.28 the solid circle represents a zero change in half cone angle, the innermost circle represents a half cone angle change of -0.05$^{\circ}$ and the outermost circle represents a change of 0.05$^{\circ}$ in the half cone angle of the part.
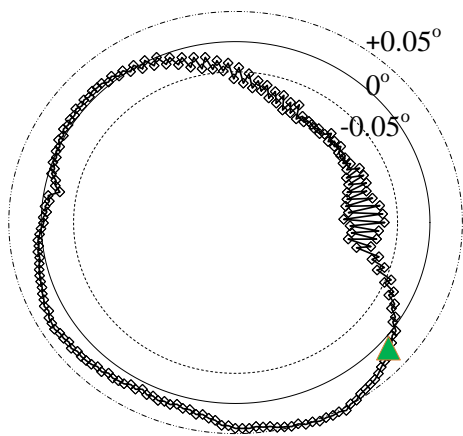
Figure 5.18: Unloading springback for
A30M25R400
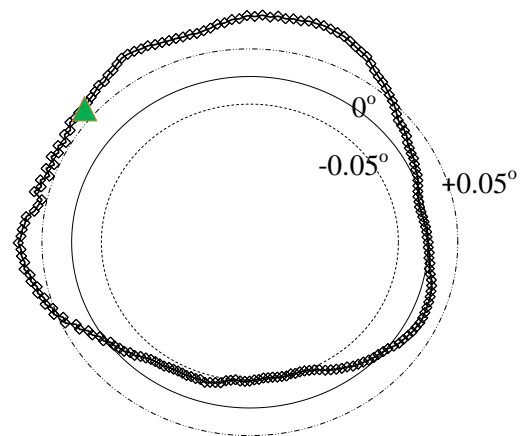


Figure 5.19: Unloading springback for
A30M20R400
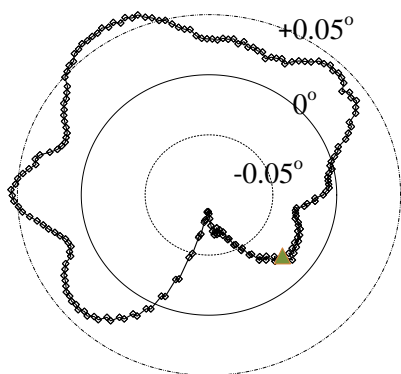


Figure 5.20: Unloading springback for
A30M15R400
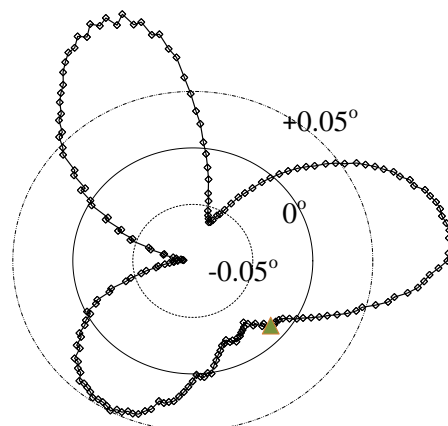


Figure 5.21: Unloading springback for
A30M10R400

In order to uncover a reason for the clover-like patterns; plots were generated for the thickness strain and displacement around the circumference of the part. Figure 5.22 shows the springback plot obtained for simulation A30M10R600; Figure 5.23 shows the corresponding circumferential plots for the thickness strain.
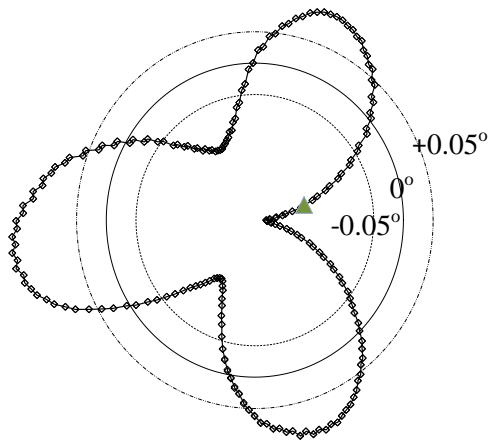
Figure 5.22: Springback plot for A30M10R600
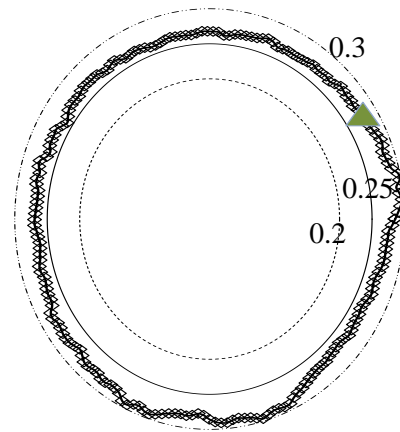
Figure 5.23: Thickness strain around the circumference of A30M10R600

The outer concentric circle represents a thickness strain of 0.3, the solid concentric circle represents a thickness strain of 0.25 and the inner concentric circle represents a thickness strain of 0.2. A similar plot was generated for the thickness strain for the circumferential path close to the mandrel round off radius (which was used to calculate the springback ratio) and for the hoop strain around the circumference; neither plot revealed any correlation to the springback plots. Consequently, there appears to be no link between the thickness strain and the unloading springback plots generated. A further line of investigation was to examine the possibility of a relationship between the final contact point between the roller and the resulting springback. The green triangle which appears on the plots in this Chapter represents the final contact point of the roller with the part. Examination of all the unloading springback plots revealed that in 18 cases, the roller endpoint did occur at a 'trough', for example in Figure 5.21. In 21 cases, the roller endpoint did not occur at the same point as a 'trough'. Of these 21 cases, 6 plots did not have troughs present, for example Figure 5.19. Therefore, from this data, it is not possible to establish a link between the roller endpoint and the springback pattern; in fact, the springback pattern appears to be independent of the roller endpoint.

## 5.4    Springback variation with respect to mandrel velocity

Examining the plots with respect to mandrel rotational velocity to establish any relationship between the mandrel rotational velocity and the in process springback pattern, revealed that in general little change was observed to occur as illustrated by Figures 5.24-5.26. Figures 5.27-5.28 show that the mandrel rotational speed also has minimal impact on the springback pattern where the cardioid pattern has fully developed.
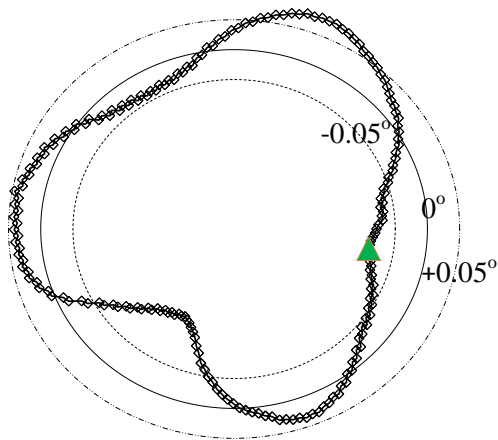


Figure 5.24: Unloading springback for
A60M20R600
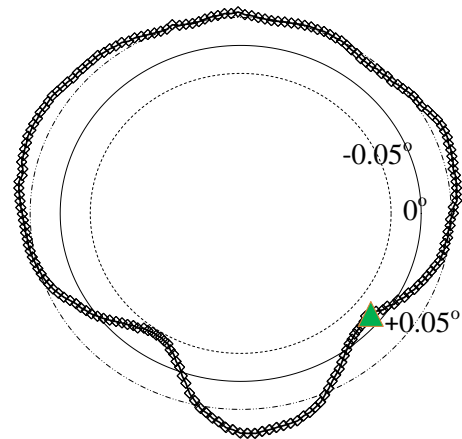


Figure 5.25: Unloading springback for
A60M20R400
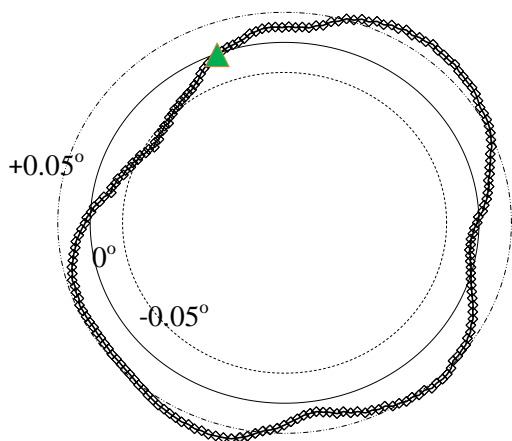


Figure 5.26: Unloading springback for
A60M20R200
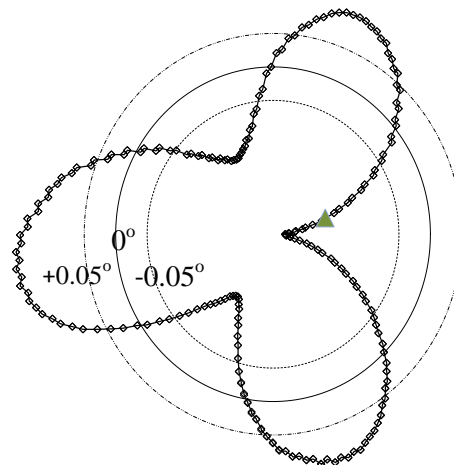


Figure 5.27: Unloading springback for
A30M10R600
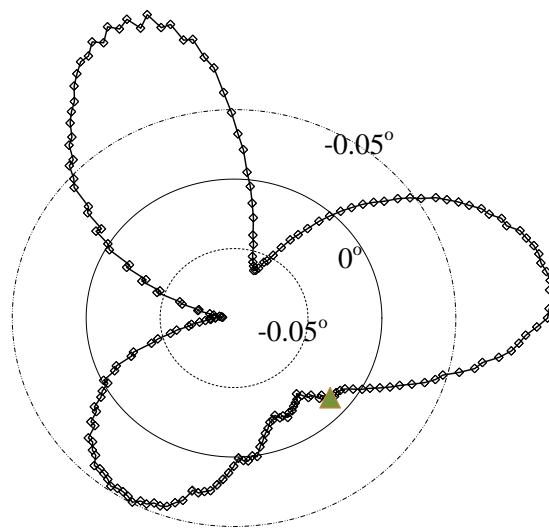
Figure 5.28: Unloading springback for A30M10R400

The lack of variation in the unloading springback pattern with respect to mandrel rotational speed implies that the nature of the unloading springback pattern is dependent upon geometrical considerations such as the mandrel round off radius and the half cone angle of the part being formed.

However, whilst the plots 5.24-5.28 show little variation in the fundamental pattern produced on the plots for the unloading springback; Figure 5.29 shows that the magnitude of the springback ratio for the total deviation from the cone angle generally (as a result of both the in process and unloading springback) reduces as the mandrel rotational speed increases. Furthermore, Figure 5.29 demonstrates that with the exception of the parts with a $40^o$ half cone angle, of the rotational speeds tested, 200rpm appears to be the optimal speed when considering the total springback as the in process springback dominates the unloading springback. In order to investigate this further, the data was re-plotted in terms of the feed rate.
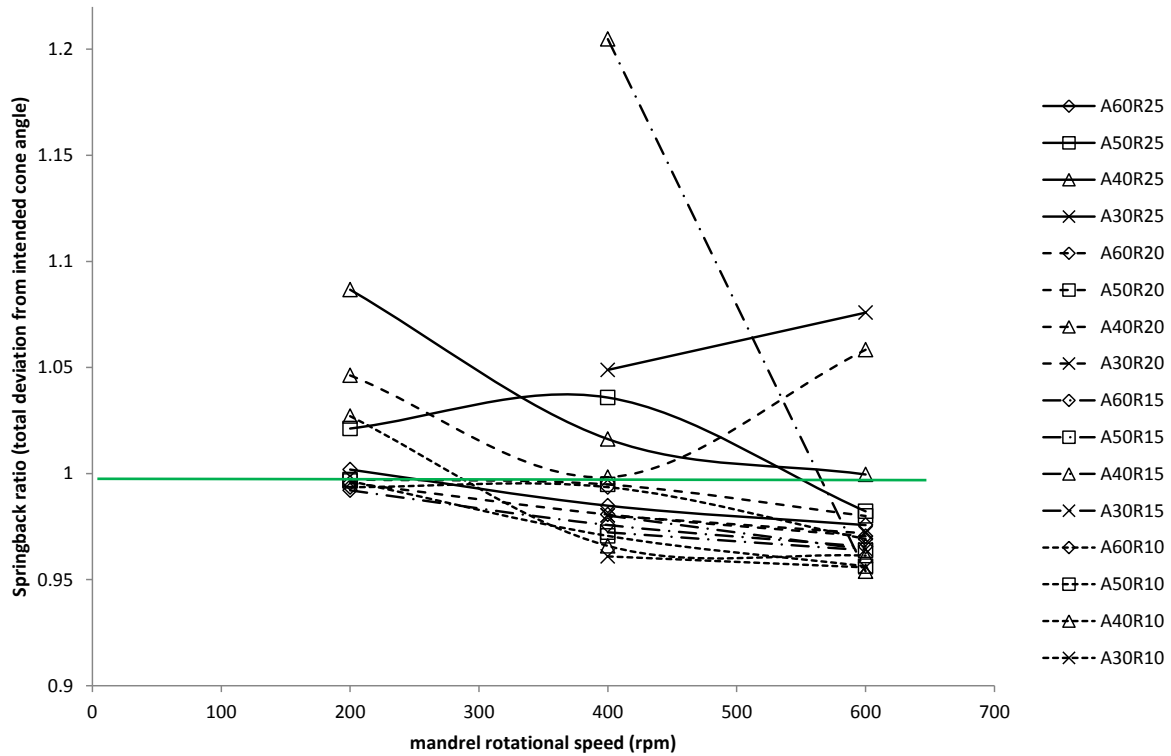
Figure 5.29: Variation of total springback ratio with mandrel rotational speed

The definitions of the simulations used for Figure 5.29 are the same as the definitions as used in Table 4.4. In each case, the number which follows the letter A is the half cone angle of the mandrel used in the simulation, the number which follows the letter M represents the mandrel round-off radius and the number which follows the letter R is the rotational speed of the mandrel throughout the simulation.

Figure 5.30 is the data from Figure 5.29 re-plotted in terms of the Feed rate, F, calculated from

$$F = 60 \frac{v}{\omega} \sin \alpha \qquad (5.4)$$

where $v$ is the roller velocity, $\omega$ is the mandrel rotational speed and $\alpha$ is the half cone angle of the mandrel. This formula is derived by considering the distance moved along the inclined surface of the mandrel. The blue line on Figure 5.30 represents no deviation in the half cone angle of the formed

part from the intended half cone angle. Figure 5.30 demonstrates that the springback ratio decreases with increasing feed rate; that is to say that as the feed rate is increased the final cone angle of the formed part becomes smaller. This is likely to be due to the fact that as the feed rate is increased, the material around the mandrel round off radius does not undergo as much plastic deformation as the material further away from the mandrel.
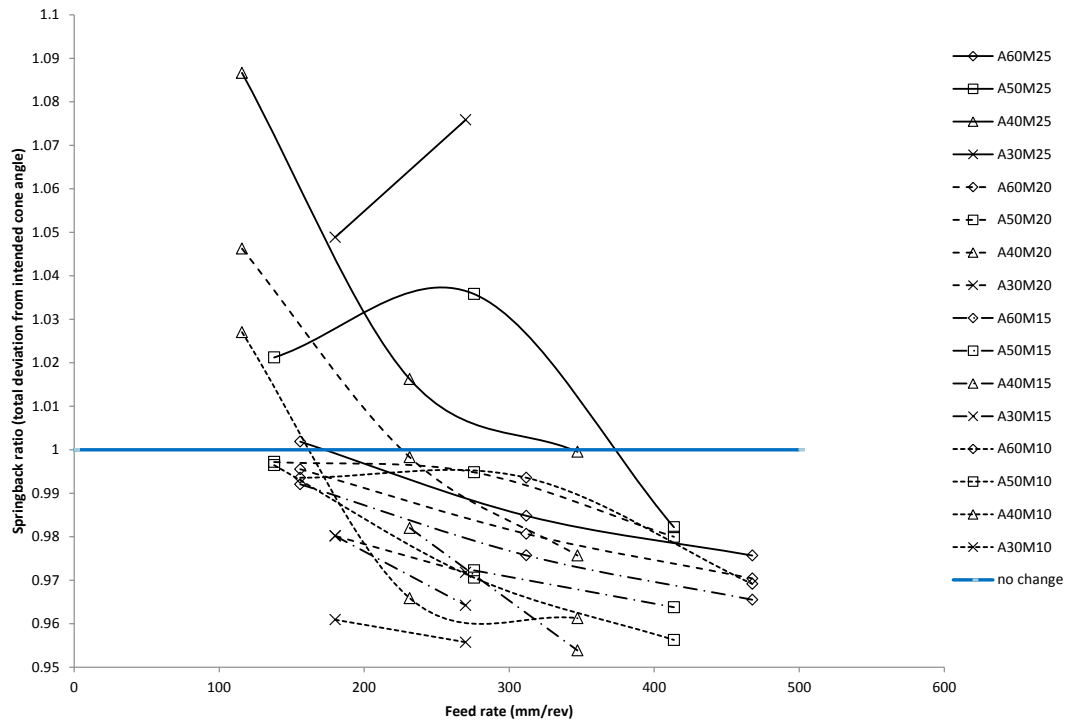


Figure 5.30: Variation of total springback ratio with respect to Feed rate

## 5.5    Variation with contact area

In Chapter 4, the variable M was defined in order to characterise the contact area between the roller and the workpiece; (4.72) is repeated here for convenience:

$$M = \frac{\omega^2 e^{\alpha^{0.6}}}{1200000\alpha} \tag{4.72}$$

where $\omega$ is the mandrel rotational speed (rpm) and $\alpha$ is the half cone angle of the mandrel. Since the contact area between the workpiece and the roller increases as the half cone angle increases and also

as the rotational speed of the mandrel increases, it is important to attach a physical interpretation to M. It can clearly be seen that as ω increases, the value of M also increases. To examine the behaviour of the terms involving $\alpha$, it is useful to compare M with the inequality

$$\frac{e^{\alpha^{0.5}}}{\alpha} \leq \frac{e^{\alpha^{0.6}}}{\alpha} \qquad \text{for } \alpha > 1 \qquad (5.5)$$

Since one application of l'Hôpital's rule demonstrates that the function $\dfrac{e^{\alpha^{0.5}}}{\alpha}$ becomes increasingly large as α increases, it may be stated that $\dfrac{e^{\alpha^{0.6}}}{\alpha}$ also becomes increasingly large as α increases. Hence, since the contact area between the roller and the workpiece increases as the half cone angle of the part increases and as the mandrel rotational speed increases; a larger value of M may be physically interpreted to mean a greater contact area between the roller and the workpiece.

The dependence of the springback ratio on M was examined for each springback simulation performed; the results are shown in Figure 5.31.
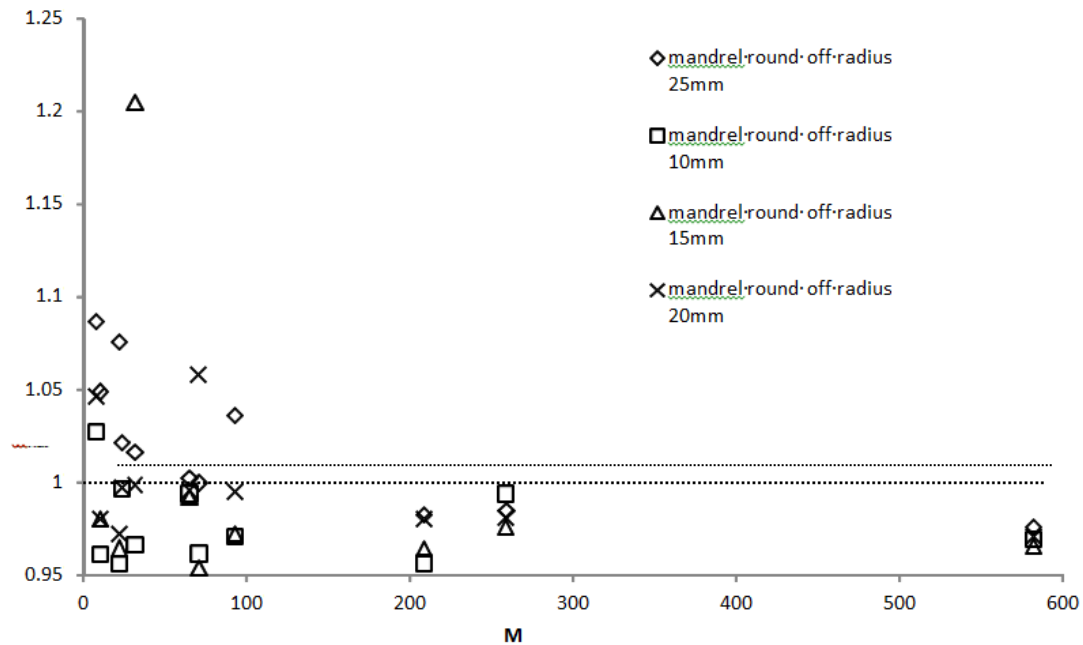
Figure 5.31: Variation of springback ratio (total deviation from half cone angle) with respect to M, defined in (4.72)

Wick *et al*. (1984) state that the feed rate is known to have an impact on the contact area between the roller and the workpiece. Comparison of Figures 5.30 and 5.31 would appear to support this claim, with a larger feed rate resulting in a lower springback ratio.

Figure 5.31 demonstrates that for values of M greater than 100, the springback ratio is less than unity. Furthermore, it may be noted that springback ratios greater than 1 were only observed when M took values less than 100. This may be explained by the fact that to obtain a smaller value of M, either the half cone of the mandrel or the mandrel rotational speed (or both) needs to be reduced. Maintaining the mandrel half cone angle but decreasing the mandrel rotational speed is analogous to decreasing the feed rate. Similarly, maintaining the mandrel rotational speed and decreasing the half cone angle of the mandrel is also analogous to decreasing the feed rate as defined by equation (5.4).

## 5.6      Conclusions of the chapter

 Since it is not possible to eliminate springback, it is important to investigate what can be done to mitigate springback. In this chapter, it was seen that as the feed rate increased, the springback ratio decreased with an optimal feed rate lying around 150-160mm/rev. For all investigated cases where the feed rate was calculated to be 400mm/rev or higher, the springback ratio was less than or equal to 0.98 as demonstrated in Figure 5.30. This implies that for forming processes carried out at higher feed rates; a springback ratio less than unity should be compensated for by attempting to form a slightly larger cone so that the springback acts in a sense that results in the intended cone angle of the part being obtained. For example, at a feed rate of 480mm/rev a mandrel with half cone angle of 60o produces a cone with springback ratio of 0.98, corresponding to a final half cone angle of approximately 54o. The same springback ratio applied to a mandrel of half cone angle 61.2o would produce a cone with half cone angle of 60o.

Investigating the influence of mandrel rotational speed on the springback ratio revealed that as the mandrel rotational speed increased the springback ratio decreased and that with the exception of the 25mm mandrel round off radius, 200rpm was the optimal mandrel rotational speed of the speeds tested, shown in Figure 5.29. Furthermore, Figure 5.29 also demonstrated that in general, the total springback ratio was smaller for smaller mandrel round off radii; this was attributed to the fact that less plastic deformation occurs around the mandrel round off radius when a larger mandrel round off radius is used. Examining Figure 5.29, it is seen that if a part is to be spun at 400rpm or greater, then springback can be somewhat mitigated by using a mandrel with a larger round off radius. Similarly, if a half cone angle and mandrel round off radius have been specified although a free choice of mandrel rotational speed is offered, in order to attain a springback ratio as close to 1 as possible a mandrel rotational speed of 200rpm should  be selected (with the exception of a 40o half cone angle).

In this chapter, the plots for the unloading springback revealed that a clover pattern emerged as the mandrel round-off radius decreased. Although it was shown that the springback does not occur uniformly around the circumference of the part, there was no link found between the thickness strain and these patterns, however these clover patterns were shown to be dependent upon the mandrel round off radius becoming more pronounced as the mandrel round off radius is decreased. This is analogous to stating that for more uniform unloading springback, a mandrel round off radius of 20mm or 25mm should be used.

# §6    Conclusions and suggestions for Future Work

The introduction and literature review detailed the metal spinning process and the research relevant to this project which has been carried out to date. In reviewing the literature, a number of gaps in the literature were identified, namely that investigations into springback in the conventional metal spinning process (Music *et al*. (2010)) and the influence of the mandrel round off radius on process parameters (Xia *et al*. (2005)) were necessary. This thesis has made a contribution to the body of knowledge in addressing these concerns.

In Chapter Four, a three-dimensional finite element model was developed to model a single pass conventional metal spinning process; multiple runs were conducted and a formability surface connecting the mandrel rotational speed, half cone angle and round-off radius was presented. Such a surface has not previously been presented in the literature for the conventional metal spinning of cones using mild steel blanks and a single pass process. The surface illustrated that decreasing the mandrel half cone angle needed to be accompanied by an increase in mandrel rotational speed or an increase in mandrel round-off radius in order for wrinkle free spinning to take place. Furthermore, a formability parameter, *D*, defined as the radial difference between the blank diameter and the mandrel diameter was proposed. This parameter explained the discrepancies experienced by Zhang *et al*. (2012) by applying scaling methods in their research. A further contribution made in Chapter Four was the derivation of a theoretical expression for the hoop force for a single pass conventional metal spinning process; the comparison between the theoretical force and the output from the finite element model highlighted the influence of the contact area between the roller and the blank on the hoop force. An empirical parameter which quantified the contact area in terms of the rotational speed, round-off radius and half cone angle of the mandrel was found. When M was used to scale the theoretical hoop force, the results compared well with the numerical output; this highlights the importance of the contact area between the roller and the workpiece in conventional metal spinning.

The work in this chapter could be extended by performing a similar parametric study to include the formability parameter, $D$, roller velocity and roller clearance and coupling the results with those already obtained. This would enable a more detailed description of the contact area parameter (M).

In chapter 5, a parametric study on three-dimensional springback was carried out; both the in-process and unloading springback was investigated and the in-process springback was found to be the more dominant form. The results showed that springback does not occur uniformly around the part and furthermore, a clover-like cardioid pattern was observed to appear in the plots of the unloading springback as mandrel rotational velocity increases. The deviation from the intended cone angle was found to increase as the feed rate increased, in particular, as the feed rate increased the springback ratio decreased resulting in a half cone angle of the part which was smaller than the intended half cone angle. Examining the plot of total springback against the mandrel rotational velocity, it was evident that with the exception of the $40^o$ cone, reducing the mandrel rotational speed reduced the deviation from the intended half cone angle of the part. Furthermore, it was observed that the springback ratio in the overall deviation from the intended cone angle decreased as the contact area decreased; this implies that the springback may be compensated for by altering the half cone angle of the part depending upon the area coefficient. It also implies that the release of residual stresses is dependent upon the contact area during the forming process. This is in part supported by the work done by Zhan *et al.* (2008) who found that the springback increases as the clearance decreases since the contact area between the roller and the workpiece is likely to decrease as the clearance decreases.

The work in this chapter could be extended by investigating the variation of springback with respect to the formability parameter, $D$ in addition to the roller velocity. Another important line of enquiry would be to investigate the origins of the clover-like pattern which emerges in the plots of the unloading springback. It is the author's speculation that this pattern represents the most efficient way of redistributing the residual stresses and that this may be linked with the contact area between the roller and the workpiece. This may potentially be supported by the investigation into the extrusion process conducted by Yang (1986) referenced in the introduction since it is noticeable that the clover

cross-sectional profile (the cross-sectional profile with the largest contact area between die and workpiece) produced the lowest springback.

It has become apparent that a thorough investigation involving the contact area between the roller and the workpiece needs to be undertaken and a contact parameter to be better defined. Indeed, the contact area has been shown to be interdependent upon the mandrel rotational velocity and half cone angle. It is likely that the contact area is dependent upon more parameters, indeed El-Khabeery (1991) speculated about a thermal gradient in the contact zone which could potentially be responsible for influencing the elasticity of the material depending upon the roller nose radius and the feed rate or the roller. This would indicate that thermal effects should be included in future research.

## Appendix A: Derivation of the volume of a frustum

Consider a cone of perpendicular height Hand base radius R. The cone is cut, parallel to the base at radial distance r as illustrated.
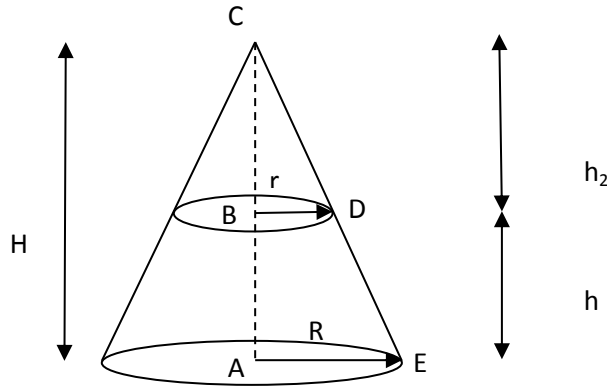


it can be seen that h+h$_2$ = H. The volume of a cone is given by $\dfrac{\pi}{3}R^2H$ and hence, the volume of the frustum may be seen as the difference in volume of two cones and is written as

$$V_{frustum} = \frac{\pi}{3}\left(R^2H - r^2h_2\right) \qquad\qquad \text{AE1}$$

It remains to use similar triangles CBD and CAE in order to replace H and h$_2$ in expression AE1. The aforementioned similar triangles lead to

$$\frac{H}{R} = \frac{h_2}{r} \quad\Rightarrow\quad h_2 = \frac{rH}{R} = \frac{r(h+h_2)}{R} \quad\Rightarrow\quad h_2R = rh + rh_2 \quad\Rightarrow\quad h_2 = \frac{rh}{(R-r)}$$

substituting this result and the fact that H=h+h$_2$ into AE1 leads to

$$V_{frustum} = \frac{\pi}{3}\left(R^2(h+h_2) - r^2h_2\right) = \frac{\pi}{3}\left(R^2h + h_2\left(R^2 - r^2\right)\right) = \frac{\pi}{3}\left(R^2h + \frac{rh}{(R-r)}\left(R^2 - r^2\right)\right) = \frac{\pi h}{3}\left(R^2 + rR + r^2\right)$$

# References

ABAQUS, 2008. *ABAQUS Analysis User's Manual V6.8.* s.l.:s.n.

Advani, S. H., 1967. Stationary waves in a thin spinning disk. *Int. J. Mech. Sci. Pergamon Press Ltd.,* Volume 9, pp. 307-313.

Alberti, N., Cannizzaro, L., Lovalvo, E. & Micari, F., 1989. Analysis of metal spinning processes by the ADINA code. *Computers & Structures,* 32(3-4), pp. 517-525.

Avitzur, B. & Yang, C. T., 1960. Analysis of power spinning of cones. *Journal of Engineering for Industry - Transactions of the ASME (Series B),* Volume 82, pp. 231-245.

Bai, Q., Yang, H. & Zhan, M., 2008. Finite element modeling of power spinning of thin-walled shell with hoop inner rib. *Trans. Nonferrous Met. Soc. China,* Volume 18, pp. 6-13.

Bathe, K. J., 2010. *Finite Element Procedures.* Indian ed. New Delhi: PHI Private Learning Ltd - ISBN-978-81-203-1075-9.

Beni, H. R., Beni, Y. T. & Biglari, F. R., 2010. An experimental-numerical investigation of a metal spinning process. *Proc. IMechE,* Volume 225.

Bewlay, B. P. & Furrer, D. U., 2003. Spinning. *ASM Handbook,* Volume 14B - Metalworking: Sheet Forming (#05120).

Chen, M. D., Hsu, R. Q. & Fuh, K. H., 2001. Forecast of shear spinning force and surface roughness of spun cones by employing regression analysis. *Internationl Journal of Machine Tools & Manufacture,* 41(12), pp. 1721-1734.

Chen, M. D., Hsu, R. Q. & Fuh, K. H., 2005a. Effects of over-roll thickness on cone surface roughness in shear spinning. *Journal of Materials Processing Technology,* 159(1), pp. 1-8.

Chen, M. D., Hsu, R. Q. & Fuh, K. H., 2005b. An analysis of force distribution in shear spinning of cone. *International Journal of Mechanical Sciences,* 47(6), pp. 902-921.

Colding, B. N., 1959. Shear spinning. *ASME Papers,* 2(Paper No 59).

Dierig, H., 1992. CNC spinning using adaptive control. *VDI Fortschrittsberichte, VDI-Verlag, Düsseldorf (in German),* 252(2).

Dixit, P. M. & Dixit, U. S., 2008. Modeling of metal forming and machining processes by finite element and soft computing methods. *Springer-Verlag, ISBN: 978-1-84800-188-6*

Dröge, K. H., 1954. Forces and material flow in spinning. *Technische Universität Dortmund (in German).*

Eggertsen, P. A. & Mattiason, K., 2009. On the modelling of the bending-unbending behaviour for accurate springback predictions. *International Journal of Mechanical Sciences,* Volume 51, pp. 547-563.

El-Khabeery, M. M., Fattouh, M., El-Sheikh, M. N. & Hamed, O. A., 1991. On the conventional simple spinning of cylindrical aluminium cups. *Int. J. Mech. Tools Manufact.,* 31(2), pp. 203-219.

Engauge, 2010. *Engauge Digitizer.* [Online]
Available at: http://digitizer.sourceforge.net
[Accessed 2010].

Essa, K. & Hartley, P., 2009. Numerical simulation of single and dual pass conventional spinning processes. *Int. J. Mater. Form.,* Volume 2, pp. 271-281.

Essa, K. & Hartley, P., 2010. *Optimization of conventional spinning process parameters by means of numerical simulation and statistical analysis.* [Online]
Available at:
http://eprints.bham.ac.uk/628/2/Hartley_2010_Journal_of_Engineering_Manufacture.pdf

Finckenstein, E. v., 1978. Investigations of NC spinning. *Kurzberichte der sitäten der Bundesrepublik Deutschland (in German),* 78(8), pp. 38-39.

Gardiner, F. J., 1957. The springback of metals. *Transactions of the ASME,* Volume 79, pp. 1-9.

Gnaeupol-Herold, T. et al., 2004. A synchrotron study of residual stresses in a Al6022 deep drawn cup. *Materials Science and Engineering,* Volume A366, pp. 104-113.

Gope, P. C., 2012, Machine Design: Fundamentals and Applications, PHI Learning Pvt Ltd, ASIN B008HYPBMI

Hamilton, S. & Long, H., 2008. Analysis of conventional spinning process of a cylindrical part using finite element method. *Steel Research International, Verlag Stahleisen GmbH,* Volume 79, pp. 632-639.

Hayama, M., 1974. On the mechanism of shear spinning. *Proceedings on the international conference on production engineering,* Volume 1, pp. 262-267.

Hayama, M., Kudo, H. & Shinokura, T., 1965a. Experimental study of shear spinning. *Bulletin of JSME,* 8(31), pp. 453-460.

Hayama, M., Kudo, H. & Shinokura, T., 1970. Study of the pass schedule in conventional simple spinning. *Bulletin of the JSME,* 13(65), pp. 1358-1365.

Hayama, M. & Murota, T., 1963. On the study of metal spinning. *Bulletin of the Faculty of Engineering, Yokohama National University,* Volume 12, pp. 53-88.

Hayama, M., Murota, T. & Kudo, H., 1966. Deformation modes and wrinkling of flange on shear spinning. *Bulletin of JSME,* 9(34), pp. 423-433.

Kalpakcioglu, S., 1961a. On the mechanics of shear spinning. *Journal of Engineering for Industry - Transactions of the ASME (Series B),* pp. 125-130.

Kang, D.-C., Gao, X.-C., Meng, X.-F. & Wang, Z.-H., 1999. Study on the deformation mode of conventional spinning of plates. *Journal of Materials Processing Technology,* Volume 91, pp. 226-230.

Kegg, R. L., 1961. A new test method for determination of spinnability of metals. *Journal of Engineering for Industry - Transactions of the ASME (Series B),* Volume 83, pp. 118-125.

Kim, C., Jung, S. Y. & Choi, J. C., 2003. A lower upper-bound solution for shear spinning of cones. *International Journal of Mechanical Sciences,* 45(11), pp. 1893-1911.

Kim, J. H., Park, J. H. & Kim, C., 2006. A study on the mechanics of shear spinning of cones. *Journal of Mechanical Science and Technology,* 20(6), pp. 806-818.

Kirkup, S. M., 2007, The Boundary Element Method in Acoustics, Integrated Sound Software, ISBN 0 953 4031 06

Kleiner, M. et al., 2005. *Optimisation of the shear forming process by means of multivariate statistical methods.* [Online]
Available at: http://www.statistik.tu-dortmund.de/fileadmin/user_upload/Lehrstuehle/MSind/SFB_475/2005/tr23-05.pdf

Kleiner, M. et al., 2002. Combined methods for the prediction of dynamic instabilities in sheet metal spinning. *CIRP Annals-Manufacturing Technology,* 51(1), pp. 209-214.

Koboyashi, S., 1963. Instability in conventional spinning of cones. *Journal of Engineering for Industry - Transactions of the ASME (Series B),* Volume 85, pp. 44-48.

Koboyashi, S., Hall, I. K. & Thomsen, E. G., 1961. A theory of shear spinning of cones. *Journal of Engineering for Industry - Transactions of the ASME (Series B),* Volume 83, pp. 485-495.

Köhne, R., 1984. Rechnergestütze Ermittlung und Verarbeitung von Umformparametern für das Fertigungsverfahren Drücken. *Technische Universität Dortmund.*

Lange, K., 1985. *Handbook of Metal Forming.* New York: McGraw Hill.

Langhaar, H. L., 1951. *Dimensional analysis and theory of models.* s.l.:University of Wisconsin - Madison.

Liu, C. L., 2007. The simulation of the multi-pass and die-less spinning process. *Journal of Materials Processing Technology,* Volume 192-193, pp. 518-524.

Liu, J. H., Yang, H. & Li, Y. Q., 2002. A study of the stress and strain distributions of first-pass conventional spinning under different roller-traces. *Journal of Materials Processing Technology,* Volume 129, pp. 326-329.

Logan, D. L., 2011. *A First Course in the Finite Element Method.* 5th ed. s.l.:Cengage Learning Inc - ISBN: 9780495668275.

Lubliner, J., 2008. *Plasticity Theory.* 25 April ed. New York: Dover Publications Inc - ISBN: 0486462900.

Lu, X. et al., 2006. Three dimensional FE analysis on flange bending for TC4 alloy during shear spinning. *Journal of Materials Science & Technology,* 22(6), pp. 855-859.

Ma, F., Yang, H. & Zhan, M., 2010a. Effects of material properties on power spinning process of parts with transverse inner rib. *Transactions of Nonferrous Metals Society of China,* 20(8), pp. 1476-1481.

Ma, F., Yang, H. & Zhan, M., 2010. Plastic deformation behaviours and their application in power spinning process of conical parts with transverse inner rib. *Journal of Materials Processing Technology,* Volume 210, pp. 180-189.

Marghmaleki, I. S. et al., 2011. Finite element simulation of thermomechanical spinning process. *Procedia Engineering,* Volume 10, pp. 3769-3774.

MatWeb, 2010. *MatWeb.* [Online]
Available at: http://www.matweb.com

Mori, K. & Nonaka, T., 2005. Simplified Three-Dimensional Finite Element Simulation of Shear Spinning Process Based on Axisymmetric Modelling. *Journal of Manufacturing Processes,* 7(1), pp. 51-56.

Music, O. & Allwood, J. M., 2011. Flexible asymmetric spinning. *CIRP Annals - Manufacturing Technology.*

Music, O., Allwood, J. M. & Kawai, K., 2010. A review of the mechanics of metal spinning. *Journal of Materials Processing Technology,* Volume 210, pp. 3-23.

Nagarajan, H. N., Kotrappa, H. & Mallanna, C., 1981. Mechanics of flow forming. *Annals of the CIRP,* 30(1), pp. 159-162.

Oehler, G., 1963. *Biegen.* München: Hanser.

Owen, D. R. J. & Hinton, E., 1986. *Finite Elements in Plasticity. Theory and Practice.* Swansea: Pine-ridge Press Limited.

Ozturk, F., Toros, S., Kilic, S. & Bas, M. H., 2009. *Effect of cold and warm temperatures on springback of aluminium-magnesium alloy 5083-H111.* Nigde University, Nigde, Turkey, Department of Mechanical Engineering.

Packham, C. L., 1976. Metal spinning and shear flow forming. *Metallurgia and Metal Forming,* pp. 168-170, 203-206, 281-285.

Paulton, R. A. & Colding, B. N., 1958. Two new industrial processes for plastic deformation of metals. *Conference Proceedings - Technology of Engineering Manufacturing,* pp. 54-62.

Pippard, A. B., 1978. *The physics of vibration. Vol 1: The simple classical vibrator.* s.l.:Cambridge University Press.

Queener, C. A. & De Angelis, R. J., 1968. Elastic springback and residual stresses in sheet metal formed by bending. *ASM Transactions Quarterly,* Volume 61, pp. 757-768.

Quigley, E. & Monaghan, J., 2000. Metal forming: an analysis of spinning processes. *Journal of Materials Processing Technology,* Volume 103, pp. 114-119.

Quigley, E. & Monaghan, J., 2002a. Enhanced finite element models of metal spinning. *Journal of Materials Processing Technology,* Volume 121, pp. 43-49.

Quigley, E. & Monaghan, J., 2002b. The finite element modelling of conventional spinning using multi-domain models. *Journal of Materials Processing Technology,* Volume 124, pp. 360-365.

Nowinski, J.C., 1982, On the stability of waves in a thin orthotropic spinning disk, *Journal of Applied Mechanics*, 49(3), pp. 570-572.

Ozgur Tekaslan, Ulvi Seker, Ahmet Ozdemir, 2006, Determining springback amount of steel sheet metal has 0.5mm thickness in bending dies, *Materials & Design*, 27(2006), pp. 251-258.

Rahmani, B., Alinejad, G., Bakhshi-Jooybari, M. & Gorji, A., 2009. An investigation on springback/negative springback phenomena using finite element method and experimental approach. *Proc. IMechE Part B: Journal of Engineering Manufacture,* Volume 223, pp. 841-850.

Razavi, H., Biglari, F. R. & Torabkhani, A., 2005. *Study of strains distribution in spinning process using FE simulation and experimental work.* Tehran, Iran, Tehran International Congress on Manufacturing Engineering - December 12-15.

Sebastiani, G. et al., 2006. Numerical investigation on dynamic effects during sheet metal spinning by explicit finite-element-analysis. *Journal of Materials Processing Technology,* Volume 177, pp. 401-403.

Sebastiani, G., Brosius, A., Homberg, W. & Kleiner, M., 2007. Process characterization of sheet metal spinning by means of finite elements. *Key Engineering Materials,* Volume 344, pp. 637-644.

Senior, B. W., 1956. Flange wrinkling in deep-drawing operations. *Journal of the Mechanics and Physics of Solids,* Volume 4, pp. 235-246.

Shimizu, I., 2010. Asymmetric forming of aluminium sheets by synchronous spinning. *Journal of Materials Processing Technology,* Volume 210, pp. 585-592.

Slater, R. A. C., 1979. *A review of analytical and experimental investigations of the spin-forging of sheet metal cones.* London, 1st International Conference on Rotary Metal-Working Processes - November 20-22.

Slater, R. A. C. & Joorabchian, A., 1976. *Spinforging of sheet metal cones having various cone angles and an upper bound estimate for the tangential component force exerted at the workpiece roller interface.* University of Birmingham, Proceedings of the 17th International MTDR Conference, pages 521-529.

Smith, I. M. & Griffiths, D. V., n.d. *Programming the Finite Element Method.* s.l.:Wiley - ISBN: 0-471-96543-x.

Sortais, H. C., Kobayashi, S. & Thomsen, E. G., 1963. Mechanics of conventional spinning. *Journal of Engineering for Industry - Transactions of the ASME,* Volume 85, pp. 346-350.

Valberg, H. S., 2010. *Applied Metal Forming.* 1st ed. s.l.:Cambridge University Press - ISBN: 978-0-521-51823-9.

Wang, L., 2012. *Analysis of Material Deformation and Wrinkling Failure in Conventional Metal Spinning Process.* [Online]
Available at: http://etheses.dur.ac.uk/3537

Wang, L. & Long, H., 2011b. Investigation of material deformation in multi-pass conventional metal spinning. *Materials & Design,* Volume 32, pp. 2891-2899.

Wang, L. & Long, H., 2011c. A study of effects of roller path profiles on tool forces and part wall thickness variation in conventional metal spinning. *Journal of Materials Processing Technology,* Volume 211, pp. 2140-2151.

Wang, L. et al., 2011. Effects of the roller feed ratio on wrinkling failure in conventional spinning of a cylindrical cup. *Proceedings of the IMechE, Part B: Journal of Engineering Manufacture,* Volume 225, pp. 1991-2006.

Wang, L., Long, H., Roberts, M. & White, P., 2010. Analysis of single-pass conventional spinning by taguchi and finite element methods.

Wang, Q., Wang, T. & Wang, Z. R., 1989. A study of the working force in conventional spinning. *The fourth international conference used in rotary forming,* pp. 34-41.

Wells, C. H., 1968. The control of buildup and diametral growth in shear forming. *Transactions of the ASME Series B: Journal of Engineering for Industry,* Volume 2, pp. 63-70.

Wick, C., Benedict, J. T. & Veilleux, R. F., 1984. *Tool and Manufacturing Engineers Handbook.* Volume 2 - Forming, 4th edition ed. s.l.:Mc Graw-Hill, ISBN: 0-87263-135-4.

Withers, P. J. & Bhadeshia, H. K. D. H., 2001. Residual stress part 1 - measurement techniques. *Materials Science and Technology,* Volume 17, pp. 355-365.

Wong, C. C., Dean, T. A. & Lin, J., 2003. A review of spinning, shear forming and flow forming processes. *International Journal of Machine Tools & Manufacture,* 43(14), pp. 1419-1435.

Xia, Q., Shima, S., Kotera, H. & Yasuhuku, D., 2005. A study of the one-path deep drawing spinning of cups. *Journal of Materials Processing Technology,* Volume 159, pp. 397-400.

Yang, D. Y., 1986. Analytical and experimental investigation into lubricated three dimensional extrusion of helical sections. *Annals of the CIRP,* Volume 35/1/1986, pp. 169-171.

Yu, T.X, Johnson, W., Stronge, W.J., 1984, Stamping and springback of circular plates deformed in hemispherical dies. *International Journal of Mechanical Sciences*, Volume 26, Issue 2/1984, pp. 131-148

Zhang, J. et al., 2012. 3D-FE modelling for power spinning of large ellipsoidal heads with variable thickness. *Computational Materials Science,* Volume 53, pp. 303-313.

Zhan, M., Yang, H., Jiang, Z. Q. & Zhang, J. H., 2008. *3D FEM analysis of forming parameters on cone spinning based on orthogonal experimental design method.* s.l., The 9th International Conference on Technology of Plasticity.

Zhan, M. et al., 2007. 3D FEM analysis of influence of roller feed rate on forming force and quality of cone spinning. *Journal of Materials Processing Technology,* Volume 187-188, pp. 486-491.

Zhan, M., Zhanga, J. H., Xua, Y. L. & Maa, F., 2006. Research on variation of stress and strain field and wall thickness during cone spinning. *Materials Science Forum,* Volume 532-533, pp. 149-152.

Zienkiewicz, O. C. & Taylor, R. L., 2005. *The Finite Element Method for Solid and Structural Mechanics.* 6th ed. s.l.:Butterworth-Heinemann - ISBN: 0-7506-6321-9.

Zienkiewicz, O. C. & Taylor, R. L., 2005. *The Finite Element Method, its Basis & Fundamentals.* 6th ed. s.l.:Elsevier - ISBN: 0-7506-6320-0.